

## **General Disclaimer**

### **One or more of the Following Statements may affect this Document**

- This document has been reproduced from the best copy furnished by the organizational source. It is being released in the interest of making available as much information as possible.
- This document may contain data, which exceeds the sheet parameters. It was furnished in this condition by the organizational source and is the best copy available.
- This document may contain tone-on-tone or color graphs, charts and/or pictures, which have been reproduced in black and white.
- This document is paginated as submitted by the original source.
- Portions of this document are not fully legible due to the historical nature of some of the material. However, it is the best reproduction available from the original submission.

~~DR~~  
DRA

R-965

INTERIM TECHNICAL REPORT NO. 3  
ADVANCED EARTH OBSERVATION  
SYSTEM INSTRUMENTATION STUDY

(AEOSIS)

by

R. White, F. Grant,  
H. Malchow, and B. Walker

December 1975

(NASA-CR-152148) ADVANCED EARTH OBSERVATION  
SYSTEM INSTRUMENTATION STUDY (AEOSIS)  
(Draper (Charles Stark) Lab., Inc.) 141 p  
HC A07/MF A01

N77-16105

Unclassified  
G3/17 15430



The Charles Stark Draper Laboratory, Inc.

Cambridge, Massachusetts 02139



**TECHNICAL REPORT STANDARD TITLE PAGE**

1. Report No. R-965	2. Government Accession No.	3. Recipient's Catalog No.	
4. Title and Subtitle <b>INTERIM TECHNICAL REPORT NO. 3 ADVANCED EARTH OBSERVATION SYSTEM INSTRUMENTATION STUDY (AEOSIS)</b>		5. Report Date December 1975	
7. Author(s) <b>R. White, F. Grant, H. Malchow, B. Walker</b>		6. Performing Organization Code	
9. Performing Organization Name and Address <b>The Charles Stark Draper Laboratory, Inc. Cambridge, Mass. 02139</b>		8. Performing Organization Report No. R-965	
10. Work Unit No.		11. Contract or Grant No. <b>NAS5-21917</b>	
12. Sponsoring Agency Name and Address <b>Goddard Space Flight Center National Aeronautics and Space Administration Greenbelt, Maryland 20771 (S. Kant, Code 720.1, Tech. Monitor)</b>		13. Type of Report and Period Covered <b>Project Interim Report for Period August 1, 1974-October 31, 1975</b>	
14. Sponsoring Agency Code			
15. Supplementary Notes			
16. Abstract			
<p>This report presents the results of three studies pertaining to the use of various types of measurements to estimate the orbit and/or attitude of an Earth Observation Satellite. One of the studies was an investigation into the use of known ground targets in the earth sensor imagery, in combination with onboard star sightings and/or range and range rate measurements by ground tracking stations or tracking satellites (TDRSS), to estimate satellite attitude, orbital ephemeris, and gyro bias drift. The objective of the second study was the derivation of generalized measurement equations for star measurements with a particular type of star tracker, and for landmark measurements with a multispectral scanner being proposed for an advanced Earth Observation Satellite. The purpose of the third study was to conduct a preliminary investigation into the use of infra-red horizon measurements to estimate the attitude and gyro bias drift of a geosynchronous satellite.</p>			
17. Key Words Suggested by Author <b>Earth Observation Satellite Attitude and Orbit Estimation Landmark and Star Measurements Ground and TDRSS Tracking</b>		18. Distribution Statement	
19. Security Classif. (of this report) <b>Unclassified</b>	20. Security Classif. (of this page) <b>Unclassified</b>	21. No. of Pages 140	22. Price

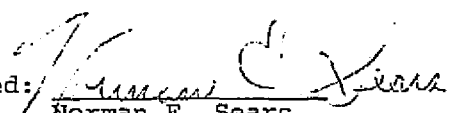
R-965

INTERIM TECHNICAL REPORT NO. 3  
ADVANCED EARTH OBSERVATION  
SYSTEM INSTRUMENTATION STUDY  
(AEOTS)

by

R. White  
F. Grant  
H. Malchow  
B. Walker

December 1975

Approved:   
Norman E. Sears

The Charles Stark Draper Laboratory Inc.  
Cambridge, Massachusetts 02139

#### ACKNOWLEDGEMENT

This report was prepared under Project No. 55-54300, sponsored by the Goddard Space Flight Center of the National Aeronautics and Space Administration through Contract No. NAS5-21917.

Section 2, covering the results of the Modified Landmark Utilization Study, was prepared by Robert L. White and Frederic D. Grant. Section 3 deriving the generalized measurement equations for a star tracker and a multispectral scanner landmark sensor, was written by Harvey Malchow. Section 4, covering the results of the Horizon Utilization Study, was prepared by Robert White and Bruce Walker. Technical assistance in the derivation of the equations for the activities in Sections 2 and 4 was provided by Milton B. Adams and Eliezer Gai. Robert White was the technical director of this program.

The report was typed by Phyllis Amsler.

The publication of this report does not constitute approval by the National Aeronautics and Space Administration of the findings or the conclusions contained herein. It is published only for the exchange and stimulation of ideas.

## TABLE OF CONTENTS

<u>SECTION</u>	<u>Page</u>
1. INTRODUCTION AND SUMMARY .....	1-1
1.1 INTRODUCTION .....	1-1
1.2 PREVIOUS STUDIES .....	1-2
1.3 SUMMARY .....	1-3
2. MODIFIED LANDMARK UTILIZATION STUDY .....	2-1
2.1 INTRODUCTION .....	2-1
2.2 SUMMARY .....	2-5
2.3 COORDINATE SYSTEMS .....	2-6
2.3.1 Basic Inertial Coordinate System .....	2-6
2.3.2 Orbit-Oriented Inertial Coordinate System ...	2-6
2.3.3 Spacecraft Body-Fixed Coordinate System .....	2-8
2.4 SYSTEM EQUATIONS .....	2-9
2.4.1 General Comments .....	2-9
2.4.2 State Dynamics .....	2-10
2.5 MEASUREMENT EQUATIONS .....	2-17
2.5.1 Landmark Measurements .....	2-17
2.5.2 Range and Range Rate Measurements .....	2-18
2.5.3 Star Measurements .....	2-19
2.5.4 Linearization of Measurement Equations .....	2-19
2.6 KALMAN FILTER EQUATIONS .....	2-26
2.7 CONSIDER STATE EQUATIONS .....	2-28
2.7.1 Introduction .....	2-28
2.7.2 Consider State Equations .....	2-28
2.7.3 Consider State Dynamics .....	2-29
2.7.4 Consider State Measurement Equations .....	2-31
2.7.5 Consider State Filter Equations .....	2-31

**TABLE OF CONTENTS (Cont.)**

<u>Section</u>		<u>Page</u>
2.8	ERROR STUDY RESULTS.....	2-33
2.8.1	Introduction.....	2-33
2.8.2	Nominal Values Used in Study.....	2-37
2.8.3	Comparative Results with Different Measurement Configurations.....	2-41
2.8.4	Comparative Results with Ground Tracking and TDRSS Satellites.....	2-44
2.8.5	Filter Performance for Five Landmark Observation Cases.....	2-50
2.8.6	Filter Performance as a Function of Orbit Angle.....	2-50
2.8.7	Performance Sensitivity to System Errors and Parameters.....	2-56
2.9	CONCLUSIONS.....	2-75
3.	STAR AND LANDMARK MEASUREMENT EQUATION DEVELOPMENT.....	3-1
3.1	INTRODUCTION.....	3-1
3.2	STAR TRACKER MEASUREMENT EQUATION.....	3-2
3.2.1	Introduction.....	3-2
3.2.2	Basic Tracker Operation and Measurement.....	3-2
3.2.3	Formal Measurement Equation.....	3-3
3.2.4	Tracker-Inertial Coordinate Relationship....	3-6
3.2.5	Measurement Error Relationships.....	3-7
3.2.6	Evaluation of Sensitivity Partial Derivatives.....	3-10
3.2.7	Sensitivity Example.....	3-14
3.3	LANDMARK MEASUREMENT EQUATION.....	3-18
3.3.1	Introduction.....	3-18
3.3.2	Basic Scanner Operation and Measurement....	3-18
3.3.3	Formal Measurement and Noise.....	3-19
3.3.4	Scanner-Inertial Coordinate Relationship....	3-22
3.2.5	Evaluation of the Sensitivity Partial Derivatives.....	3-25

## TABLE OF CONTENTS (Cont.)

<u>Section</u>		<u>Page</u>
3.4	CONCLUSIONS.....	3-31
4.	HORIZON UTILIZATION STUDY.....	4-1
4.1	INTRODUCTION.....	4-1
4.2	INFRA-RED HORIZON UNCERTAINTY.....	4-2
4.3	STATE AND MEASUREMENT EQUATIONS.....	4-3
	4.3.1 State Equations.....	4-3
	4.3.2 Measurement Equations.....	4-3
	4.3.3 Filter and Smoother Equations.....	4-5
4.4	PERFORMANCE RESULTS.....	4-8
	4.4.1 Introduction.....	4-8
	4.4.2 Performance Results for Geosynchronous Satellite.....	4-8
	4.4.3 Performance Results for Sun Synchronous Satellite.....	4-13
LIST OF REFERENCES.....		R-1

## LIST OF ILLUSTRATIONS

<u>FIGURE</u>		<u>PAGE</u>
2-1	Geometry of Landmark Observation Pass . . . . .	2-2
2-2	Basic Inertial and Orbital-Inertial Coordinate Systems . . . . .	2-7
2-3	Orbital-Inertial and Body-Fixed Coordinate Systems . . . . .	2-7
2-4	Landmark Observation Case 2 . . . . .	2-34
2-5	Landmark Observation Case 4 . . . . .	2-35
2-6	Kalman Filter Position Estimation Performance for Landmark Observation Case 2 . . . . .	2-52
2-7	Kalman Filter Position Estimation Performance for Landmark Observation Case 4 . . . . .	2-53
2-8	Kalman Filter Position Estimation Performance for Landmark Observation Case 2 with Star Sightings . . . . .	2-54
2-9	Kalman Filter Attitude Estimation Performance for Landmark Observation Case 2 . . . . .	2-56
2-10	Kalman Filter Attitude Estimation Performance for Landmark Observation Case 4 . . . . .	2-57
2-11	Kalman Filter Attitude Estimation Performance for Landmark Observation Case 2 with Star Sightings . . . . .	2-59
2-12	Sensitivity to Initial Ephemeris Uncertainty . . .	2-61
2-13	Sensitivity to Initial Gyro Bias Drift Uncertainty . . . . .	2-62
2-14	Sensitivity to Ground Tracking Station Location Uncertainty . . . . .	2-63
2-15	Sensitivity to Range Measurement Noise . . . . .	2-64
2-16	Sensitivity to Range Rate Measurement Noise . . . .	2-66
2-17	Sensitivity to Landmark Position Uncertainty . . .	2-67
2-18	Sensitivity to Number of Range Updates per Pass .	2-68

LIST OF ILLUSTRATIONS (Cont.)

<u>Figure</u>		<u>Page</u>
2-19	Sensitivity to Number of Range Rate Updates per Pass . . . . .	2-70
2-20	Sensitivity to Number of Range & Range Updates per Pass . . . . .	2-71
2-21	Sensitivity to Number of Landmark Updates per Pass .	2-72
3-1	Star Tracker Measurement Geometry . . . . .	3-8
3-2	Landmark Sighting Geometry . . . . .	3-23
4-1	Kalman Filter Performance in Estimating Gyro Bias Drift for Case 2 of Table 4-1 . . . . .	4-12

LIST OF TABLES

<u>Table</u>		<u>Page</u>
2-1	Landmark Observation Cases . . . . .	2-36
2-2	Kalman Filter Performance with Single Types of Measurements . . . . .	2-43
2-3	Kalman Filter Performance with Different Types of Measurements . . . . .	2-45
2-4	Kalman Filter Performance with Ground and TDRSS Tracking Station Measurements . . . . .	2-46
2-5	Kalman Filter Performance with Different TDRSS Ephemeris Uncertainties . . . . .	2-48
2-6	Kalman Filter Performance for Different Landmark Observation Cases . . . . .	2-51
2-7	Sensitivity to Gravitational Harmonic Uncertainties . . . . .	2-74
3-1	Major Error Sources, Types and Representative Values.....	3-5
3-2	MSS Landmark Sighting Errors.....	3-21
4-1	Fraser Smoother Performance for Geosynchronous Satellites.....	4-9
4-2	Fraser Smoother Performance for Sun Synchronous Satellite.....	4-14

## SECTION 1

### INTRODUCTION AND SUMMARY

#### 1.1 INTRODUCTION

This report is the Third Interim Technical Report covering three\* studies performed by The Charles Stark Draper Laboratory, Inc., for the NASA Goddard Space Flight Center during the period from August 1, 1974 to October 31, 1975. These studies were as follows:

- (1) Modified Landmark Utilization Study - An investigation into the use of range and range-rate measurements combined with known landmark sightings using earth sensor imagery to estimate spacecraft attitude, orbital ephemeris, and gyro bias drift. The original Landmark Utilization Study<sup>(1)\*\*</sup> had investigated the combined use of star and known landmark sightings.
- (2) Development of Star and Landmark Measurement Equations - A detailed analysis of star and landmark measurement errors and sensitivities.
- (3) Horizon Utilization Study - An investigation into the use of horizon measurements for estimation of spacecraft attitude and gyro bias drift.

Most of these studies represent a natural follow-on to previous studies performed by CSDL for GSFC pertaining to the optimal treatment of attitude and orbital ephemeris information for spacecraft that generate high-resolution imagery of the Earth. (A brief description of the previous studies is given in the next subsection). One of the long-range goals of this overall effort has been to determine how spacecraft attitude and orbit data can best be used to improve the mapping accuracy of a multi-spectral scanner.

\* A fourth task involving the actual use of army searchlights with Landsats 1 and 2 is still underway and a complete report on this effort will be made in the Final Report.

\*\* Superscripts refer to numbered references at the end of this report.

## 1.2 PREVIOUS STUDIES

Since July 1971, the Draper Laboratory has performed various studies for GSFC pertaining to the determination of attitude and orbital ephemeris for an advanced Earth Observation Satellite (EOS). These are briefly described chronologically in the following paragraphs.

Initial SIMS Trade Study. This study<sup>(2,3,4)</sup> provided GSFC with technical data that could be used for selection of an optimum Stellar-Inertial Measurement System (SIMS) for EOS. From a large number of initial SIMS candidates the following three candidates were selected for detailed evaluation:

SIMS-A	Strapdown gyros and strapdown star mapper	Derived from Honeywell SPARS
SIMS-B	Strapdown gyros and gimbaled star tracker	Derived from TRW PPCS/PADS
SIMS-C	3-Axis gimbaled gyro platform and strapdown star mapper	Subsystems defined by CSDL

A significant accomplishment of this study was the generation of statistical data showing how well the spacecraft attitude and gyro bias drift could be estimated for each candidate. Use was made of an optimal smoother to obtain 'least squares' estimates of attitude and gyro bias drift after processing star measurements over several orbits.

Detailed SIMS-A Study. This study<sup>(5)</sup> was a more detailed and accurate Monte Carlo simulation of SIMS A. This confirmed the statistical estimates of accuracy obtained in the previous study. Performance data was also generated showing the effects of certain bias errors that had not been modeled before in earlier covariance studies. These included errors such as gyro scale factor error and gyro input-axis misalignment.

Attitude Determination with Landmarks. This was an investigation (5) to determine how well spacecraft attitude and gyro bias drift could be estimated using known landmarks in the sensor imagery. The promising results indicated a possible backup method of attitude determination in the event of star sensor failure.

Mapping Error Sensitivity to Errors in Spacecraft Attitude and Orbital Ephemeris. The main objective of this study<sup>(6)</sup> was to determine the effects of errors in spacecraft attitude and in orbital ephemeris on the ability to determine the locations of unknown landmarks relative to known landmarks. Emphasis was placed on landmark location accuracy within the continental USA. One significant result was the discovery that errors in spacecraft attitude and gyro bias drift have a reduced effect on mapping errors due to the presence of certain negative correlations.

Attitude and Ephemeris Determination with Landmarks and Stars. This study<sup>(1)</sup> was an investigation into the use of star sightings together with known landmarks to estimate spacecraft attitude, gyro bias drift and orbital ephemeris. A 12-state covariance analysis was employed for the simulations. One important finding was that known landmarks could be used together with star sightings to satisfactorily estimate orbital ephemeris.

Artificial Landmark Implementation. This study<sup>(1)</sup> was an investigation into the feasibility and practicality of establishing a national system of artificial landmarks suitable for automated recognition.

### I.3 SUMMARY

Section 2 reports the results of the modified landmark utilization studies. A covariance analysis is used to compute satellite state uncertainties with emphasis on systems involving landmark sightings, and tracking facilities. Equations governing the coordinate transformations, the state dynamics, and the estimation process are given. Simulation results are given for parametric variations of measurement noises and update frequencies, and for various combinations of measurement systems.

Section 3 derives generalized measurement equations for star and landmark sightings. The derived equations are specific to certain types of star trackers and landmark sensors, but consider general types of noise sources.

Section 4 presents the results of a study aimed at the use of infrared horizon measurements for satellite attitude and gyro bias drift updates. Measurement equations are derived, the state and estimation equations are given, and simulation results are presented. The results consider variations in measurement noise and update frequency for both sun-synchronous and earth-synchronous orbits.

REPRODUCIBILITY OF THE  
ORIGINAL PAGE IS POOR

## SECTION 2

### MODIFIED LANDMARK UTILIZATION STUDY

#### 2.1 INTRODUCTION

The purpose of the Modified Landmark Utilization Study is to investigate the use of ground or navigation satellite tracking measurements of range and range-rate together with the use of known landmarks observed in the imagery of a multi-spectral scanner (MSS), to estimate spacecraft attitude, orbital ephemeris and gyro bias drift. This system configuration was proposed as an alternative to the one studied in the original Landmark Utilization Study<sup>(1)</sup>. The original study considered the use of star measurements together with known landmark observations. The present study is thus the original study "modified" to incorporate range and range-rate measurements.

This study considers radar measurements of the range and range-rate between an Earth Observation Satellite (EOS) and either a ground tracking station or a navigation satellite of the TDRSS (Tracking and Data Relay Satellite System) type. For the ground tracking configuration, the use of two unified S-Band System radars located at Merritt Island, Florida and at Goldstone, California, are found to be sufficient to give satisfactory tracking of EOS over the continental USA. For the navigation satellite tracking configuration, two geosynchronous TDRSS satellites located over the equator at 41 and 171 degrees west longitude are employed.

The Earth Observation Satellite is assumed to be in a circular sun-synchronous orbit with an inclination of 99 degrees and an altitude of 1000 km (540 nmi). This study also includes the effect of gravitational harmonic uncertainties. Figure 2-1 illustrates a typical observational pass over the continental USA. The ground tracking stations at Merritt Island and Goldstone are indicated. Shown on board the satellite is a multispectral scanner whose beam sweeps back and forth across the ground track to generate a swath of imagery 90 nmi (167 km) wide.

\*Although the swath width for Landsat and the planned EOS is 100 nmi (185 km), the present study is restricted to using landmarks over a smaller swath width since this was the desire of GSFC.

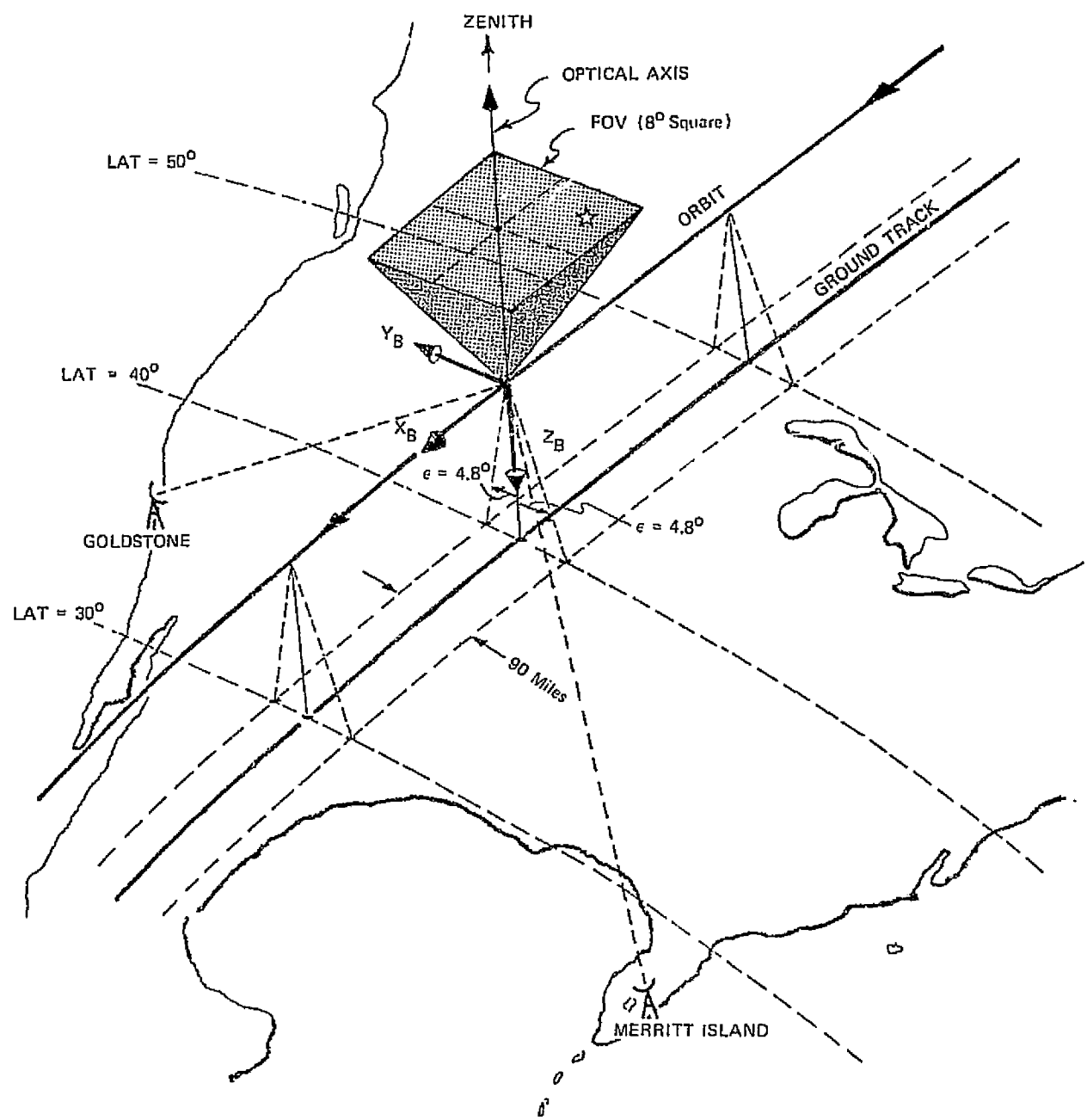


Figure 2-1 Geometry of Landmark Observation Pass

Under nominal attitude conditions (that is, with the  $X_B$ -axis along the local horizontal, and zero roll and yaw angles), the space-craft body axes ( $X_B, Y_B, Z_B$ ) are oriented as shown in Figure 2-1, with  $X_B$  in the direction of spacecraft motion and  $Z_B$  pointing to nadir. It is assumed that the spacecraft has three orthogonal body-mounted gyros aligned with its principal body axes.

In this study optimal filtering techniques are used to process the landmark and the range and range-rate measurements. Since the study is primarily concerned with obtaining a statistical measure of performance in estimating spacecraft attitude, orbital ephemeris, and gyro bias drift, a covariance type of analysis is used. Here, the covariance matrix of the uncertainties in the estimates of the state parameters is propagated and updated using Kalman filter equations. This approach yields a statistical indication of achievable performance for a given system error and measurement noise model.

It should be noted that there are drawbacks to limiting an error analysis to covariance matrix processing alone. One drawback, of course, lies in the simplifying assumptions relative to modeling of spacecraft orbit and attitude history. Another is found in the incomplete modeling of system biases and random processes. To minimize the effects of modeling inadequacies, all important error sources should be modeled. If the statistics for certain states are truly Gaussian, the Kalman filter in linear form can be shown to be optimal. However, if the statistics of some states are poorly known or incorporate non-zero biases, the effort to incorporate poorly modeled states may result in unacceptable performance.

#### Consider States

One example of a state modeling problem in the present study is that associated with the TDRSS satellite ephemeris uncertainties. During the relatively short time of data processing in the present study (typically, 2.5 hours), it would seem reasonable to expect very little change in the TDRSS satellite ephemeris uncertainties. Hence, measurements by TDRSS can be considered

highly time-correlated or as having bias components. Rather than model these uncertainties as white noises, or estimable biases, another approach is to model them as "consider" states. This approach enables the Kalman filter to recognize the presence of the "consider" state variable errors which are unobservable while minimizing the number of estimator or covariance states. The consider state equations are given in Section 2.7. Results are given in Section 2.8.4 comparing estimation uncertainties with TDRSS ephemeris uncertainties modeled as white noises and as consider states.

#### Gravitational Harmonic Uncertainties

The effects of gravitational harmonic uncertainties are included in all covariance runs made for this study. Also taken into account is a 0.2 PPM uncertainty in the main gravitational constant,  $\mu$ . The term-by-term difference between the two most recent Smithsonian gravitational models, SEIII (1973) and SEII (1969), as represented in the C and S expansion coefficients (through  $n,m = 10, 10$ ) is initially defined to be equal to the one sigma uncertainty in knowledge of these coefficients. These differences are subsequently scaled down to match propagation data obtained from GSFC for 5 orbits. The scaling effectively defines the one sigma uncertainties as one-third of the difference between SEII and SEIII coefficients.

To model these uncertainties directly using Monte Carlo techniques would be excessively time-consuming. As an approximate and feasible alternative, ephemeris uncertainty covariance matrices, representing the portion of the orbit that is inaccessible to radar tracking, are generated by Monte Carlo runs with randomized gravitational constant uncertainty. In the covariance runs made for this study this ephemeris uncertainty covariance matrix is incorporated into the simulations at the start of each pass over the USA. Thus the gravitational harmonic uncertainties acting over that portion of the orbit which is beyond radar coverage is approximately accounted for. The effect of these uncertainties on that portion of the pass over the USA having radar coverage is not modeled, since it is relatively negligible.

## 2.2 SUMMARY

This report presents the analytical equations and performance results of the Modified Landmark Utilization Study. The study investigates the use of range and range rate measurements by ground or TDRSS tracking stations, in combination with landmark and/or star measurements, to update a state vector which includes EOS spacecraft attitude, orbital ephemeris and gyro bias drift. Optimal Kalman filter techniques were used to process the different types of measurements. A covariance analysis that gives a statistical indication of performance in estimating spacecraft attitude and orbital ephemeris was adopted for this study. For studies involving TDRSS ephemeris uncertainties, "consider" states were added to the covariance data processing to improve the modeling. The study is restricted to the use of landmarks and ground tracking stations within the continental USA and Alaska. The effect of gravitational harmonic uncertainties is also incorporated into the simulations.

Comparative data is presented showing the performance obtained with various combinations of the indicated measurements. Data is also presented showing the sensitivity of performance to variations in the following parameters:

- (1) Initial uncertainties in spacecraft attitude, orbital ephemeris and gyro bias drift.
- (2) Ground tracking station location uncertainty.
- (3) Range and range-rate measurement noise.
- (4) Number of range and range-rate updates per pass.
- (5) Number of landmark updates per pass.
- (6) Landmark position uncertainty.

The data presented shows that range and range-rate measurements alone can be used to satisfactorily estimate orbital ephemeris, but that landmark measurements must also be incorporated to satisfactorily estimate spacecraft attitude and gyro bias drift.

### 2.3 COORDINATE SYSTEMS

This section defines the reference coordinate systems or frames used in the error study and simulations. These primary reference frames are the following:

Basic Inertial (I-frame)  
Orbit-Oriented Inertial (O-frame)  
Body-Fixed (B-frame)

#### 2.3.1 Basic Inertial Coordinate System (I-Frame)

The coordinate axes for this system are defined in Figure 2-2. The axes  $X_I$  and  $Y_I$  both lie in the equatorial plane with  $X_I$  pointing towards the vernal equinox. Axis  $Z_I$  points along the north polar axis of the Earth. Star catalogs normally give the directions of stars in this coordinate system.

#### 2.3.2 Orbit-Oriented Inertial Coordinate System (O-Frame)

This system of axes is also defined in Figure 2-2. The coordinate system is oriented relative to the basic inertial coordinate system through the angles  $\Omega$  and  $i$ . The first angle is the right ascension of the orbit ascending node, and the angle  $i$  is the orbit inclination. This orbital plane does precess slowly about the earth's rotational pole due to oblateness of the earth. However, the orbit-oriented coordinate system is defined herein to be an inertial frame since, in our simulations, orbit plane rotation due to precession is ignored as it would add unnecessary complexity to the simulations. Since real rotation of the EOS orbit plane is a small fraction of a degree over the course of a typical simulation, the distribution of available stars is not affected by such precession. The transformation matrix  $T_{OI}$ , from

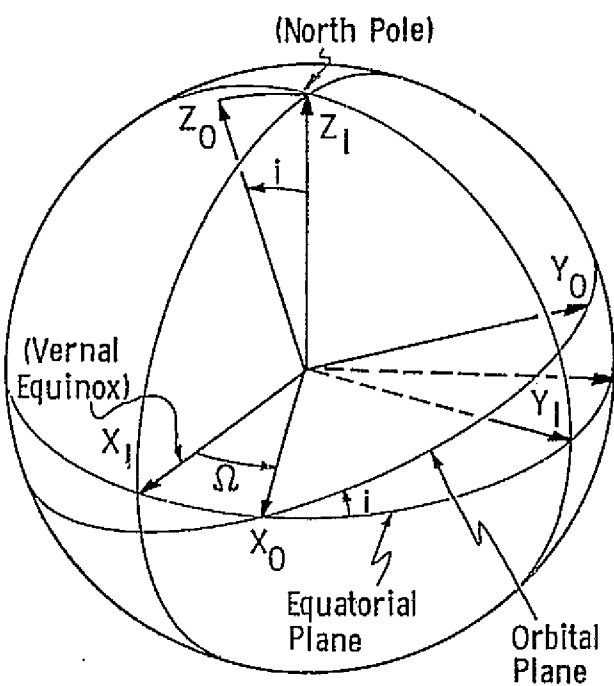


Figure 2-2 Basic Inertial and Orbital-Inertial Coordinate Systems

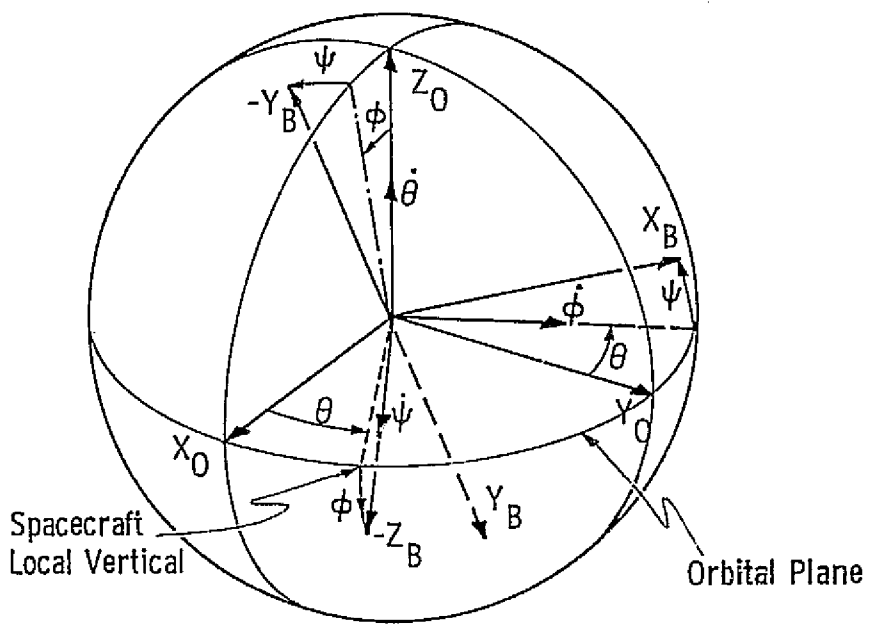


Figure 2-3 Orbital-Inertial and Body-Fixed Coordinate Systems

basic inertial to orbit-oriented inertial coordinates is given by:

$$T_{OI} = \begin{bmatrix} 1 & 0 & 0 \\ 0 & ci & si \\ 0 & -si & ci \end{bmatrix} \begin{bmatrix} c\Omega & s\Omega & 0 \\ -s\Omega & c\Omega & 0 \\ 0 & 0 & 1 \end{bmatrix} \quad (2-1)$$

where  $c$  denotes cosine, and  $s$  denotes sine. Thus a star vector  $\underline{s}_O$  in the orbit-oriented frame can be computed, given the star vector  $\underline{s}_I$  in basic inertial coordinates.

$$\underline{s}_O = T_{OI} \underline{s}_I \quad (2-2)$$

### 2.3.3 Spacecraft Body-Fixed Coordinate System (B-Frame)

The axes of this system are such that  $X_B$ ,  $Y_B$ , and  $Z_B$  are respectively the roll, pitch and yaw axes of the spacecraft. The nominal orientation of these axes is as follows:

$X_B$  - is along the projection of the spacecraft velocity vector onto the local horizontal plane

$Y_B$  - is normal to the orbital plane

$Z_B$  - is along the local nadir

The orientation of the B-frame with respect to the O-frame is shown in Figure 2-3. The transformation from the O-frame to the B-frame is through the Euler angle sequence of pitch ( $\theta$ ), roll ( $\phi$ ), and yaw ( $\psi$ ) as shown in Figure 2-3 and expressed by:

$$T_{BO} = \begin{bmatrix} 0 & 1 & 0 \\ 0 & 0 & -1 \\ -1 & 0 & 0 \end{bmatrix} \begin{bmatrix} 1 & 0 & 0 \\ 0 & c\psi & s\psi \\ 0 & -s\psi & c\psi \end{bmatrix} \begin{bmatrix} c\phi & 0 & -s\phi \\ 0 & 1 & 0 \\ s\phi & 0 & c\phi \end{bmatrix} \begin{bmatrix} c\theta & s\theta & 0 \\ -s\theta & c\theta & 0 \\ 0 & 0 & 1 \end{bmatrix} \quad (2-3)$$

The input axes for the strapdown gyros are ideally colinear with the spacecraft body-fixed axes, so that  $x_g = x_B$ ,  $y_g = y_B$  and  $z_g = z_B$ .

## 2.4 SYSTEM EQUATIONS

### 2.4.1 General Comments

In the present study the state to be estimated consists of twelve parameters which comprise 3 attitude angles, 3 orbital position components, 3 orbital velocity components, and the bias drift of each of 3 gyros. These parameters can be represented as the components of a twelve dimensional state vector  $\underline{x}$ . The dynamic behavior of the system with the above state can be described by the following nonlinear differential state equation:

$$\dot{\underline{x}} = \underline{f} (\underline{x}, \underline{u}, t) \quad (2-4)$$

where  $t$  is time and  $\underline{u}$  is the noise introduced by gyro random drift, gyro quantization, etc. . A priori information about the statistics of the noise  $\underline{u}$  is given by the covariance matrix  $Q$  where:

$$E [\underline{u}(t) \underline{u}^T(\tau)] = Q \cdot \delta(t-\tau) \quad (2-5)$$

At some arbitrary time,  $t_n$ , a measurement  $\underline{z}(t_n)$  is taken. This measurement is related to the state through the measurement equation:

$$\underline{z}(t_n) = \underline{h} (\underline{x}(t_n), \underline{v}(t_n), t_n) \quad (2-6)$$

where  $\underline{v}(t_n)$  is the measurement noise of a zero mean white gaussian process whose covariance matrix  $R$  is given by:

$$E [\underline{v}(t_n) \underline{v}^T(t_{n-1})] = R \cdot \delta(t_n - t_{n-1}) \quad (2-7)$$

For the special case where Equations 2-4 and 2-6 are linear, the standard Kalman Filter would be used to obtain optimal estimates of the

state. However, in the present case, these equations are nonlinear and must be linearized before using the so-called "Extended Kalman Filter". This linearization is generally performed around the estimated values of the state. In the present covariance analysis, however, there is no estimated state and use is made of the known nominal state for this purpose.

For the Extended Kalman Filter, the new state and measurement vectors are defined as:

$$\delta \underline{x} = \underline{x} - \underline{x}_{\text{nom}} \quad (2-8)$$

$$\delta \underline{z} = \underline{z} - \underline{z}_{\text{nom}}$$

The corresponding state and measurement equations are:

$$\dot{\delta \underline{x}} = F \delta \underline{x} + G \delta \underline{u} \quad (2-9)$$

$$\delta \underline{z} = H \delta \underline{x} + A \delta \underline{v} \quad (2-10)$$

where the matrices  $F$ ,  $G$ ,  $H$ , and  $A$  are:

$$F = \frac{\partial f}{\partial \underline{x}} \left| \begin{array}{c} \\ \underline{x}_{\text{nom}} \\ \underline{u} = 0 \end{array} \right. \quad G = \frac{\partial f}{\partial \underline{u}} \left| \begin{array}{c} \\ \underline{x}_{\text{nom}} \\ \underline{u} = 0 \end{array} \right. \quad (2-11)$$

$$H = \frac{\partial h}{\partial \underline{x}} \left| \begin{array}{c} \\ \underline{x}_{\text{nom}} \\ \underline{v} = 0 \end{array} \right. \quad A = \frac{\partial h}{\partial \underline{v}} \left| \begin{array}{c} \\ \underline{x}_{\text{nom}} \\ \underline{v} = 0 \end{array} \right.$$

#### 2.4.2 State Dynamics

The original nonlinear state of the system  $\underline{x}$  is defined as the following twelve dimensional vector:

$$\underline{x}^T = (\theta, \phi, \psi, B_x, B_y, B_z, x, y, z, v_x, v_y, v_z) \quad (2-12)$$

where

$\theta, \phi, \psi$  - Euler angles defining the body attitude with respect to the orbital frame.

$B_x, B_y, B_z$  - Bias drift of roll (X), pitch (Y), and yaw (Z) gyros

$x, y, z$  - Components of the spacecraft position vector in the Basic Inertial frame

$v_x, v_y, v_z$  - Components of the spacecraft velocity vector in the Basic Inertial frame

The equations that relate the Euler rates ( $\dot{\theta}, \dot{\psi}, \dot{\phi}$ ) to the spacecraft body rates ( $\omega_x, \omega_y, \omega_z$ ), measured by the X, Y, and Z gyros, are given by:

$$\begin{bmatrix} \dot{\theta} \\ \dot{\phi} \\ \dot{\psi} \end{bmatrix} = \begin{bmatrix} s\psi/c\phi & -c\psi/c\phi & 0 \\ c\psi & s\psi & 0 \\ s\phi s\psi/c\phi & -s\phi c\psi/c\phi & -1 \end{bmatrix} \begin{bmatrix} \omega_x \\ \omega_y \\ \omega_z \end{bmatrix} \quad (2-13)$$

or in matrix notation:

$$\dot{\underline{\xi}} = G(\underline{\xi}) \underline{\omega} \quad (2-14)$$

where  $\underline{\xi}^T = [\theta, \phi, \psi]$

$$\underline{\omega}^T = [\omega_x, \omega_y, \omega_z]$$

$G(\underline{\xi})$  = the matrix in Equation 2-13.

The relationship between the gyro measured body rates ( $\underline{\omega}$ ) and the true body rates ( $\underline{\omega}_t$ ) sensed by the gyros is:

$$\underline{\omega} = \underline{\omega}_t + \underline{D} \quad (2-15)$$

$$\text{where } \underline{\omega}_t^T = (0, -\omega_o, 0) \quad (\omega_o = \text{orbital rate}) \quad (2-16)$$

and  $\underline{D}$  represents the gyro drift rate which can be expressed as follows:

$$\underline{D} = \underline{B} + \underline{\eta} \quad (2-17)$$

where  $\underline{B}$  = gyro bias drift

$\underline{\eta}$  = additive white noise (gyro random drift).

The gyro random drift is assumed to be a zero mean white gaussian noise whose covariance matrix Q is given by:

$$E [\underline{\eta}(t) \underline{\eta}^T(\tau)] = Q \cdot \delta(t-\tau) \quad (2-18)$$

Equations 2-14 can therefore be rewritten as:

$$\dot{\underline{\xi}} = G(\underline{\xi}) \underline{\omega}_t + G(\underline{\xi}) \underline{B} + G(\underline{\xi}) \underline{\eta} \quad (2-19)$$

Since the components of the  $\underline{B}$  vector are unknown constants\*, they should be included as additional elements to be estimated in the state vector. This can be done by augmenting Equation 2-19 and including  $\underline{B}$  in the state. Recalling that for constants there are no dynamics:

$$\dot{\underline{B}}^T = (0, 0, 0) \quad (2-20)$$

Hence, Equation 2-19 can be changed to:

$$\begin{bmatrix} \dot{\underline{\xi}} \\ \dot{\underline{B}} \end{bmatrix} = \begin{bmatrix} 0_3 & G(\underline{\xi}) \\ 0_3 & 0_3 \end{bmatrix} \begin{bmatrix} \underline{\xi} \\ \underline{B} \end{bmatrix} + \begin{bmatrix} G(\underline{\xi}) \\ 0_3 \end{bmatrix} (\underline{\omega}_t + \underline{\eta}) \quad (2-21)$$

where  $0_3$  is a  $3 \times 3$  null matrix.

Since the orbital dynamics are uncoupled with the attitude angle dynamics, their description is given by a separate set of first-order ordinary differential equations:

\*For the purposes of this study, the gyro bias drift is assumed to be unknown. However, in normal practice, a portion of the gyro bias drift is usually known and is compensated for when integrating the outputs of the gyros.

$$\begin{bmatrix} \cdot \\ \underline{\dot{r}} \\ \cdot \\ \underline{\dot{v}} \end{bmatrix} = \begin{bmatrix} \underline{v} \\ \frac{-\mu}{|\underline{r}|^3} \underline{r} \end{bmatrix} \quad (2-22)$$

where

$$\underline{v}^T = (v_x, v_y, v_z)$$

$$\underline{r}^T = (x, y, z)$$

$\mu$  = gravitational constant

The combined state of the system for attitude, orbital ephemeris, and gyro bias drift can be written as:

$$\underline{x}^T = (\underline{\xi}^T, \underline{B}^T, \underline{r}^T, \underline{v}^T) \quad (2-23)$$

where the dynamics of this state are given by Equations 2-21 and 2-22. However, both equations are nonlinear and must be linearized around the nominal state values. Let a new 12 dimensional state be defined as follows:

$$\delta\underline{x}^T = (\delta\underline{\xi}^T, \delta\underline{B}^T, \delta\underline{r}^T, \delta\underline{v}^T) \quad (2-24)$$

where

$$\begin{aligned} \delta\underline{\xi} &= \underline{\xi} - \underline{\xi}_0, \quad \delta\underline{r} = \underline{r} - \underline{r}_0 \\ \delta\underline{B} &= \underline{B} - \underline{B}_0, \quad \delta\underline{v} = \underline{v} - \underline{v}_0 \end{aligned} \quad (2-25)$$

In Equations 2-25 the vectors  $\underline{r}_0$  and  $\underline{v}_0$  are the position and velocity for a nominal circular orbit with an orbital rate  $\omega_0$ , and

$$\underline{\xi}_0^T = (\omega_0 t, 0, 0), \quad \underline{B}_0^T = (0, 0, 0)$$

To linearize Equation 2-21 define:

$$F_1 = \frac{\partial}{\partial \underline{\xi}} \begin{bmatrix} G(\underline{\xi}) & \omega_t \end{bmatrix} \Bigg|_{\underline{\xi} = \underline{\xi}_0} = \begin{bmatrix} 0 & 0 & 0 \\ 0 & 0 & -\omega_0 \\ 0 & \omega_0 & 0 \end{bmatrix} \quad (2-26)$$

$$G_1 = G(\underline{\xi}) \Bigg|_{\underline{\xi} = \underline{\xi}_0} = \begin{bmatrix} 0 & -1 & 0 \\ 1 & 0 & 0 \\ 0 & 0 & -1 \end{bmatrix} \quad (2-27)$$

so that the linearized expression for Equation 2-21 can be written as:

$$\begin{bmatrix} \dot{\delta \underline{\xi}} \\ \vdots \\ \delta \underline{B} \end{bmatrix} = \begin{bmatrix} F_1 & G_1 \\ O_3 & O_3 \end{bmatrix} \begin{bmatrix} \delta \underline{\xi} \\ \delta \underline{B} \end{bmatrix} + \begin{bmatrix} G_1 \\ O_3 \end{bmatrix} \delta \underline{n} \quad (2-28)$$

To linearize Equation 2-22 define:

$$\begin{aligned} F_2 &= \frac{\partial}{\partial \underline{r}} \begin{bmatrix} -\mu & \underline{r} \\ |\underline{r}|^3 & \end{bmatrix} \Bigg|_{\underline{r} = \underline{r}_0} \\ &= -\frac{\mu}{r^5} \begin{bmatrix} (r^2 - 3x^2) & -3xy & -3xz \\ -3xy & (r^2 - 3y^2) & -3yz \\ -3xz & -3yz & (r^2 - 3z^2) \end{bmatrix} \end{aligned} \quad (2-29)$$

where  $x$ ,  $y$ , and  $z$  are the components of  $\underline{r}_0$  and  $r$  is the magnitude of  $\underline{r}_0$ . The linearized expression for Equation 2-22 can now be written as:

$$\begin{bmatrix} \dot{\delta \underline{r}} \\ \dot{\delta \underline{v}} \end{bmatrix} = \begin{bmatrix} O_3 & I_3 \\ F_2 & O_3 \end{bmatrix} \begin{bmatrix} \delta \underline{r} \\ \delta \underline{v} \end{bmatrix} \quad (2-30)$$

where  $I_3$  is a  $3 \times 3$  identity matrix.

Having determined the linearized state equations for both attitude and orbital ephemeris (Equations 2-28 and 2-30), these equations may be combined to represent the state equation of the full linearized state as follows:

$$\dot{\delta \underline{x}} = F \delta \underline{x} + G \delta \underline{\eta} \quad (2-31)$$

where  $\delta \underline{x}$  is given in Equation 2-24 and

$$F = \begin{bmatrix} F_1 & G_1 & 0_3 & 0_3 \\ 0_3 & 0_3 & 0_3 & 0_3 \\ 0_3 & 0_3 & 0_3 & I_3 \\ 0_3 & 0_3 & F_2 & 0_3 \end{bmatrix}, \quad G = \begin{bmatrix} G_1 \\ 0_3 \\ 0_3 \\ 0_3 \end{bmatrix} \quad (2-32)$$

Since  $F_1$  and  $G_1$  are time invariant, because of linearization around the nominal state instead of the estimated state, a transition matrix can be derived for the attitude state Equation 2-28 using Laplace transform techniques:

$$\Phi_{att}^{(k,k-1)} = \left[ \begin{array}{ccc|cc|c} 1 & 0 & 0 & 0 & -\Delta t_k & 0 \\ 0 & C & -S & S/\omega_o & 0 & (1-C)/\omega_o \\ 0 & S & C & (1-C)/\omega_o & 0 & -S/\omega_o \\ \hline & & & \vdots & & \\ & 0_3 & & \vdots & & I_3 \end{array} \right] \quad (2-33)$$

where  $k$  and  $k-1$  denote the times ( $t_k$  and  $t_{k-1}$ ) of the present and previous measurements:  $\omega_o$  is the orbital rate;  $\Delta t_k = t_k - t_{k-1}$ ;  $S = \sin(\lambda)$ ,  $C = \cos(\lambda)$ ; and  $\lambda = \omega_o \Delta t_k$ .

The derivation of the transition matrix for the orbital ephemeris state equation (Equation 2-30) is more complicated since  $F_2$  is time varying. However, an approximate solution<sup>(9)</sup> in local vertical coordinates is:

$$\Phi_{LV}^{(k, k-1)} = \begin{bmatrix} (2-C) & S & 0 & S/\omega_0 & 2(1-C)/\omega_0 & 0 \\ (2S-3\lambda) & (2C-1) & 0 & 2(C-1)/\omega_0 & (4S-3\lambda)/\omega_0 & 0 \\ 0 & 0 & C & 0 & 0 & S/\omega_0 \\ \omega_0(3\lambda-S) & \omega_0(1-C) & 0 & (2-C) & (3\lambda-2S) & 0 \\ \omega_0(C-1) & -\omega_0S & 0 & -S & (2C-1) & 0 \\ 0 & 0 & -\omega_0S & 0 & 0 & C \end{bmatrix} \quad (2-34)$$

The transition matrix in Equation 2-34 can be expressed in basic inertial coordinates as follows:

$$\Phi_{eph}^{(k, k-1)} = T \Phi_{LV}^{(k, k-1)} T^T \quad (2-34a)$$

where:

$$T = \begin{bmatrix} T_{ILV} & O_3 \\ O_3 & T_{ILV} \end{bmatrix}$$

$$T_{ILV} = \begin{bmatrix} T_{OI}^T & T_{OLV} \end{bmatrix}$$

$$T_{OLV} = \begin{bmatrix} C & -S & 0 \\ S & C & 0 \\ 0 & 0 & 1 \end{bmatrix}$$

The transition matrix for the combined state for perturbations on attitude, gyro bias drift, and orbital ephemeris is therefore:

$$\Phi(k, k-1) = \begin{bmatrix} \Phi_{att}^{(k, k-1)} & O_6 \\ O_6 & \Phi_{eph}^{(k, k-1)} \end{bmatrix} \quad (2-35)$$

where  $O_6$  is the  $6 \times 6$  null matrix.

## 2.5 MEASUREMENT EQUATIONS

For this study the measurement data is primarily collected from two instruments, the multi-spectral scanner and the tracking radar. The first measures the line-of-sight (LOS) to known landmarks while the second measures range and range rate from either ground stations or navigation satellites. Also included in the study for comparison purposes is measurement data from the star tracker ( $8^{\circ}$  FOV) of the LOS to known stars. The measurements are usually assumed to be corrupted by white noise.

### 2.5.1 Landmark Measurements

Landmark measurements are obtained by using a multi-spectral scanner (MSS) whose beam sweeps back and forth across the ground track to generate a 90 mile wide swath of ground imagery (see Figure 2-1). Under the nominal attitude conditions considered in this study, the maximum angular excursion of the beam from local vertical is  $4.8^{\circ}$ . The direction of the beam in body coordinates is defined by the angles  $\alpha_M$  and  $\beta_M$ . Here  $\alpha_M$  is the sweep angle, measured positively about the  $x$  body axis, between the  $z$  body axis and the beam; and  $\beta_M$  is nominally zero and is primarily introduced to account for errors in the remaining dimension of angular measurement.

Since the beam is always near the local vertical, the downrange and crosstrack errors in landmark position were modeled as equivalent angular errors in  $\alpha_M$  and  $\beta_M$ . It should be noted that a full scheme including state estimation would require a more exact error model. The above simplified model was considered to be adequate for this covariance analysis. No consideration was given to landmark altitude error since the system sensitivity to this error is relatively small.

The unit vector defining the measured LOS to the landmark in body coordinates is:

$$\underline{\underline{m}}_B = \begin{bmatrix} 1 & 0 & 0 \\ 0 & c\alpha_M & -s\alpha_M \\ 0 & s\alpha_M & c\alpha_M \end{bmatrix} \begin{bmatrix} c\beta_M & 0 & s\beta_M \\ 0 & 1 & 0 \\ -s\beta_M & 0 & c\beta_M \end{bmatrix} \begin{bmatrix} 0 \\ 0 \\ 1 \end{bmatrix} = \begin{bmatrix} s\beta_M \\ -s\alpha_M c\beta_M \\ c\alpha_M c\beta_M \end{bmatrix} \quad (2-36)$$

The estimated LOS to the landmark in body coordinates is the following unit vector:

$$\hat{\underline{m}}_B = T_{BO} T_{OI} \text{ Unit } (\underline{l} - \underline{r}) \quad (2-37)$$

where  $\underline{r}$  is the estimated spacecraft position vector and  $\underline{l}$  is the landmark position vector, both in basic inertial coordinates at the time of measurement.

### 2.5.2 Range and Range-Rate Measurements

The range and range-rate measurements represent the range and the range rate between EOS and either a ground tracking station (USBS radar) or a navigational satellite.

The range from a tracking station to the spacecraft is simply:

$$R_s = |\underline{r} - \underline{r}_T| \quad (2-38)$$

and the range rate is:

$$\dot{R}_s = \frac{(\underline{v} - \underline{v}_T) \cdot (\underline{r} - \underline{r}_T)}{|\underline{r} - \underline{r}_T|} \quad (2-39)$$

where  $\underline{r}$ ,  $\underline{v}$  are the spacecraft position and velocity vectors, and  $\underline{r}_T$ ,  $\underline{v}_T$  are the tracking station position and velocity vectors in basic inertial coordinates at the time of measurement.

For this study the tracking station may be either (1) a ground tracking station, or (2) a geosynchronous navigational satellite. For either type of tracking station, the station velocity is given by:

$$\underline{v}_T = \omega_T \times \underline{r}_T \quad (2-40)$$

where  $\omega_T$  is the inertial earth angular rate of the tracking station with respect to the center of the Earth.

### 2.5.3 Star Measurements

Only one type of star tracker is considered in this study, and it is used only to supplement other types of measurements. This is the 8° FOV star tracker somewhat similar to the CT401 tracker of Ball Brothers Research Corporation. This is a strapdown tracker with no gimbals. The measured direction of a star passing through the FOV is electronically indicated by two angles  $\alpha_T$  and  $\beta_T$ . These are used in the following equation to obtain a unit vector defining the measured LOS to the star in body coordinates.

$$\hat{s}_B = \begin{bmatrix} c\beta_T & 0 & -s\beta_T \\ 0 & 1 & 0 \\ s\beta_T & 0 & c\beta_T \end{bmatrix} \begin{bmatrix} 1 & 0 & 0 \\ 0 & c\alpha_T & s\alpha_T \\ 0 & -s\alpha_T & c\alpha_T \end{bmatrix} \begin{bmatrix} 0 \\ 0 \\ -1 \end{bmatrix} = \begin{bmatrix} s\beta_T c\alpha_T \\ -s\alpha_T \\ -c\beta_T c\alpha_T \end{bmatrix} \quad (2-41)$$

The estimated LOS to the star in body coordinates is given by the following unit vector:

$$\hat{s}_B = T_{BO} T_{OI} \hat{s}_I \quad (2-42)$$

where  $\hat{s}_I$  is the unit LOS vector to the star in basic inertial coordinates and  $T_{BO}$  is a function of the estimated body attitude angles  $\theta$ ,  $\phi$  and  $\psi$ . (See Equation 2-3). A more detailed model of this tracker is discussed in Section 3.

### 2.5.4 Linearization of Measurement Equations

The extended Kalman Filter requires that the measurement equations be in a linear form, here given as:

$$\delta z_i = H_i \delta \underline{x} + H_{ci} \delta \underline{x}_c + A_i \delta v_i \quad (2-43)$$

where  $H_i$  is the sensitivity of the measurement to the state,  $H_{ci}$  is the sensitivity to the consider states,  $x_c$ , and  $A_i$  is the sensitivity of the measurement to the noise. (Consider states are discussed in Section 2.6). The subscript  $i$  is replaced by  $M$  for the MSS landmark sightings, by  $R$  and  $\dot{R}$  for the range and range rate measurements and by  $T$  for the star tracker measurements.

### Landmark Measurement

Linearization of the estimated landmark measurement equation yields the following<sup>\*</sup>:

$$H_M = \frac{\partial \hat{m}_B}{\partial \underline{x}} \Bigg|_{\underline{x}=\underline{x}_O} = \frac{\partial}{\partial \underline{x}} \left[ T_{BO} T_{OI} \text{ Unit } (\underline{l}-\underline{x}) \right] \Bigg|_{\underline{x}=\underline{x}_O} \quad (2-44)$$

$$= \frac{\partial}{\partial \underline{x}} \left[ T_{BO} \right]_{\underline{x}=\underline{x}_O} T_{OI} \text{ Unit } (\underline{l}-\underline{x}) + T_{BO} T_{OI} \frac{\partial}{\partial \underline{x}} \left[ \text{Unit } (\underline{l}-\underline{x}) \right]_{\underline{x}=\underline{x}_O} \quad (2-45)$$

$$= \begin{bmatrix} H_\theta & H_\phi & H_\psi & 0 & 0 & 0 & H_x & H_y & H_z & 0 & 0 & 0 \\ 0 & 0 & 0 & 0 & 0 & 0 & 0 & 0 & 0 & 0 & 0 & 0 \end{bmatrix} \quad (2-46)$$

where the following are the submatrices (or vectors) due to differentiation with respect to the state elements:

$$H_\theta = \begin{bmatrix} -c\theta & -s\theta & 0 \\ 0 & 0 & 0 \end{bmatrix} T_{OI} \text{ Unit } (\underline{l}-\underline{x}) \quad (2-47)$$

$$H_\phi = \begin{bmatrix} 0 & 0 & 0 \\ -c\theta & -s\theta & 0 \end{bmatrix} T_{OI} \text{ Unit } (\underline{l}-\underline{x}) \quad (2-48)$$

$$H_\psi = \begin{bmatrix} 0 & 0 & 1 \\ -s\theta & c\theta & 0 \end{bmatrix} T_{OI} \text{ Unit } (\underline{l}-\underline{x}) \quad (2-49)$$

$$H_x = T_{BO_2} T_{OI} \frac{1}{d^3} \begin{bmatrix} (l_x - x)^2 - d^2 \\ (l_y - y)(l_x - x) \\ (l_z - z)(l_x - x) \end{bmatrix} \quad (2-50)$$

$$H_y = T_{BO_2} T_{OI} \frac{1}{d^3} \begin{bmatrix} (l_x - x)(l_y - y) \\ (l_y - y)^2 - d^2 \\ (l_z - z)(l_y - y) \end{bmatrix} \quad (2-51)$$

\*Note that only two rows are given for the matrix  $H_M$  since only two of the three components of a "unit" LOS vector are needed to completely define the line-of-sight to a landmark, star, etc..

$$H_z = T_{BO_2} T_{OI} \frac{1}{d^3} \begin{bmatrix} (l_x - x)(l_z - z) \\ (l_y - y)(l_z - z) \\ (l_z - z)^2 - d^2 \end{bmatrix} \quad (2-52)$$

where  $l_x$ ,  $l_y$ , and  $l_z$  are the components of the landmark position  $\underline{l}$  computed in basic inertial coordinates at the time of measurement:  $T_{BO_2}$  is a  $2 \times 3$  matrix containing the first two rows of  $T_{BO}$ , and  $d = |\underline{l} - \underline{r}|$ .

As stated earlier, landmark position errors and MSS measurement errors are both modeled as noises in  $\alpha_M$  and  $\beta_M$ . The sensitivity of the landmark measurement to these errors is represented by the following matrix:

$$A_M = \frac{\partial \underline{l}_{MB}}{\partial \underline{v}_M} \left| \begin{array}{l} \alpha_M = \alpha_M^{\text{Meas}} \\ \beta_M = \beta_M^{\text{Meas}} \end{array} \right. = \begin{bmatrix} 0 & c\beta_M \\ -ca_M c\beta_M & sa_M c\beta_M \end{bmatrix} \quad (2-53)$$

#### Range Measurement

Linearization of the range measurement equation yields:

$$H_R = \frac{\partial R_S}{\partial \underline{x}} \left| \begin{array}{l} \underline{x} = \underline{x}_0 \end{array} \right. = \frac{\partial}{\partial \underline{x}} (|\underline{r} - \underline{r}_T|) \left| \begin{array}{l} \underline{x} = \underline{x}_0 \end{array} \right. \quad (2-54)$$

$$H_R = (0, 0, 0, 0, 0, 0, H_{Rx}, H_{Ry}, H_{Rz}, 0, 0, 0) \quad (2-55)$$

where the following equations are due to differentiation with respect to the state elements:

$$H_{Rx} = \frac{1}{R_s} (r_0 - r_{T0}) \quad (2-56)$$

$$H_{Ry} = \frac{1}{R_s} (r_1 - r_{T1}) \quad (2-57)$$

$$H_{Rz} = \frac{1}{R_s} (r_2 - r_{T2}) \quad (2-58)$$

Range measurement error is modeled as affected by two types of noises, first by the additive noise  $v_{R1}$  on the range measurement itself, and second by the noise  $v_{R2}$  due to uncertainty in tracking station ephemeris.\*

The sensitivity to the first noise is simply unity.

$$A_{R1} = \frac{\partial R_s}{\partial v_{R1}} = 1 \quad (2-59)$$

The sensitivity to tracking station ephemeris uncertainty modeled as white noise is:

$$A_{R2} = \frac{\partial R_s}{\partial v_{R2}} \left|_{\underline{r}_T=\underline{r}_{T0}} \right. = \frac{\partial}{\partial \underline{v}_{R2}} \left|_{\underline{r}_T=\underline{r}_{T0}} \right. \left| \underline{r} - \underline{r}_T \right| \left|_{\underline{r}_T=\underline{r}_{T0}} \right. \quad (2-60)$$

$$A_{R2} = - [H_{Rx}, H_{Ry}, H_{Rz}, 0, 0, 0] \quad (2-61)$$

where the  $H$ 's are given by Equations 2-56 through 2-58. Here the change in sign is due to the fact that differentiation is with respect to  $\underline{r}_T$  and not to  $\underline{r}$  as in the  $H$  equation.

The corresponding measurement noise variance equation for use in the Kalman update equation is:

$$R_R = A_{R1} R_1 A_{R1}^T + A_{R2} R_2 A_{R2}^T \quad (2-62)$$

\*Note here that the term "ephemeris" is used for a tracking station on the ground or in orbit.

where

$$R_1 = [\text{Var } (\text{RN})] \quad (2-63)$$

RN = the range measurement noise

$$R_2 = T_{IL} R_{eph} T_{IL}^T \quad (2-64)$$

and where  $R_{eph}$  is the tracking station ephemeris uncertainty covariance matrix in local vertical coordinates and  $T_{IL}$  is a transformation matrix from local vertical to basic inertial coordinates.

#### Range Rate Measurement

When the range rate equation (Equation 2-39) is linearized, the result is:

$$\dot{H}_R = \frac{\partial \dot{R}_s}{\partial \underline{x}} \Big|_{\underline{x}=\underline{x}_0} = \frac{\partial}{\partial \underline{x}} \left[ \frac{(\underline{v} - \underline{v}_T) \cdot (\underline{r} - \underline{r}_T)}{|\underline{r} - \underline{r}_T|} \right] \Big|_{\underline{x}=\underline{x}_0} \quad (2-65)$$

$$\dot{H}_R = (0, 0, 0, 0, 0, 0, H_{Rx}, H_{Ry}, H_{Rz}, H_{Rx}^*, H_{Ry}^*, H_{Rz}^*) \quad (2-66)$$

where the following equations are obtained by differentiation with respect to the state elements:

$$H_{Rx}^* = \frac{1}{R_s^2} [R_s (v_0 - v_{T0}) - \dot{R}_s (r_0 - r_{T0})] \quad (2-67)$$

$$H_{Ry}^* = \frac{1}{R_s^2} [R_s (v_1 - v_{T1}) - \dot{R}_s (r_1 - r_{T1})] \quad (2-68)$$

$$H_{Rz}^* = \frac{1}{R_s^2} [R_s (v_2 - v_{T2}) - \dot{R}_s (r_2 - r_{T2})] \quad (2-69)$$

$$H_{RX}^{\cdot \cdot} = \frac{1}{R_s} (\underline{r}_0 - \underline{r}_{T0}) \quad (2-70)$$

$$H_{RY}^{\cdot \cdot} = \frac{1}{R_s} (\underline{r}_1 - \underline{r}_{T1}) \quad (2-71)$$

$$H_{RZ}^{\cdot \cdot} = \frac{1}{R_s} (\underline{r}_2 - \underline{r}_{T2}) \quad (2-72)$$

Range rate measurement uncertainty is also modeled as affected by two types of noises. First is the noise  $v_3$  in the doppler measurement itself, and second is the noise  $\underline{v}_{R2}$  due to tracking station ephemeris uncertainty.

The sensitivity to the first noise is simply unity.

$$A_{R1}^{\cdot} = \frac{\partial R_s}{\partial v_3} = 1 \quad (2-73)$$

The sensitivity to tracking station ephemeris uncertainty is:

$$A_{R2}^{\cdot} = \frac{\partial R_s}{\partial \underline{v}_{R2}} \left| \begin{array}{l} \underline{r}_T = \underline{r}_{T0} \\ \underline{v}_T = \underline{v}_{T0} \end{array} \right. = \frac{\partial}{\partial \underline{v}_{R2}} \left[ \frac{(\underline{v} - \underline{v}_t) \cdot (\underline{r} - \underline{r}_t)}{|\underline{r} - \underline{r}_t|} \right] \left| \begin{array}{l} \underline{r}_T = \underline{r}_{T0} \\ \underline{v}_T = \underline{v}_{T0} \end{array} \right. \quad (2-74)$$

and

$$A_{R2}^{\cdot} = - [H_{RX}^{\cdot \cdot}, H_{RY}^{\cdot \cdot}, H_{RZ}^{\cdot \cdot}, H_{RX}^{\cdot \cdot \cdot}, H_{RY}^{\cdot \cdot \cdot}, H_{RZ}^{\cdot \cdot \cdot}] \quad (2-75)$$

where the  $H$ 's are given by Equations 2-67 through 2-72. Here the change in sign is due to the fact that differentiation is with respect to  $\underline{r}_T$  and  $\underline{v}_T$  and not  $\underline{r}$  and  $\underline{v}$ .

The corresponding measurement noise variance equation for use in the Kalman update equation is:

$$R_R^* = A_{R1}^* R_3 A_{R1}^{*T} + A_{R2}^* R_4 A_{R2}^{*T} \quad (2-76)$$

where

$$R_3 = [\text{Var } (\text{RRN})] \quad (2-77)$$

RRN = the range rate measurement uncertainty

$$R_4 = T_{IL} R_{eph} T_{IL}^T \quad (2-78)$$

where  $R_{eph}$  and  $T_{IL}$  have been defined previously.

#### Star Tracker Measurement

Linearization of the estimated star tracker measurement equation yields the following:

$$\begin{aligned} H_T &= \frac{\partial}{\partial \underline{x}} \left[ \begin{bmatrix} T_{BO} \end{bmatrix} \right] \underline{x} = \underline{x}_0^T T_{OI} \underline{s}_I \\ &= \begin{bmatrix} H_\theta & H_\phi & H_\psi & 0 & 0 & 0 & 0 & 0 & 0 & 0 & 0 & 0 \\ -\theta & -\phi & -\psi & 1 & 0 & 0 & 0 & 0 & 0 & 0 & 0 & 0 \\ 0 & 0 & 0 & 0 & 0 & 0 & 0 & 0 & 0 & 0 & 0 & 0 \end{bmatrix} \end{aligned} \quad (2-79)$$

where

$$H_\theta = \begin{bmatrix} -c\theta & -s\theta & 0 \\ 0 & 0 & 0 \end{bmatrix} \quad T_{OI} \underline{s}_I \quad (2-80)$$

$$H_\phi = \begin{bmatrix} 0 & 0 & 0 \\ -c\phi & -s\phi & 0 \end{bmatrix} \quad T_{OI} \underline{s}_I \quad (2-81)$$

$$H_\psi = \begin{bmatrix} 0 & 0 & 1 \\ -s\psi & c\psi & 0 \end{bmatrix} \quad T_{OI} \underline{s}_I \quad (2-82)$$

The measurement angles of the star tracker are:

$$\begin{aligned} \alpha_{T_{Meas}} &= \alpha_{T_{True}} + v_{\alpha_T} \\ \beta_{T_{Meas}} &= \beta_{T_{True}} + v_{\beta_T} \end{aligned} \quad (2-83)$$

\*See footnote on page 2-20.

where  $v_{\alpha_T}$  and  $v_{\beta_T}$  are the random measurement errors which may be expressed as the components of the random vector

$$\underline{v}_{ST} = \begin{bmatrix} v_{\alpha_T} \\ v_{\beta_T} \end{bmatrix} \quad (2-84)$$

whose covariance matrix  $R_T$  is defined as follows:

$$E(\underline{v}_{ST}\underline{v}_{ST}^T) = R_T \delta(t - \tau) = \begin{bmatrix} \sigma_{\alpha_T}^2 & 0 \\ 0 & \sigma_{\beta_T}^2 \end{bmatrix} \delta(t - \tau) \quad (2-85)$$

The sensitivity of the star measurement to the random errors is:

$$A_T = \frac{\partial s_B}{\partial \underline{v}_{ST}} \left| \begin{array}{l} \alpha_T = \alpha_{T_{Meas}} \\ \beta_T = \beta_{T_{Meas}} \end{array} \right. = \begin{bmatrix} -s\beta_T & s\alpha_T & c\beta_T & c\alpha_T \\ -c\alpha_T & 0 \end{bmatrix} \quad (2-86)$$

REPRODUCIBILITY OF THE  
ORIGINAL PAGE IS POOR

## 2.6 KALMAN FILTER EQUATIONS

The equations for the filterering technique are the extended Kalman Bucy equations for discrete measurements. These equations consist of two parts: 1) propagation between measurements, and 2) updating whenever a measurement is taken. Since the linearized state equations in this study lend themselves to a closed-form solution, the transition matrix  $\Phi(t_k, t_{k-1})$  of Equation 2-35 can be used for propagation of the covariance matrix from one measurement to the next as follows, where a new notation is adopted so that subscripts k and k-1 denote the times of measurement ( $t_k$  and  $t_{k-1}$ ):

$$P_k' = \Phi_{k,k-1} P_{k-1} \Phi_{k,k-1}^T + G_k Q_k G_k^T \quad (2-87)$$

where

$P_{k-1}$  - updated covariance matrix at time  $t_{k-1}$

$P_k'$  - covariance matrix at  $t_k$  before updating

$G_k, Q_k$  - are defined in Equations 2-32 and 2-18.

The updating equation at time  $t_k$  is given by:

$$P_k = P_k' - K_k H_k P_k' \quad (2-88)$$

where

$K_k$  is the Kalman gain matrix defined by

$$K_k = P_k' H_k^T [P_k + H_k P_k' H_k^T]^{-1} \quad (2-89)$$

Recursive solution of Equations 2-87, 2-88, and 2-89 provides the filtered value of the covariance matrix at any desired time.

## 2.7 CONSIDER STATE EQUATIONS

### 2.7.1 Introduction

Optimal performance of the Kalman filter depends on accurate description of the statistics of the measurements involved. This implies that the estimator should accurately model all real world states. It may develop that some states can be neglected because they are truly negligible. In other cases the statistics of the states may be poorly known or the states may incorporate non-zero biases. Here the attempt to incorporate poorly modeled states in the estimator may result in poor performance, since the estimator is trying to fit the data to an incorrect model.

A useful approach is to have the estimator "consider" the effect of poorly modeled states (but not to make estimates of them) when estimating the "desired" states. An important advantage of this approach is that the number of estimated states is not expanded while the effects of "consider" states are still taken into account.

### 2.7.2 Consider State Equations

The equations for the estimation problem with "consider" states are as follows:

Define

$$\underline{x}_T = \begin{bmatrix} \underline{x} \\ \underline{x}_C \end{bmatrix} \quad (2-90)$$

where

$\underline{x}$  is the twelve dimensional vector defined by  
Equation 2-12

$\underline{x}_C$  is the " consider" portion of the new state vector

The covariance matrix for  $\underline{x}_T$  is:

$$P_C = \begin{bmatrix} P & C_P \\ C_P^T & W \end{bmatrix} \quad (2-91)$$

where  $P = E(\underline{x} \underline{x}^T)$  (2-92)

$$W = E(\underline{x}_C \underline{x}_C^T) \quad (2-93)$$

$$C_P = E(\underline{x} \underline{x}_C^T) \quad (2-94)$$

### 2.7.3 Consider State Dynamics

Since a circular orbit with a nominal attitude history is assumed in this study, a transition matrix can be used here for propagation of the covariance matrix. The covariance propagation equation for the state  $\underline{x}_T$  is

$$P_C' = \Phi_T P_C \Phi_T^T + G_T Q_T G_T^T \quad (2-95)$$

(where the subscripts k and k-1, to denote times of measurement, are omitted for simplicity) and where

$P_C$  - covariance matrix at time  $t_{k-1}$  after update,  
(before propagation)

$P_C'$  - covariance matrix at time  $t_k$  after propagation,  
(before update)

$$Q_T = \begin{bmatrix} 0 & 0 \\ 0 & Q_C \end{bmatrix} \quad (2-96)$$

$$G_T = \begin{bmatrix} G & 0 \\ 0 & G_C \end{bmatrix} \quad (2-97)$$

$Q_c$  - white noise matrix associated with the consider states

$G_c$  - identity matrix (12 x 12 here)

$$\Phi = \begin{bmatrix} \Phi & 0 \\ 0 & \Phi_c \end{bmatrix} \quad (2-98)$$

where  $\Phi_c$  is the consider state transition matrix.

Substituting Equations 2-91 and 2-97 into 2-95, we obtain for the propagated covariance matrix the following:

$$P'_c = \begin{bmatrix} P' & C_p' \\ C_p'^T & W' \end{bmatrix} \quad (2-99)$$

where

$$P' = \Phi P \Phi^T + G Q G^T \quad (2-100)$$

$$C_p' = \Phi C_p \Phi_c^T \quad (2-101)$$

$$W' = \Phi_c W \Phi_c^T + G_c Q_c G_c^T \quad (2-102)$$

For the present study the consider states are taken to be the ephemeris uncertainties in position and velocity associated with each of the two TDRSS satellites stationed over the equator.

The consider state transition matrix,  $\Phi_c$ , is then given by:

$$\Phi_c = \begin{bmatrix} \Phi_{c1} & 0 \\ 0 & \Phi_{c2} \end{bmatrix} \quad (2-103)$$

where  $\Phi_{c1}$  and  $\Phi_{c2}$  are the six-by-six transition matrices associated with the ephemeris uncertainties for each of the two TDRSS satellites. These matrices are identical in form to the transition matrix given in Equation 2-34 for the EOS ephemeris state. In this case the term  $\omega_o$  of Equation 2-34 is the orbital rate of TDRSS.

#### 2.7.4 Consider State Measurement Equations

The measurement equation incorporating the consider states is:

$$\underline{z} = [H \mid H_C] \begin{bmatrix} \underline{x} \\ \underline{x}_C \end{bmatrix} + A_T \underline{n} \quad (2-104)$$

or

$$\underline{z} = H_T \underline{x}_T + A_T \underline{n} \quad (2-105)$$

where

$$H_T = [H \mid H_C] \quad (2-106)$$

and

$H$  is the sensitivity of the measurement to the state,  $\underline{x}$ .

$H_C$  is the sensitivity of the measurement to the consider state,  $\underline{x}_C$ .

#### 2.7.5 Consider State Filter Equations

The Kalman filter equations for the covariance are as follows where the updating equation at time,  $t_k$ , is given by:

$$P_C' = P_C' - K_T H_T P_C' \quad (2-107)$$

where  $P_C'$  and  $P_C$  are the covariance matrices before and after updating,

and

$$K_T = P_C' H_T^T [H_T P_C' H_T^T + R_T]^{-1} \quad (2-108)$$

$$R_T = A_T F [\underline{n} \underline{n}^T] A_T^T \quad (2-109)$$

Here there is no interest in updating the consider state,  $\underline{x}_c$ , but only the state,  $\underline{x}$ . Therefore, only those rows of  $K_T$  which pertain to  $\underline{x}$  are calculated. This gain is called  $K_x$ . That is, choose  $K_T$  such that:

$$K_T = \begin{bmatrix} K_x \\ 0 \end{bmatrix} \quad (2-110)$$

Combining Equations 2-91 and 2-106 yields:

$$K_x = (P_T H^T + C_p' H_c^T)^{-1} (H_T P_c' H_T^T + R_T) \quad (2-111)$$

where

$$H_T P_c' H_T^T + R_T = H P' H^T + H C_p' H_c^T + H_c C_p'^T H^T + H_c W H_c^T + R_T \quad (2-112)$$

The updating equations for  $P$ ,  $C_p$  and  $W$  can be shown to be

$$P = P' - K_x (H P' + H_c C_p'^T), \quad (2-113)$$

$$C_p = C_p' - K_x (H C_p' + H_c W'), \quad (2-114)$$

$$W = W'. \quad (2-115)$$

It should be noted that the update in Equation 2-114 should be carried out even if the consider state sensitivity  $H_c$  is zero, such as would be the case when landmark measurements are used.

## 2.8 ERROR STUDY RESULTS

### 2.8.1 Introduction

The results presented in this section give performance data on the landmark, range and range-rate update configuration. The previous report, Interim Technical Report No. 2<sup>(1)</sup>, had presented results on the landmark-star configuration.

The present study assumes radar range and range-rate measurements made by either (1), two ground tracking stations (located at Merritt Island, Florida and Goldstone, California), or (2), two TDRSS<sup>(1)</sup> geosynchronous navigational satellites located over the equator. Most of the results are generated for landmark observation case 2, which includes two passes over the continental USA. (See Figure 2-4). The material presented in Section 2.8.5 shows that additional passes over the USA and Alaska have a relatively small effect on reducing estimation uncertainties. Figure 2-5 illustrates the four-pass case and Table 2-1 briefly describes all of the cases used in the study.

The landmark location data is generated artificially, since no realistic data was conveniently available nor was considered necessary for this type of study. Most performance results are generated using only two landmark updates per pass over the continental USA. The landmark location data is obtained at points within the USA by selecting random values of the multi-spectral scanner (MSS) beam angle. The maximum scan beam angle is  $\pm 4.8^\circ$  corresponding to  $\pm 45$  miles on the ground. (See Figure 2-1). The landmarks are located near the north and south USA borders for the given pass.

For the ground tracking station simulations, five simultaneous range and range-rate updates per pass are assumed. The first pass is tracked by Merritt Island and the second by Goldstone. Minimum allowable radar beam elevation is 5 degrees. For the simulations with TDRSS tracking, eighteen simultaneous range and range-rate measurements by both TDRSS stations are assumed. The TDRSS satellites are located at 41 and 171 degrees west longitude over the equator. More TDRSS measurements are possible because of the greater coverage of EOS orbits from the vantage point of the TDRSS satellites.

2-34

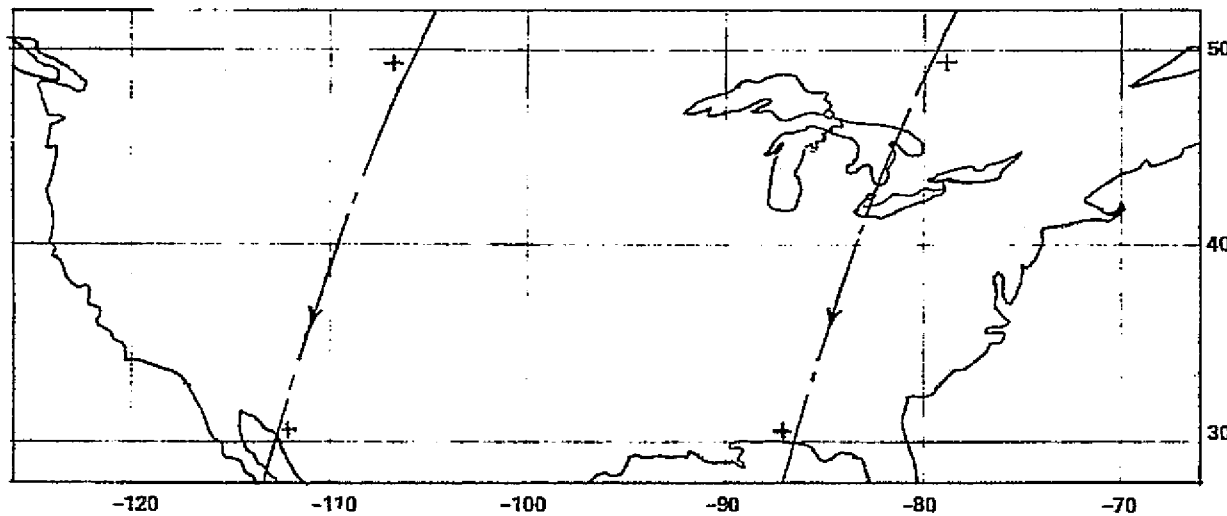


Figure 2-4 Landmark Observation Case 2

2-35

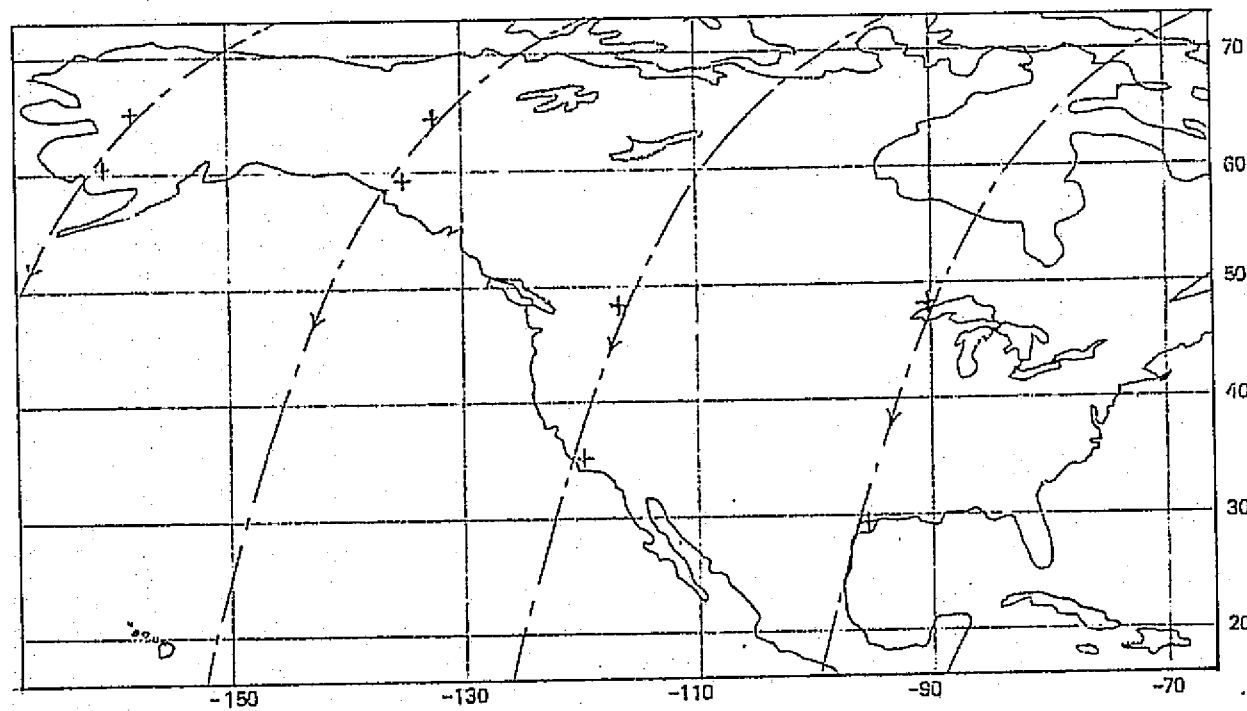


Figure 2-5 Landmark Observation Case 4

TABLE 2-1  
LANDMARK OBSERVATION CASES

Case Number	Pass Number	North Latitude (deg)		Region*
		At Start	At End	
1	1	50	30	USA
2	1	50	30	USA
	2	50	30	↓
3	1	50	45	USA
	2	50	30	↓
	3	50	45	↓
4	1	50	30	USA
	2	50	30	↓
	3	65	60	Alaska
	4	65	60	↓
5	1	50	45	USA
	2	50	30	↓
	3	50	45	Alaska
	4	65	60	↓
	5	65	60	↓

\*USA denotes continental USA.

For the comparative simulations using a star tracker, only one type of star tracker is assumed. This is the body fixed 8° square FOV tracker which electronically tracks a star as it passes through the FOV. For the relevant runs the stars are chosen at equal orbital intervals (20 stars per orbit) with randomized locations within the tracker's field of view.

The performance results presented here are generally the uncertainties in the Kalman filtered estimates of spacecraft attitude, gyro bias drift and orbital ephemeris after processing landmark, range and range-rate measurements for two passes. The results are the square roots of the principal diagonal terms of the 12 x 12 covariance matrix. They provide a good statistical indication of performance in estimating the state parameters.

#### 2.8.2 Nominal Values Used in Study

Unless otherwise stated, the nominal values of the error sources and parameters used to generate the performance results are as given here. Although some of the values may not represent the best or latest estimates, it is felt that they are satisfactory for the present study.

The landmark measurement uncertainty used in this study (15 meters) is a composite number representing both uncertainty in the landmark location in Earth coordinates and uncertainty in the multi-spectral scanner measurement. Two assumptions are made concerning the landmark. First it is assumed to have no associated recognition process errors, and secondly it is assumed to be essentially a point source. These requirements are met by the searchlight landmark described in Reference 1. There are four basic uncertainty sources in this measurement, namely:

- 1) artificial landmark surveying errors,
- 2) earth pole wander and rotation rate variations,
- 3) MSS resolution,
- 4) scan rate and timing errors.

The uncertainty numbers associated with each of these sources are somewhat arbitrary, for example surveying accuracy can be increased in steps by applying more and more sophisticated techniques.

Estimates for the uncertainty in each category are as follows:

surveying	10 meters,
earth wobble	3 meters,
MSS resolution	10 meters,
scan errors	4 meters.

The root sum-of-square value for these uncertainties is 15 meters. Further discussion of the sources of these numbers is given in section 3.3.

The nominal values for uncertainties in the range and range-rate measurements (10 meters and 0.012 meter/sec) include both biases and white noises in the measurements. Because of the limitations imposed upon the present study the radar biases are not modeled separately as estimatable states or as consider biases, since more extensive analysis and simulations would have been required. Although the data given in the literature for these noises varies somewhat, it is felt that the above values are reasonable selections.

The nominal value for ground tracking station location uncertainty is assumed to be 5 meters along each axis. This figure has been chosen because Merritt Island and Goldstone are particularly well surveyed, although the nominal location uncertainty for all USBS (United-S Band System) radars is 10 meters.

#### TDRSS Ephemeris Uncertainties

The choice of a suitable TDRSS ephemeris uncertainty covariance is a difficult problem. The only available TDRSS uncertainty covariance was printed in a 1971 report<sup>(11)</sup> on the TDRSS system. This covariance was reprinted in a 1973 NASA report on "Navigation Systems Characteristics, Rev 1".<sup>(12)</sup> However this covariance may have reproduction errors since one of the cross-correlation coefficients is greater than unity. Nevertheless this covariance is used in the TDRSS simulations after appropriate modification.

Two other TDRSS ephemeris uncertainty covariances are also used in the simulations for comparative purposes. Data for the first covariance was obtained from GSFC and represents a somewhat pessimistic estimate. These assume position uncertainties about four times greater than for the first covariance. Data for the second covariance anticipates future state-of-the-art improvements in determination of TDRSS ephemeris. Here position uncertainties are about 50 times smaller than for the first set of uncertainties.

#### Gravitational Harmonic Uncertainties

All covariance runs made for this study include the effects of uncertainties in the gravitational harmonic C & S coefficients as well as in the gravitational constant,  $\mu$ . A separate study was first undertaken where the term-by-term differences between the most recent Smithsonian gravitational models (SEII (1969) and SEIII (1973)) were treated as if equivalent to one sigma uncertainties, and where the gravitational constant uncertainty was 0.2 PPM. The effect on the computed EOS orbit beyond radar coverage (for both GTS and TDRSS) was determined for each term. It was found incidentally that the C and S coefficients having the most significant effect on EOS orbit were those associated with the following n, m pairs: 2,2; 3,3; 5,5; 6,2; 6,5; 6,6; 8,7. By summing the ephemeris error results of numerous Monte Carlo runs for which the C and S coefficients were randomized, an uncertainty covariance matrix was obtained that represented the ephemeris uncertainties at the point that radar coverage commences prior to passage over the USA. This covariance was then scaled to match data obtained from GSFC for 5 orbits.

With ground tracking coverage, the square roots of the uncertainty covariance diagonals were as follows:

(altitude, down range, crosstrack):

(2.6, 14.3, 3.3, .013, .003, .002) meters, meters/sec

With TDRSS tracking, because of better coverage, the corresponding uncertainties were:

(3.0, 6.8, 7.8, .007, .003, .003) meters, meters/sec

For the 12-state covariance simulation studies this ephemeris uncertainty covariance matrix was summed with the propagated 12-state covariance at the point for each pass when radar coverage commences prior to USA passage.

The nominal values of the error sources and parameters are as follows:

Initial State Uncertainties ( $1\sigma$ )

Attitude (Pitch, Roll, Yaw)	-	60 arcsec (each)
Gyro Bias Drift	-	0.03 deg/hr (each)
<b>Ephemeris Position</b>		
Attitude	-	20 meters
Downrange	-	50 meters
Crosstrack	-	20 meters
<b>Ephemeris Velocity</b>		
Altitude	-	0.05 meter/sec
Downrange	-	0.02 meter/sec
Crosstrack	-	0.02 meter/sec

Gyro Error Sources ( $1\sigma$ )

Random Drift	-	0.01 deg/hr (white noise)
Quantization	-	0.1 arcsec

Landmark Measurements ( $1\sigma$ )

Landmark Position	-	
Downrange	-	15 meters
Crosstrack	-	15 meters

8° FOV Star Tracker

Measurement Error ( $1\sigma$ )	5 arcsec/axis
Field-of-View	8 x 8 degrees
Pointing Direction	towards zenith
Star Distribution	star randomly selected in FOV after each 18 degrees of orbital motion

Range and Range Rate Measurements ( $1\sigma$ )

Slant Range	10 meters
Slant Range Rate	0.012 meter/sec
GTS Location	5 meters (each)
TDRSS Ephemeris (Position & Velocity;	
Altitude, Downrange, Crosstrack)	
1971 Report	
(15, 276, 128; .020, .001, .009) meter,meter/sec	
GSFC	
(150, 1000, 500; .073, .011,.036) meter,meter/sec	
Future State-of-the-Art	
(5, 5, 5;.00037,.00037,.00037)     meter,meter/sec	

Gravitational Coefficient Uncertainties ( $1\sigma$ )

Gravitational Constant, $\mu$	0.2 PPM
C&S Coefficients	(See previous comments)

Normal Conditions for Observation Runs

Landmark Observation Case 2 (Includes 2 passes over continental USA)

2 Landmark updates per pass

5 Range and Range Rate updates (simultaneous) by Merritt Island on first pass and by Goldstone on second pass

Run starts at equator at  $98^\circ$  east longitude on ascending node and passes over north polar region before making first pass over USA

Run ends just south of last landmark update on second pass over USA

2.8.3 Comparative Results with Different Measurement Configurations

Before presenting the results obtained with different measurement configurations, it will be useful to show the effects of using a single type of measurement for updating the estimation uncertainties.

Table 2-2 gives performance data after processing with a single type of measurement. All data presented includes the effects of two passes over the USA.

For comparison the state uncertainties for the case where no measurements are made are presented in the first row of Table 2-2. In this case the covariance matrix of uncertainties is simply propagated without update with any measurements. The increase in attitude uncertainty is due to the uncertainty in gyro bias drift, while the increase in satellite altitude and downrange position uncertainty is due to the effect of initial altitude uncertainties on the computed gravity feedback.

The next row shows the effect of star sightings with the 8° FOV star tracker where it is assumed that 20 stars per orbit could be seen with the tracker. The results show a very significant decrease in the attitude and gyro bias drift uncertainties. However the ephemeris uncertainties were not improved at all. This is because star sightings do not provide any information on satellite position.

The third row of Table 2-2 gives the effects of measurements of known landmarks where two landmark updates per pass over the continental USA were used. The results show only a moderate decrease in attitude and drift uncertainties and a relatively slight decrease in ephemeris uncertainties. Note that the pitch attitude and ephemeris uncertainties are greater than their initial values.

The next row shows the effect of range and range rate measurements by ground tracking stations (Merritt Island and Goldstone) where it was assumed that the range and the range rate measurements were made simultaneously. The results contrast sharply with those for star sightings. Here there is a very significant decrease in ephemeris uncertainties, while there is no improvement in attitude and gyro bias drift uncertainties. The last row also shows the effect of range and range rate measurements taken from the planned geosynchronous Tracking and Data Relay Satellite System (TDRSS). Although more measurements per pass (18) were made (because of better coverage of the EOS orbit by TDRSS), the performance is markedly inferior to that with ground tracking. This is primarily due to the relatively large initial ephemeris uncertainties assumed for the TDRSS satellites. This will be discussed in the next subsection.

TABLE 2-2  
KALMAN FILTER PERFORMANCE WITH  
SINGLE TYPES OF MEASUREMENTS

Type of Measurement	State Estimation Uncertainties ( $1\sigma$ )											
	Attitude (arcsec)			Gyro Bias Drift ( $10^{-3}$ deg/hr)			Position (meters)			Velocity (meters/sec)		
	Pitch	Roll	Yaw	X	Y	Z	Alt.	Range	Track	Alt.	Range	Track
<u>Initial State Uncertainties:</u>												
	60	60	60	30	30	30	20	50	20	.05	.02	.02
No Measurements	273	83	83	30	30	30	101	745	20.5	.749	.075	.020
Stars	2.0	1.8	14.9	15	0.4	1.0	101	745	20.5	.749	.075	.020
Landmarks	94	4.7	26.8	24	12	22	57	460	20.0	.482	.039	.020
Range and Range Rate (GTS)	273	83	83	30	30	30	2.8	4.6	7.8	.012	.003	.020
Range and Range Rate (TDRSS)	273	83	83	30	30	30	10.1	44.4	16.8	.040	.010	.016

Notes: Nominal number of measurements per pass or per orbit  
are assumed for each measurement type. See Section 2.7.2  
GTS - Ground Tracking Station

Table 2-3 shows the performance for various measurement configurations. The first row shows the results when using both star sightings and known landmark measurements. The decrease in attitude uncertainty is due almost entirely to star information, since it is almost the same as with stars alone. However the decrease in attitude uncertainty enables the landmark information to be used more effectively to reduce the ephemeris uncertainty. The next three rows give the state uncertainties that result from a measurement configuration that combines known landmarks and range and/or range rate ground tracking. The decrease in ephemeris uncertainty is essentially the same with range and range-rate updates taken alone, as compared with the configuration where landmarks are included in the measurements. However the existence of range and range rate information enables the landmark measurements to be very effectively used to reduce the pitch and roll attitude uncertainties as well as the Y bias drift uncertainty. The other two rows show that range-rate measurements are more effective than range measurements in decreasing ephemeris uncertainties.

The next to last row of Table 2-3 gives the results of using stars and range and range-rate information with no landmarks. Here the decrease in attitude uncertainty is due entirely to star sightings, while the decrease in ephemeris uncertainty is due entirely to range and range rate information. The addition of landmark measurements to this configuration decreases attitude uncertainties slightly to the lowest uncertainty level of any combination considered.

#### 2.8.4 Comparative Results with Ground Tracking and TDRSS Satellites

Table 2-4 compares the performance of ground and TDRSS tracking for the cases with and without uncertainties in the positions of the ground stations or TDRSS. Landmark measurements were also used in all of these cases. The ground tracking stations had a nominal location uncertainty of 5 meters per axis. The TDRSS satellites were assumed to have initial ephemeris uncertainties of 15, 276, 128;.020, .001, .009 meters and meters/sec in altitude, downrange and crosstrack. The associated covariance matrix is from a 1971 report.<sup>(11)</sup> (See Section 2.8.2). For Table 2-4 the TDRSS ephemeris uncertainties are modeled as consider states.

TABLE 2-3  
KALMAN FILTER PERFORMANCE WITH  
DIFFERENT TYPES OF MEASUREMENTS

Types of Measurements	State Estimation Uncertainties ( $10^{-3}$ )											
	Attitude (arcsec)			Gyro Bias Drift ( $10^{-3}$ deg/hr)			Position (meters)			Velocity (meters/sec)		
	Pitch	Roll	Yaw	X	Y	Z	Alt.	Range	Track	Alt.	Range	Track
<u>Initial State Uncertainties:</u>												
	60	60	60	30	30	30	20	50	20	.05	.02	.02
Landmarks and Stars	2.0	1.7	14.9	15	0.4	1.0	15.0	15.3	10.2	.030	.015	.02
Landmarks & Range	3.2	3.0	26.8	24	0.7	22	6.6	9.2	10.6	.016	.007	.020
Landmarks & Range Rate	2.6	3.0	26.8	24	0.6	22	3.1	5.7	10.3	.014	.003	.020
Landmarks & Range & Range Rate	2.5	2.7	26.8	24	0.6	22	2.8	4.6	7.8	.012	.003	.020
Stars & Range & Range Rate	2.0	1.8	14.9	15	0.4	1.0	2.8	4.6	7.8	.012	.003	.020
Landmarks & Stars & Range & Range Rate	1.6	1.5	14.1	14	0.3	0.9	2.8	4.6	7.8	.012	.003	.020

Notes: Nominal number of measurements per pass or per orbit are assumed for each measurement type. See Section 2.7.2. Ground tracking stations used for range and range rate measurements.

TABLE 2-4  
KALMAN FILTER PERFORMANCE WITH  
GROUND AND TDRSS TRACKING STATION MEASUREMENTS

Tracking Station Ephemeris Uncertainties	State Estimation Uncertainties ( $1\sigma$ )					
	Attitude (arcsec)			Position (meters)		
	Pitch	Roll	Yaw	Alt.	Range	Track
Initial Uncertainties Are:	60	60	60	20	50	20
<u>Ground Tracking Stations</u>						
Zero Locat.Uncert.	2.4	2.5	26.8	2.1	2.8	6.6
Nom.Locat.Uncert.	2.5	2.7	26.8	2.8	4.6	7.8
<u>TDRSS Satellite Stations</u>						
Zero Ephem.Uncert.	3.2	2.3	26.6	4.8	11.2	3.1
Nom.Ephem.Uncert.	9.2	4.1	26.7	9.7	44.3	16.8

Note: All data obtained with nominal number of range  
and range rate and landmark measurements.  
TDRSS ephemeris uncertainties modelled as consider states.

Table 2-4 shows that with zero ground station and TDRSS location uncertainties, the position estimation uncertainties with TDRSS measurements compare favorably with ground tracking results, particularly in crosstrack. However with nominal ground station and TDRSS location uncertainties the position estimation uncertainties are markedly worse with TDRSS tracking. Note for example that the downrange position uncertainty is only slightly less than the initial uncertainty.

#### TDRSS Ephemeris Uncertainties Modeled as Consider States

The TDRSS ephemeris uncertainties are associated with a state that is highly time-correlated over the simulation time intervals of this study. Since the errors in this state will not undergo very much change during those time intervals, it is appropriate that they be modeled as consider state biases rather than as zero bias white noises. With this type of modeling the Kalman filter estimator "considers" the effect of imperfectly modeled states (but does not measure or estimate them) on the estimation of the "desired" states. Since the TDRSS ephemeris uncertainties may have non-zero means relative to the data intervals studied, the treatment of these uncertainties as "consider" states implies better modeling of the real world data. The analysis and equations for "consider" state propagation and update are presented in Section 2-7.

While it is better to model the TDRSS ephemeris uncertainties as consider states rather than as white noises, it is nevertheless of some interest to investigate Kalman filter performance with both modeling types. Table 2-5 compares estimation performance for the two types of modeling with three sets of initial TDRSS ephemeris uncertainties. These were given in Section 2.8.2 and are repeated here for the readers convenience. The three sets of initial ephemeris uncertainties are: (1) an adverse estimate obtained from GSFC, (2) a conservative estimate first given in a 1971 report, and (3) a future state-of-the-art estimate now being used in other unrelated CSDL studies. The one sigma ephemeris uncertainties in meters and meters per second for the three sets are:

TABLE 2-5  
KALMAN FILTER PERFORMANCE WITH  
DIFFERENT TDRSS EPHEMERIS UNCERTAINTIES

Tracking Station Ephemeris Uncertainties ( $1\sigma$ )	State Estimation Uncertainties ( $1\sigma$ )						
	Attitude (arcsec)			Position (meters)			
	Pitch	Roll	Yaw	Alt.	Range	Track	
<u>Initial Uncertainties Are:</u>							
		60	60	60	20	50	20
0		3.2	2.3	26.6	4.8	11.2	3.1
<u>With GSFC Ephemeris Uncertainties Modelled as:</u>							
Noises		23.7	4.2	27.0	18.9	114.4	17.7
Consider States		39.6	4.6	27.1	27.2	195.1	19.9
<u>With '71 Shuttle Study Ephemeris Uncertainties Modelled as:</u>							
Noises		6.5	2.8	26.7	9.7	30.0	8.4
Consider States		9.2	4.1	26.7	9.7	44.3	16.8
<u>With Future State-of-the-Art Ephemeris Uncertainties Modelled as:</u>							
Noises		3.3	2.3	26.6	4.9	11.9	3.3
Consider States		3.6	2.3	26.6	5.1	13.7	3.7

Note: All data obtained with nominal number of range  
and range rate and landmark measurements.

	Alt.	Dnrng.	Crtk.	$V_{alt}$	$V_{dnrng}$	$V_{crtk}$
GSFC conserv.	1)	150,	1000,	.500;	.073,	.011, .036
1971 rpt	2)	15,	276,	128;	.020,	.0011, .0025
Future est.	3)	5,	5,	5;	.00037,	.00037, .00037

Table 2-5 shows that the Kalman filter performance is consistently worse when the TDRSS ephemeris uncertainties are modelled as "consider" states than when modelled as white noise. This is to be anticipated, since use of "consider" states represents a more realistic modelling of possible biases. Table 2-5 also shows that with consider state modelling, the Kalman filter performance for ephemeris uncertainty estimation is only satisfactory with future state-of-the-art TDRSS ephemeris uncertainties. With 1971 Shuttle study uncertainties the downrange estimation uncertainty is only slightly less than the initial uncertainty.

### 2.8.5 Filter Performance for the Five Landmark Observation Cases

Table 2-6 presents the Kalman filter estimation uncertainties at the end of the last pass for the five different landmark observation cases. (See Table 2-1). Numerically these cases correspond to the number of passes over the continental USA, and if Case 4 or 5, over Alaska as well. To track the last two passes a third USBS radar tracking station located at Fairbanks, Alaska, is used for range and range rate measurements.

Table 2-6 shows that most of the improvement in performance is accomplished by the end of the second pass. Only slight improvement results as the number of passes is increased from two to five. In going from Case 2 to 3 it is noted that the ephemeris uncertainties did not decrease as one might expect. For example, the downrange uncertainty is 6.6 meters for Case 3, while it is 4.6 meters for Case 2. The reason for this irregularity lies in the choice of EOS orbital paths for the different cases. To make possible three observational passes over the continental USA (Case 3), a somewhat different inertial orbital path from that for Case 2 had to be used. Because of the different relationships of the EOS orbital paths with respect to the ground tracking stations for Cases 3 and 5, as opposed to those for Cases 2 and 4, the estimation uncertainties are moderately different from what they would have been if the same inertial orbital path had been used for all cases.

### 2.8.6 Kalman Filter Performance as a Function of Orbit Angle

#### Position Estimation Performance

Figures 2-6 and 2-7 show graphically the effect of propagation and update of the position estimation uncertainties for Cases 2 and 4 when using landmark measurements and ground tracking range and range rate measurements. For comparison, Figure 2-8 shows the position uncertainties for Case 2 when using star sightings and the same ground tracking measurements.

TABLE 2-6  
KALMAN FILTER PERFORMANCE FOR  
DIFFERENT LANDMARK OBSERVATION CASES

Landmark Observation	State Estimation Uncertainties ( $1\sigma$ )						
	Attitude (arcsec)			Position (meters)			
Case	Pitch	Roll	Yaw	Alt.	Range	Track	
<u>Initial Uncertainties Are:</u>							
	60	60	60	20	50	20	
1	3.7	5.2	34.3	12.3	9.7	19.2	
2 (nom)	2.5	2.7	26.8	2.8	4.6	7.8	
3	2.4	1.9	21.2	3.2	6.6	6.1	
4	2.0	1.9	18.4	2.3	3.6	6.2	
5	1.9	1.6	16.9	2.4	4.4	4.8	

Notes: 2 Landmark Updates/Pass

5 Range and Range Rate Updates/Pass by Ground Tracking

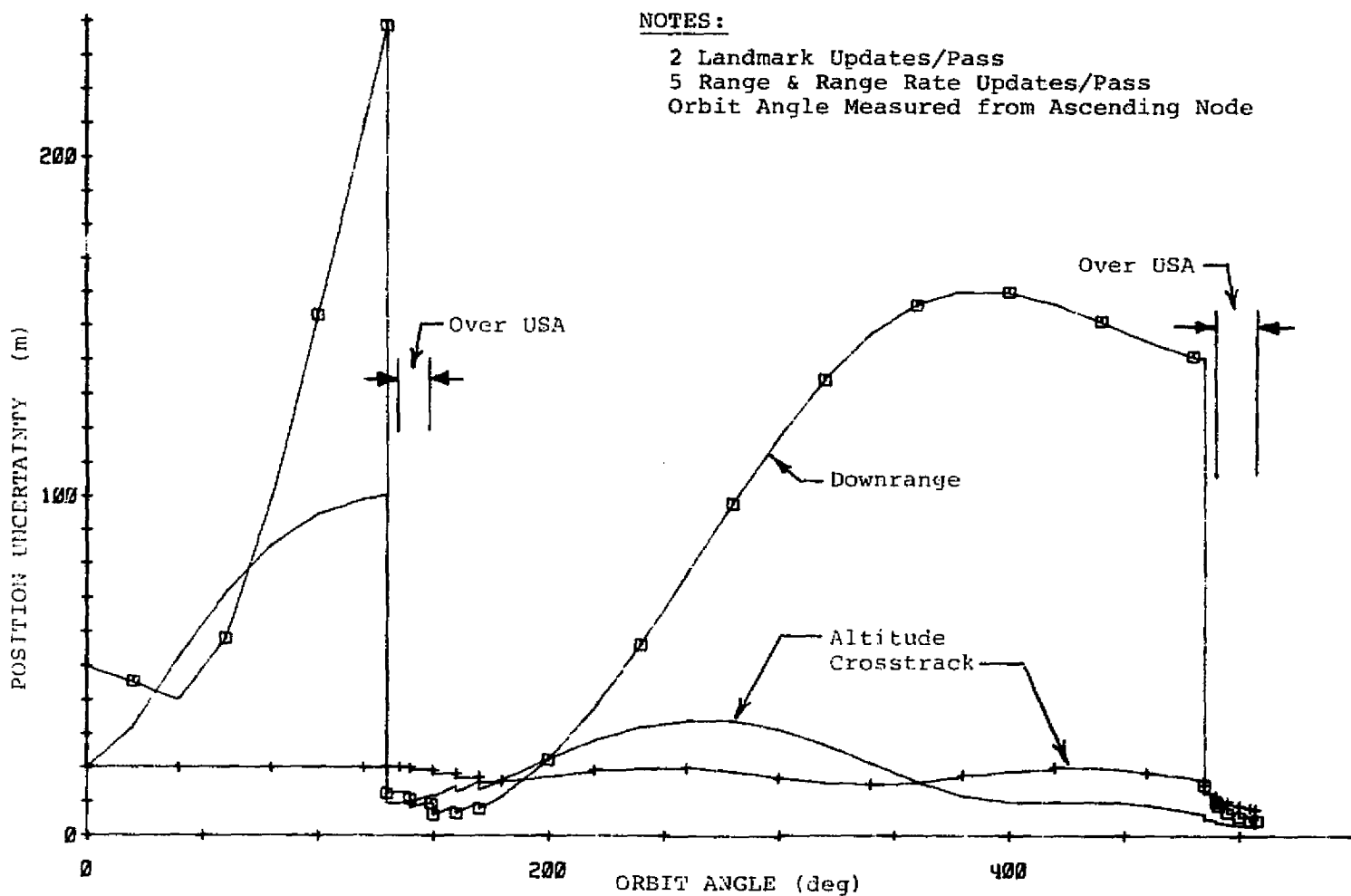


Figure 2-6 Kalman Filter Position Estimation Performance  
for Landmark Observation Case 2

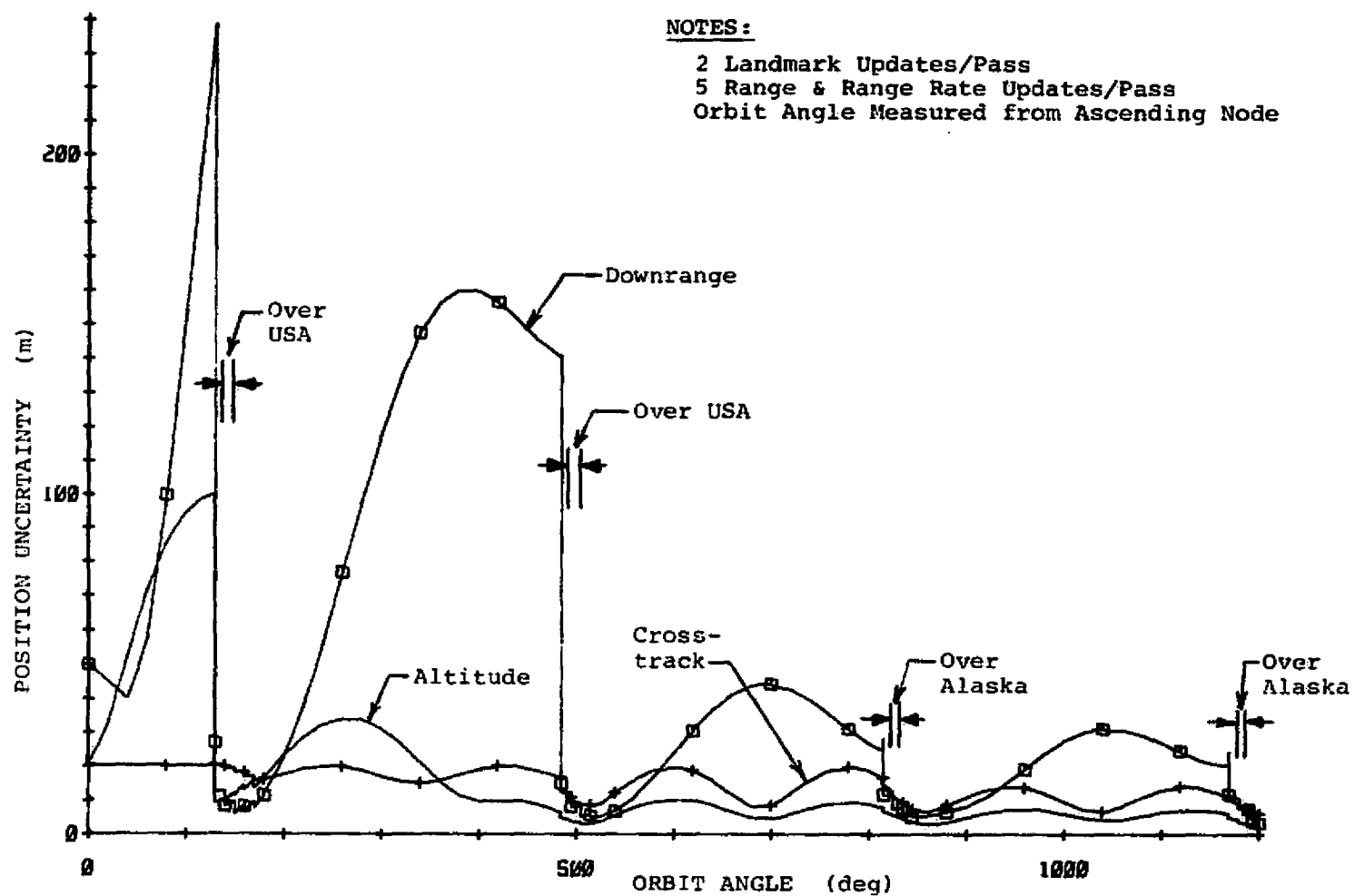


Figure 2-7 Kalman Filter Position Estimation Performance  
for Landmark Observation Case 4

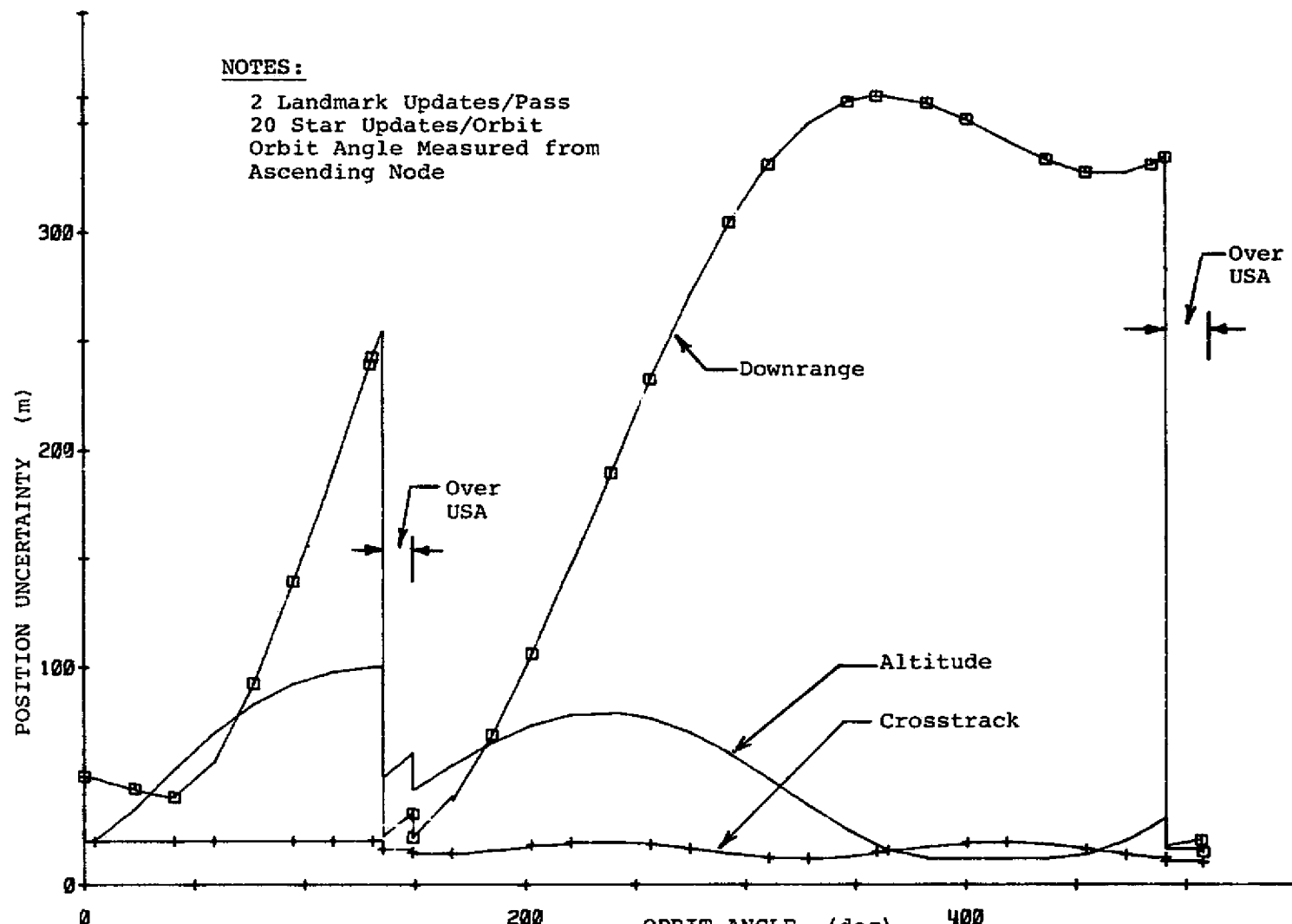


Figure 2-8 Kalman Filter Position Estimation Performance  
for Landmark Observation Case 2 with Star Sightings

Figures 2-6 and 2-7 show how effectively range and range rate measurements reduce the altitude and downrange position uncertainties on the first update of each pass for Cases 2 and 4. Subsequent updates on the same pass only reduce the uncertainties slightly. The marked increase in downrange uncertainty, and to a lesser extent the altitude position uncertainty, after the first USA pass is due to the presence of relatively large velocity estimation uncertainties. The operation of the Kalman filter on the velocity uncertainties is shown in Figure 2-7 by the marked reduction in peak downrange and altitude position uncertainties resulting after the second and third passes. The cross-track uncertainty is more cyclical than the other uncertainties. This uncertainty is progressively reduced after each pass.

Figure 2-8 shows graphically for Case 2 the effect of using star sightings with the same range and range rate measurements. It is seen here that the reduction in the downrange and altitude uncertainties at the start of each pass over the USA is not as dramatic as was the case in Figures 2-6 and 2-7 where landmarks were used.

#### Attitude Estimation Performance

Figures 2-9 and 2-10 show graphically the attitude estimation performance when using landmark, range, and range rate measurements. Figure 2-11 does the same with landmark and star measurements.

Note in Figures 2-9 and 2-10 that significant reductions occur in the attitude uncertainties (particularly those of pitch and roll) during the passes over the USA and Alaska. In these cases, the only information provided on attitude was that obtained from the landmark measurements during the passes over the USA and Alaska. Two landmark measurements were made on each pass. Most of the reduction in attitude uncertainty during a pass occurs during the first landmark update of each pass. In addition, it is seen that most of the reduction occurs in pitch and roll since the landmark is always near the local vertical. Note that the performance in Case 2 (Figure 2-9) is essentially the same as that of Case 4 (Figure 2-10) during the first two passes since Case 4 is essentially an extension of Case 2. Also note in Figure 2-10 that the uncertainty in pitch remains low and does not grow as rapidly

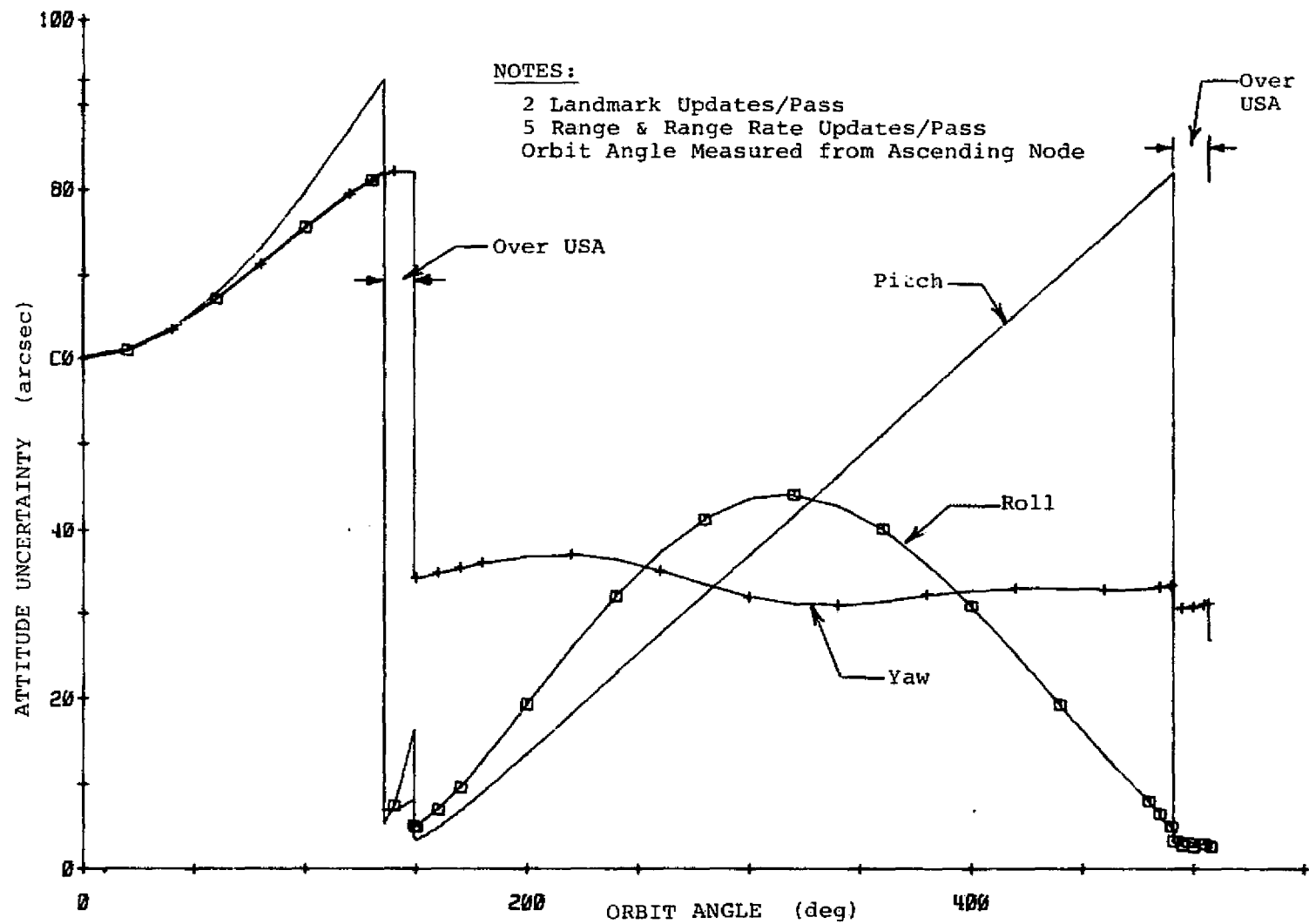


Figure 2-9 Kalman Filter Attitude Estimation Performance  
for Landmark Observation Case 2

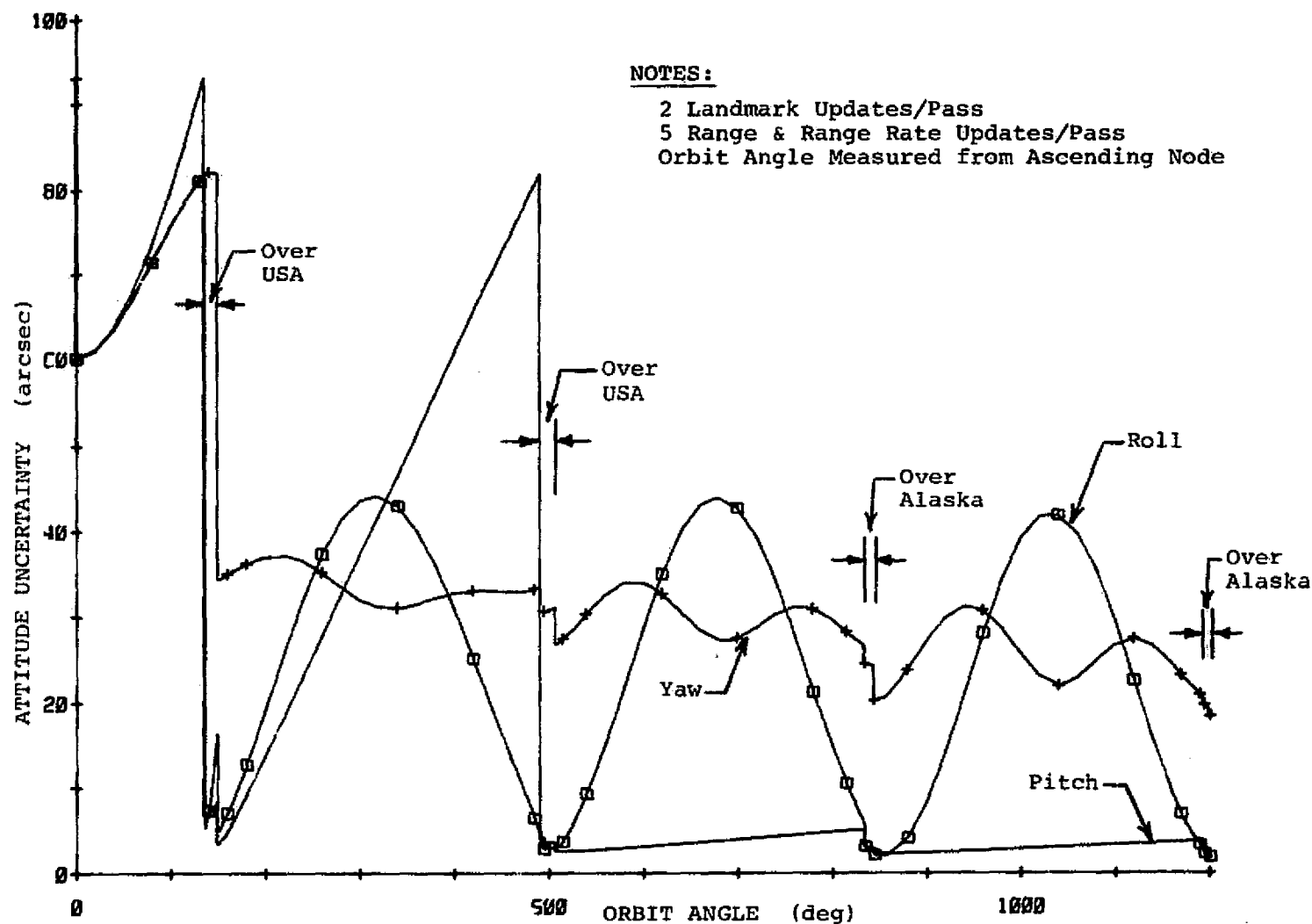


Figure 2-10 Kalman Filter Attitude Estimation Performance for Landmark Observation Case 4

after the second pass. This is due to the fact that the uncertainty of the Y (pitch) gyro bias drift was greatly improved by the updates of the second pass.

In Figures 2-9 and 2-10 it is seen that the roll and yaw uncertainties become oscillatory after the first pass. Note that the frequency in yaw is twice that in roll, and that there is a definite phase relationship between the two. The reason for the oscillatory behavior is due to a complex relationship between roll, yaw, roll gyro bias drift, and yaw gyro bias drift, and the fact that updates are made only during the passes over the continental USA and Alaska, which occur at somewhat the same portion of the satellite orbit.

In dramatic contrast to Figure 2-9 and 2-10, Figure 2-11, with star sightings in combination with landmark measurements, shows a very different performance in attitude estimation. This is primarily due to the fact that many more updates are made in attitude (20 star sightings per orbit plus 2 landmark measurements per pass). Note that the frequent updates of attitude throughout the orbit causes the uncertainties of all attitude components to reach almost steady state values after the first orbit.

#### 2.8.7 Performance Sensitivity to System Errors and Parameters

In this section the sensitivity of Kalman filter performance to various system uncertainties and parameters is investigated. These include the following:<sup>\*</sup>

- 1) Initial ephemeris uncertainty
- 2) Initial gyro bias drift uncertainty
- 3) Ground tracking station location uncertainty
- 4) Range measurement noise
- 5) Range rate measurement noise
- 6) Landmark position uncertainty
- 7) Number of range updates per pass
- 8) Number of range-rate updates per pass
- 9) Number of range and range-rate updates per pass

<sup>\*</sup>No data is presented on the sensitivity to initial spacecraft attitude uncertainties since the performance in estimating the ephemeris and attitude was virtually unaffected by values of these uncertainties up to 15 times nominal.

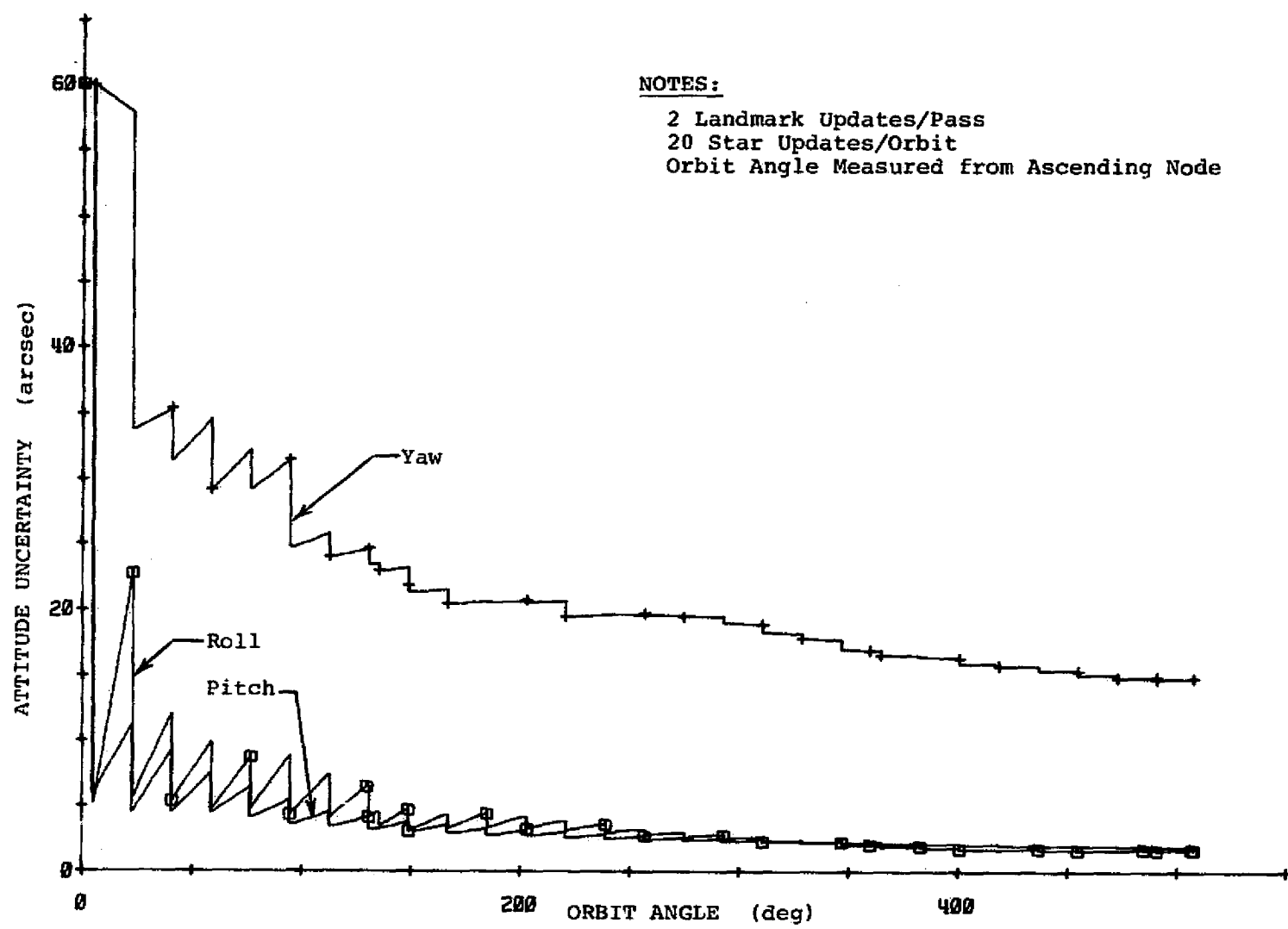


Figure 2-11 Kalman Filter Attitude Estimation Performance  
for Landmark Observation Case 2 with Star Sightings

- 10) Number of landmark updates per pass
- 11) Gyro random drift and quantization
- 12) Gravity harmonic uncertainties

These are considered separately in the following paragraphs.

#### Sensitivity to Initial Ephemeris Uncertainty

Figure 2-12 shows the effect of variation of the initial ephemeris uncertainty (all six components varied simultaneously) on position and attitude estimation uncertainties. This figure demonstrates that even when the initial ephemeris uncertainty is ten times its nominal value, the altitude and crosstrack position uncertainties are only slightly affected, while the downrange uncertainty is moderately increased. As might be expected the effect on the attitude uncertainties is negligible.

Figure 2-13 shows that only the yaw attitude uncertainty is affected by increases in the initial gyro bias drift uncertainty about all axes. In this case it is seen that the position estimation uncertainties remain unaffected.

#### Sensitivity to Ground Tracking Station Location Uncertainty

Figure 2-14 shows that the performance in estimating spacecraft position is strongly affected by an increase in the tracking station location uncertainty (assumed equal in all dimensions). For example, an increase in the location uncertainty from 5 (nominal) to 10 meters increases the downrange estimation uncertainty from 4.6 to 6.9 meters. This is to be expected since the location uncertainty effectively adds to the range measurement error.

#### Sensitivity to Range Measurement Noise

Figure 2-15 shows the effect of variation in the range measurement noise while maintaining nominal values for the errors in range rate and landmark measurements. It is seen that as the range measurement noise is increased, the performance in estimating spacecraft position levels off at values which happen to be those primarily obtained with range rate measurements alone. Note that there is little to be

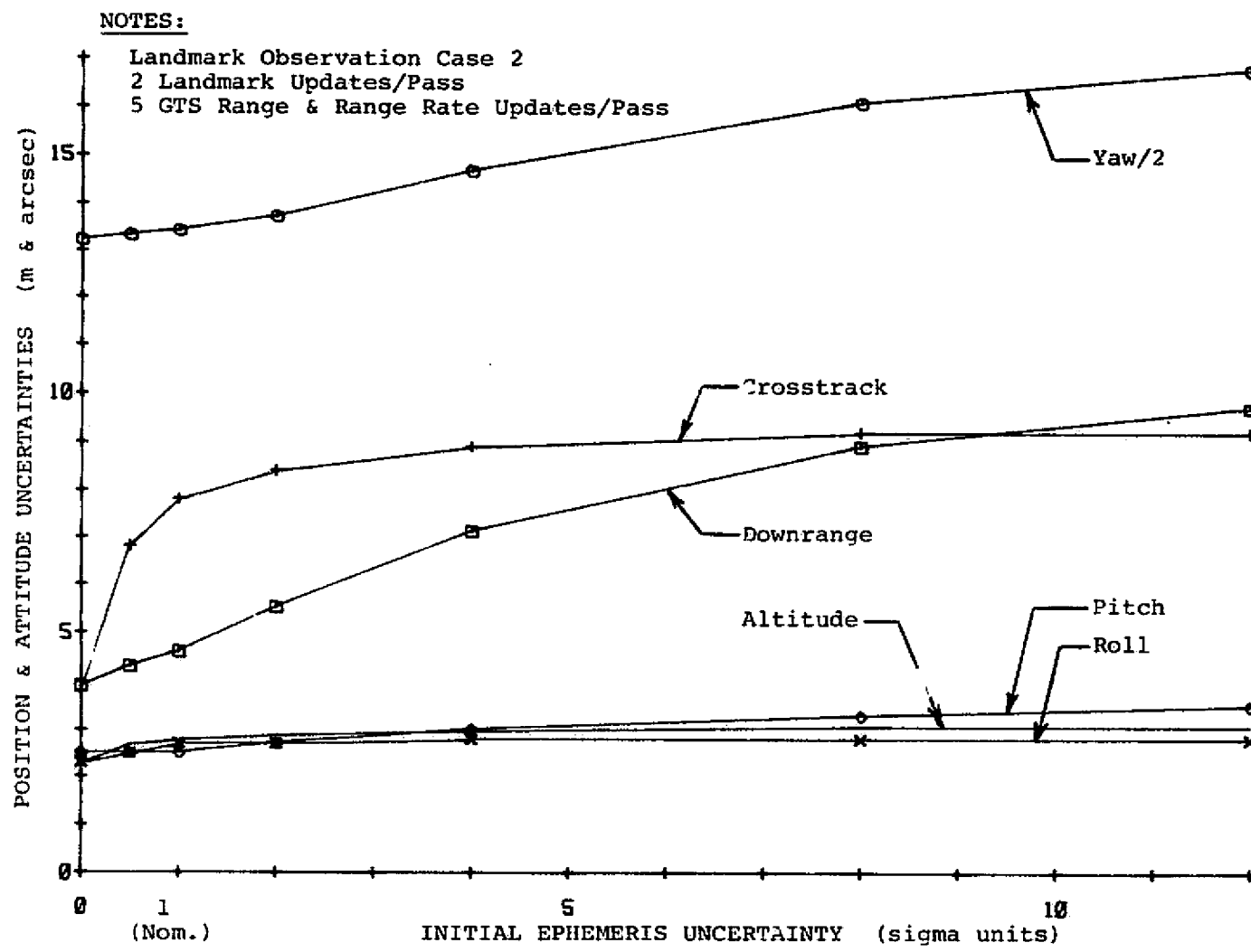


Figure 2-12 Sensitivity to Initial Ephemeris Uncertainty

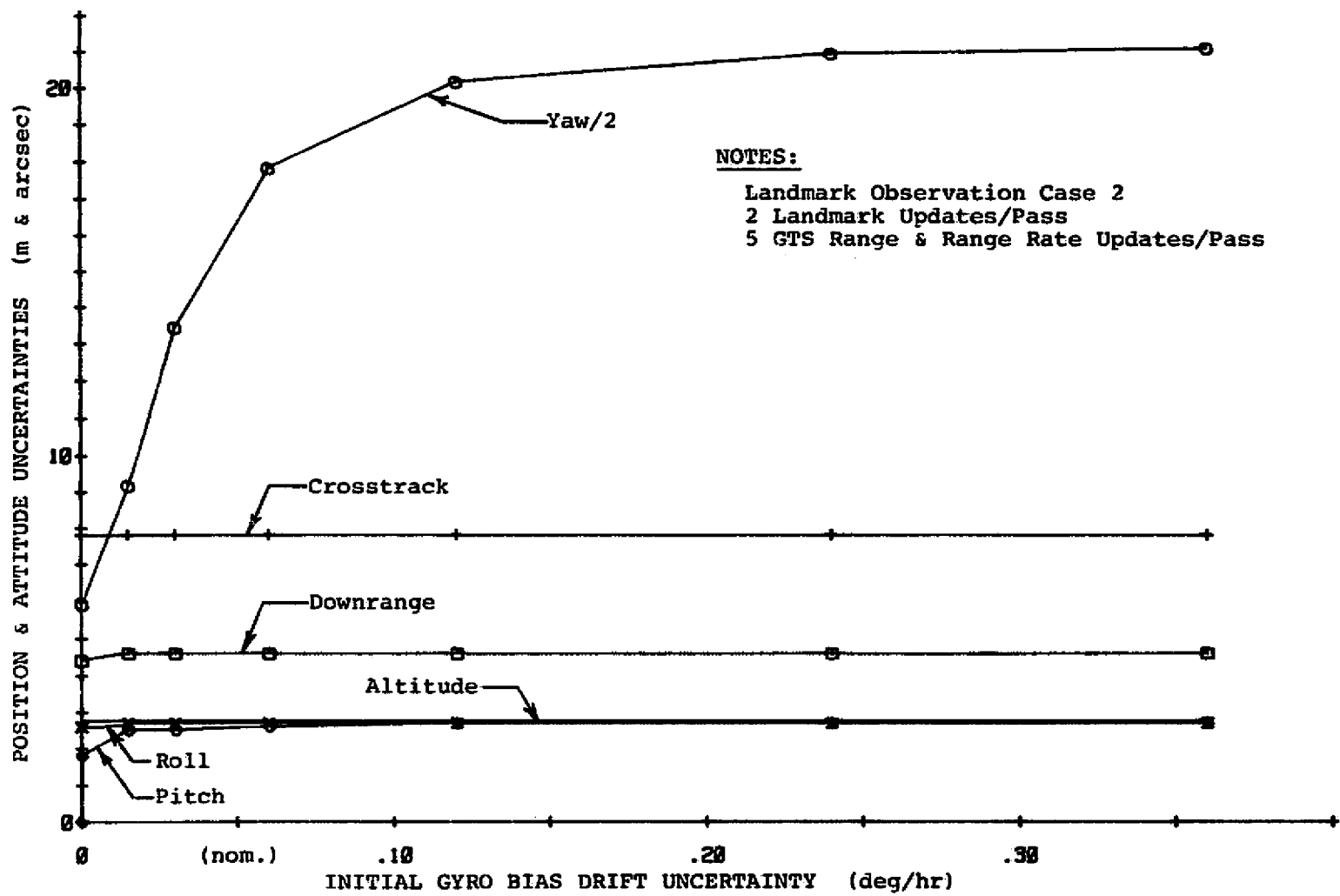


Figure 2-13 Sensitivity to Initial Gyro Bias Drift Uncertainty

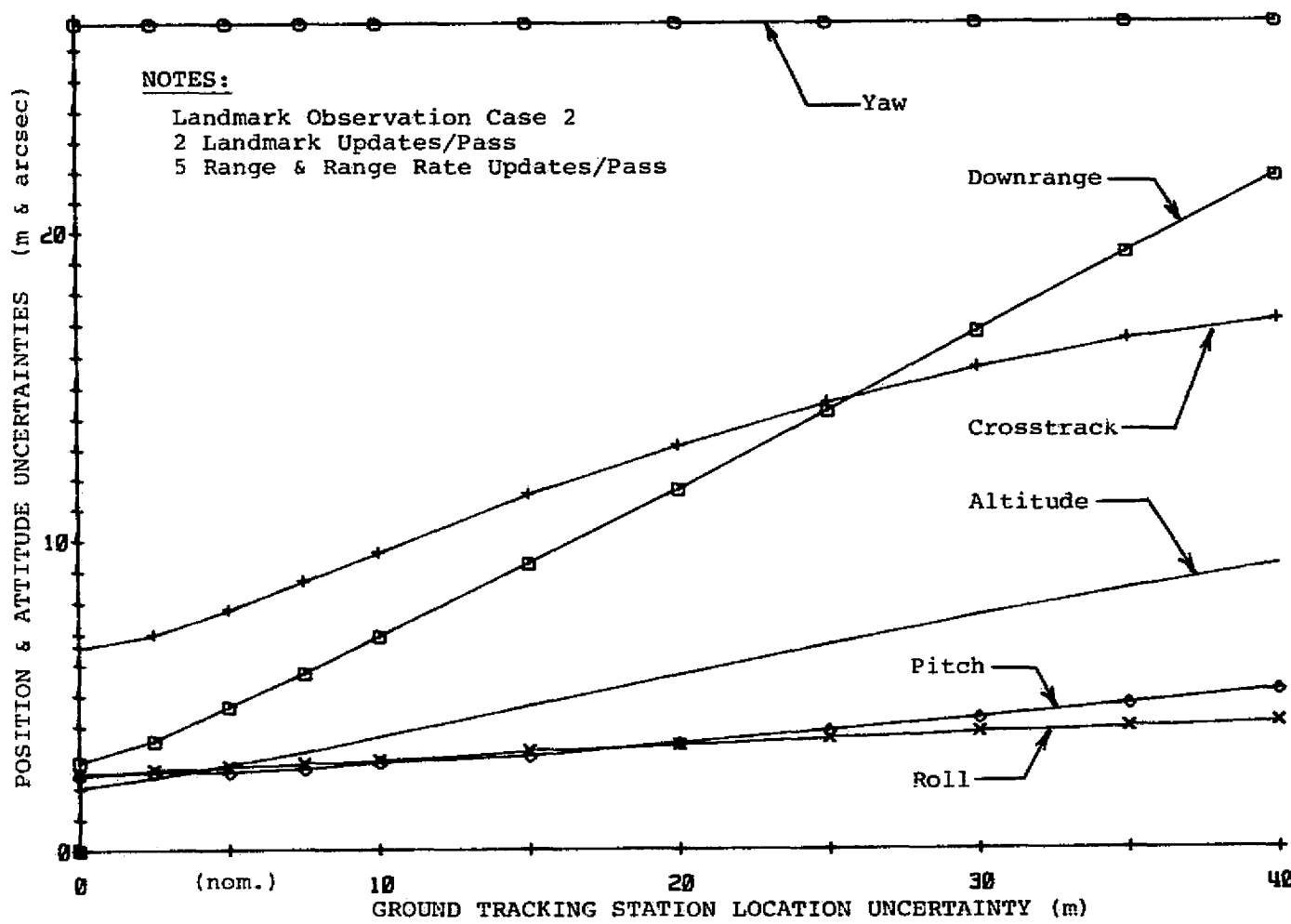


Figure 2-14 Sensitivity to Ground Tracking Station Location Uncertainty

NOTES:

Landmark Observation Case 2  
2 Landmark Updates/Pass  
5 GTS Range & Range Rate Updates/Pass

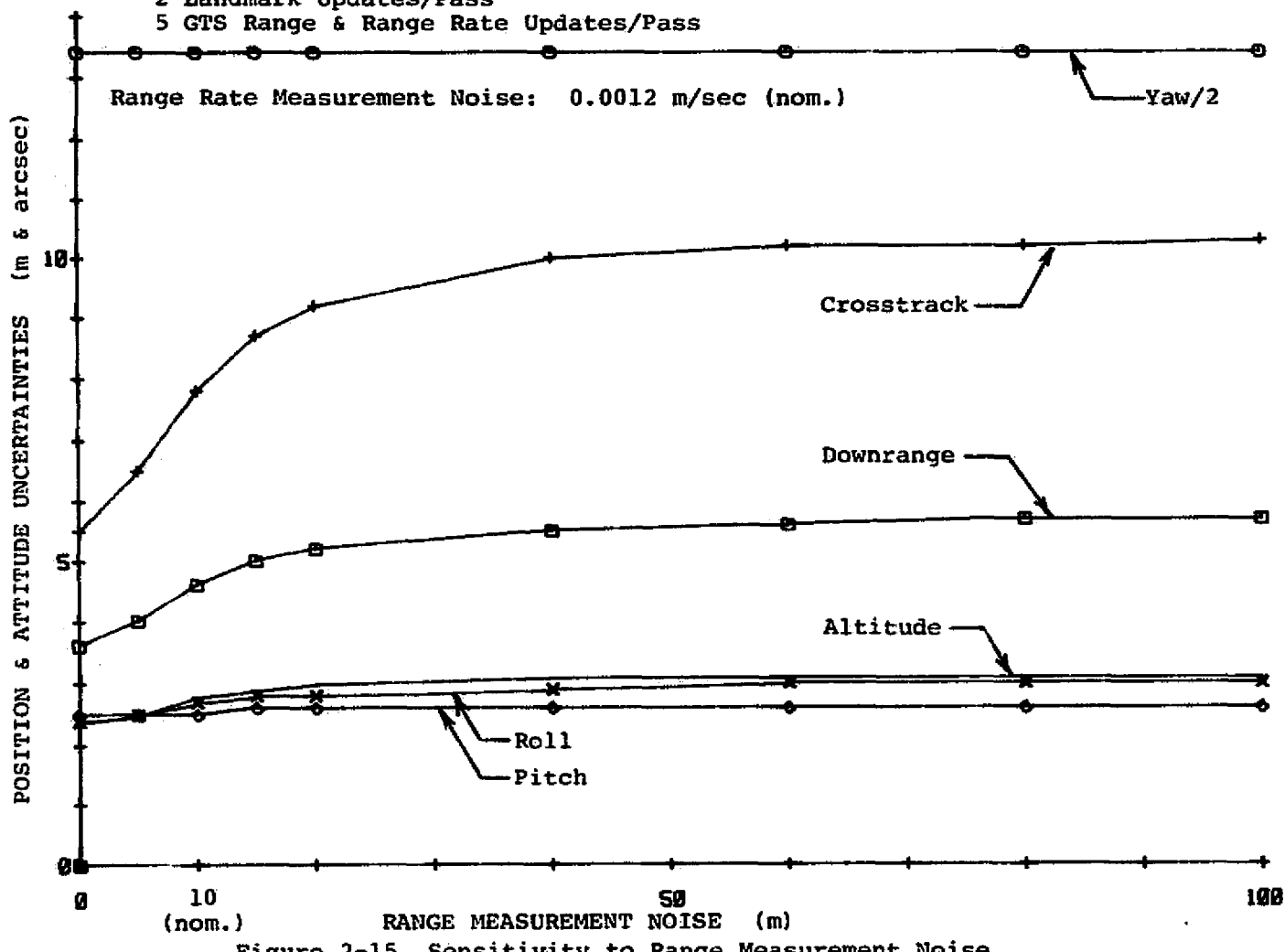


Figure 2-15 Sensitivity to Range Measurement Noise

gained from range measurements when the one-sigma noise in these measurements exceeds about twice the nominal value of 10 meters.

#### Sensitivity to Range Rate Measurement Noise

Figure 2-16 shows the effect of variation in the range rate measurement noise while maintaining all other conditions at nominal. In contrast to the results just shown for range measurement noise in Figure 2-15, it is seen that the sensitivity to range rate noise extends over a much larger range of variation in this parameter. This is also seen to be the case in Table 2-3.

#### Sensitivity to Landmark Position Uncertainty

Figure 2-17 shows the sensitivity of performance to landmark position uncertainty when landmark measurements are used in combination with ground tracking measurements. It is seen that the performance in estimating attitude is strongly affected by a variation in the landmark position uncertainty, while the performance in estimating spacecraft position is essentially unaffected. This is as expected since the landmark measurements provide the only data on attitude, while the ground tracking measurements, with the assumed high accuracies, dominate the performance in estimating spacecraft position. If landmark measurements had been used with star sightings instead of ground tracking measurements, the reverse situation would have occurred, where the star sightings dominate the attitude performance and the landmark measurements provide the only information on spacecraft position. (See Figure 2-18 of Reference 8). In either case, it is important to note from Section 2.7.2 that the landmark position uncertainty is treated in this covariance study as being the overall error associated with a landmark measurement.

#### Sensitivity to Number of Range Updates per Pass

Figure 2-18 shows that approximately 15 range updates per pass are required to reach asymptotic levels in position estimation performance when no range rate measurements are included. Although the conditions under which this data was generated are not considered to be quite nominal since the nominal range rate measurements were not

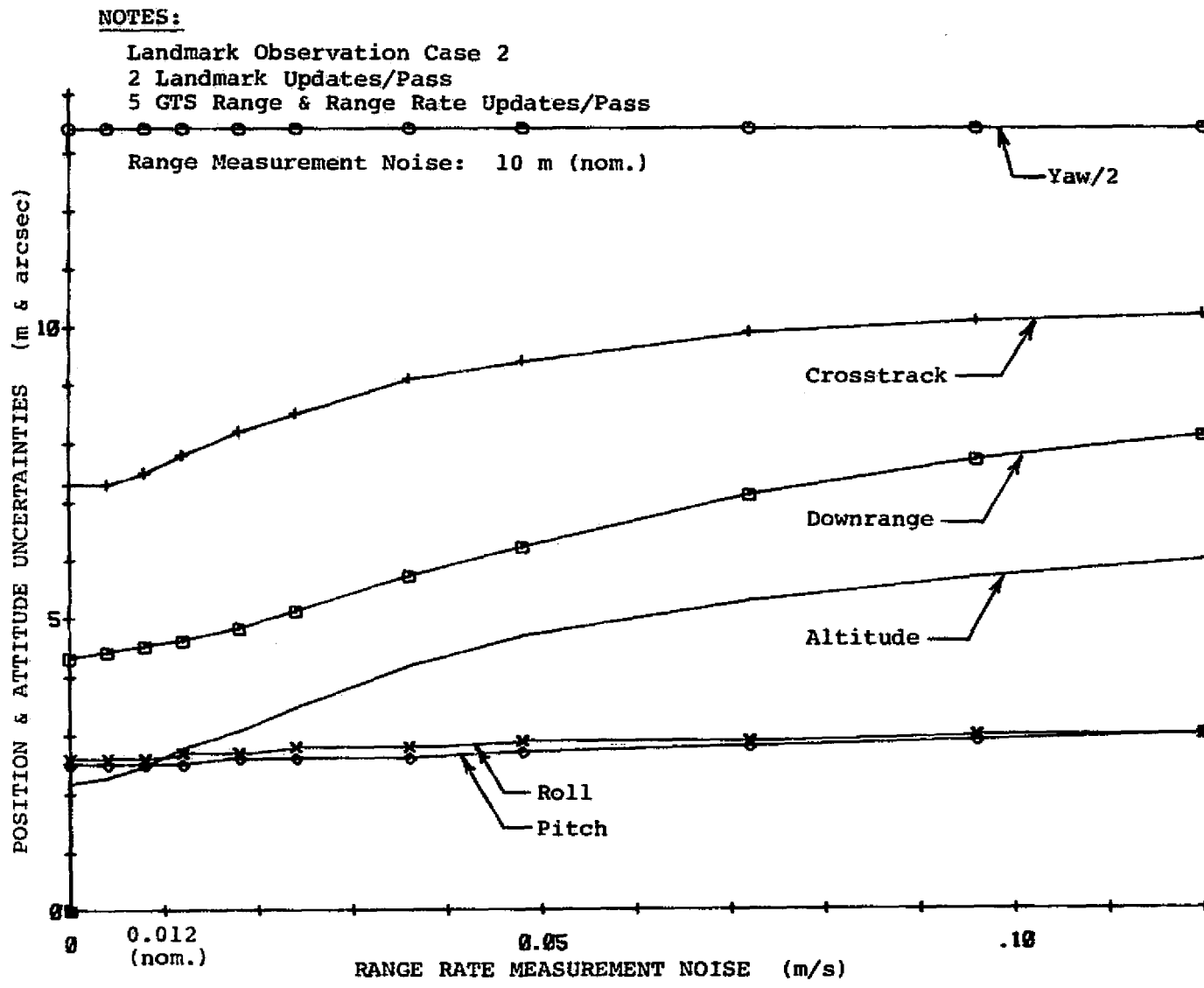


Figure 2-16 Sensitivity to Range Rate Measurement Noise

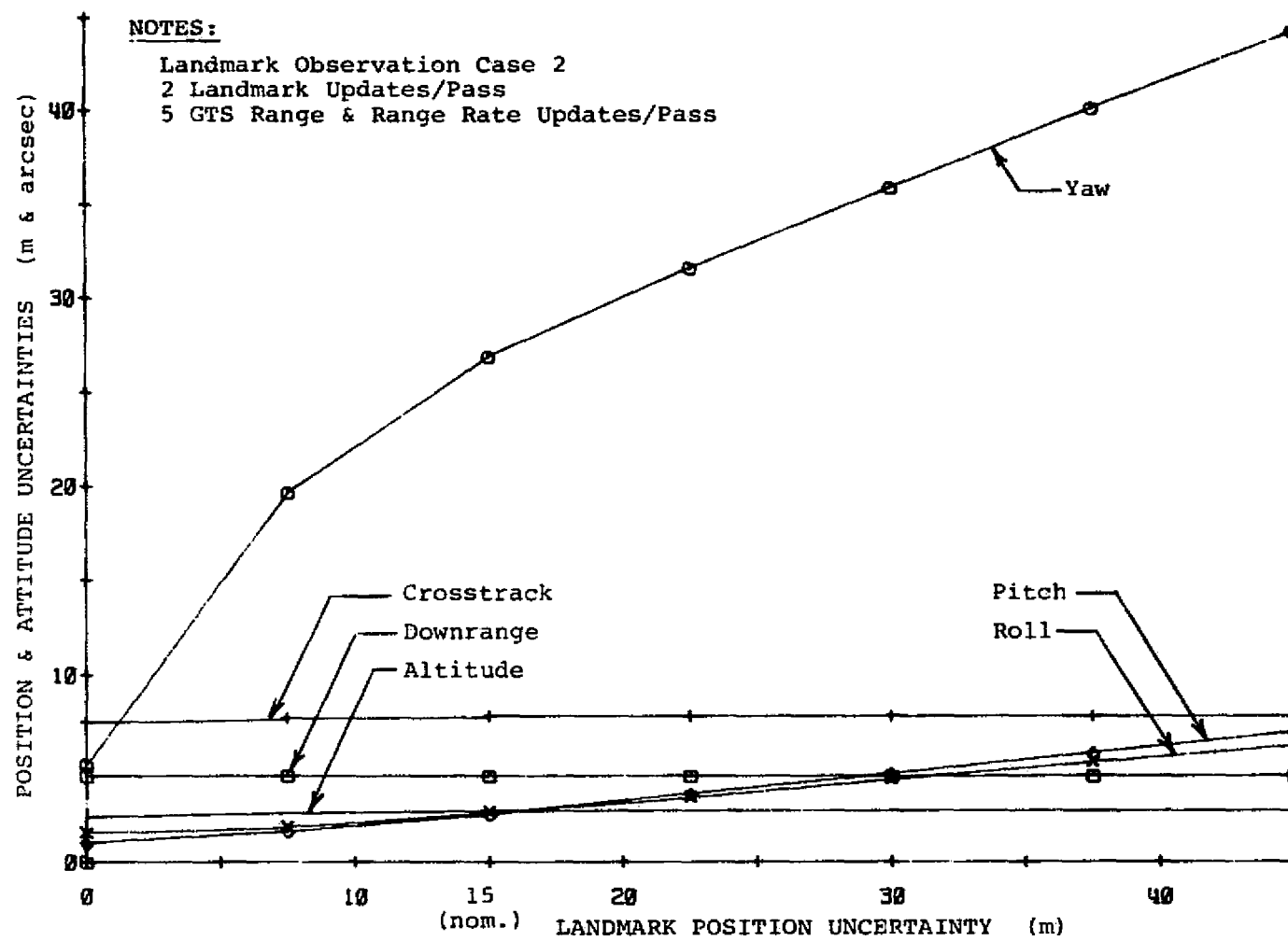


Figure 2-17 Sensitivity to Landmark Position Uncertainty

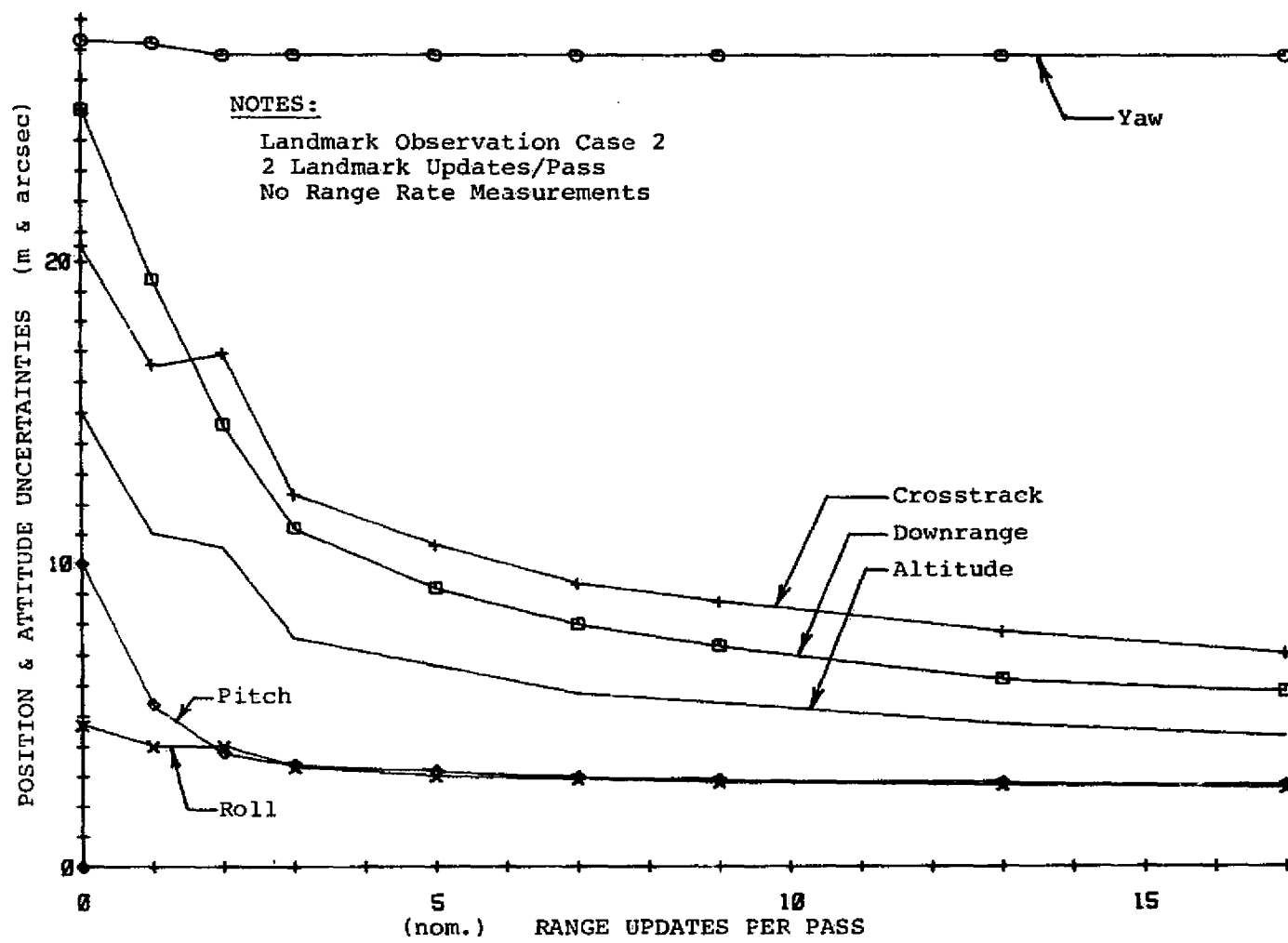


Figure 2-18 Sensitivity to Number of Range Updates per Pass

included, the data at least shows the effect of varying the number of range measurements in combination with the nominal number of landmark measurements. Also note in Figure 2-18 that only two or three range updates are required per pass in order to achieve minimum attitude estimation uncertainties.

#### Sensitivity to Number of Range Rate Updates per Pass

Figure 2-19 indicates that minimum position estimation uncertainties are achieved after about 5 range rate updates per pass when no range measurements are included. Note that it takes fewer range rate updates per pass, as compared to range updates per pass, to achieve minimum estimation uncertainties. Also note that only two or three range rate updates per pass are required to reduce the attitude uncertainties to minimum levels.

#### Sensitivity to Number of Range and Range Rate Updates per Pass

Shown in Figure 2-20 is the sensitivity of performance to the number of updates per pass with both range and range rate measurements. Here it is seen that the affect on performance is not much different from that in Figure 2-19 where no range measurements were made. In addition, it is seen that five range and range rate measurements (the nominal number used in this study) yield results which are fairly close to what would be obtained if more range and range rate measurements were used during a pass.

#### Sensitivity to Number of Landmark Updates per Pass

As was true in Figure 2-17 for sensitivity to landmark position uncertainty, Figure 2-21 shows that the attitude estimation uncertainties are reduced by increasing the number of landmark updates per pass, while the uncertainties in estimating spacecraft position remain unaffected. Note that only two landmark updates per pass are required to bring the attitude uncertainties close to their minimum levels. Again it is important to note that the results in Figure 2-21 (like those in Figure 2-17) were generated for the case of no star sightings. If landmark measurements had been used with star sightings instead of range and range rate measurements, the performance in estimating spacecraft position would have been affected to some extent by the number of landmark updates per pass. (See Figure 2-13 of Reference 8).

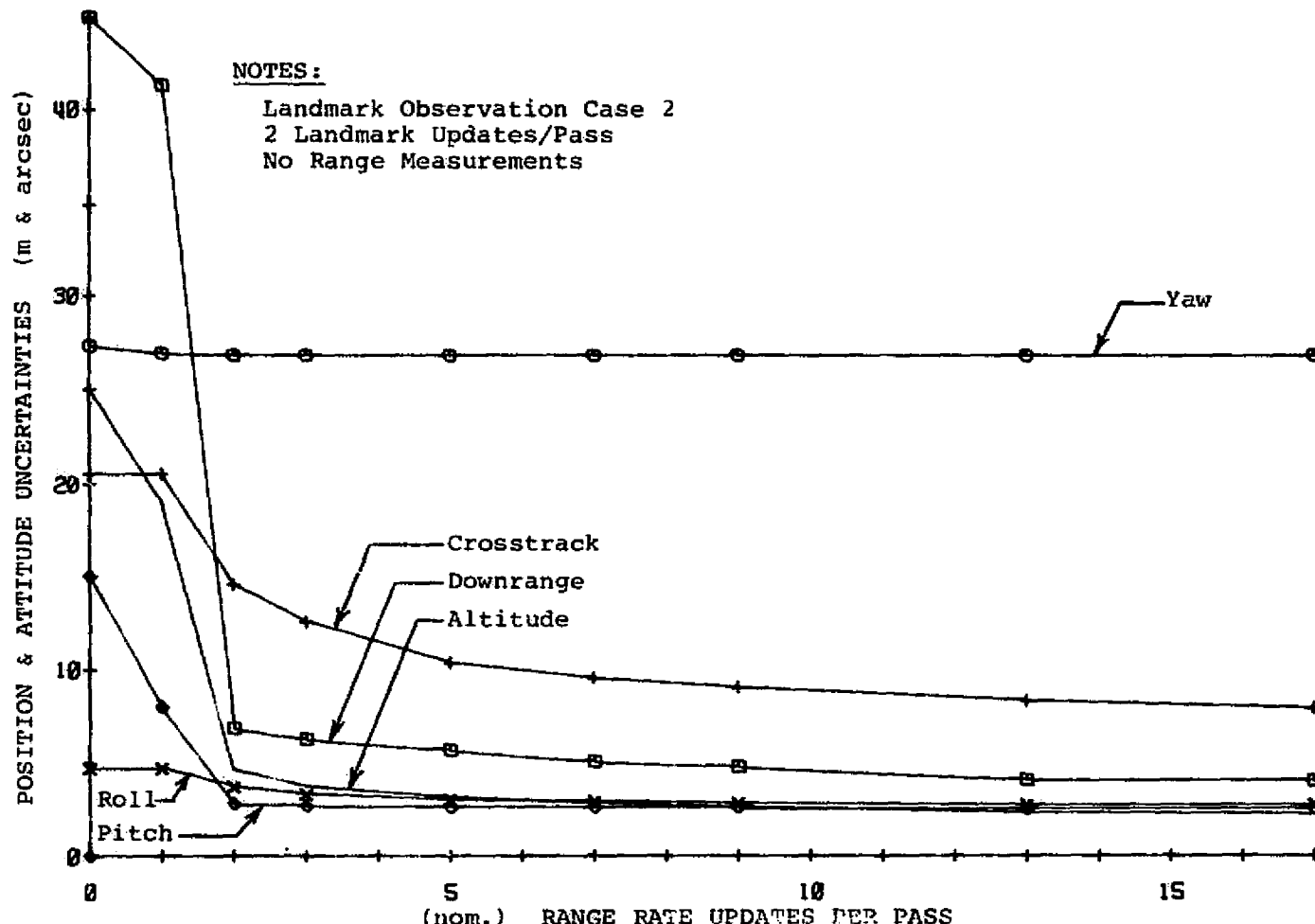


Figure 2-19 Sensitivity to Number of Range Rate Updates per Pass

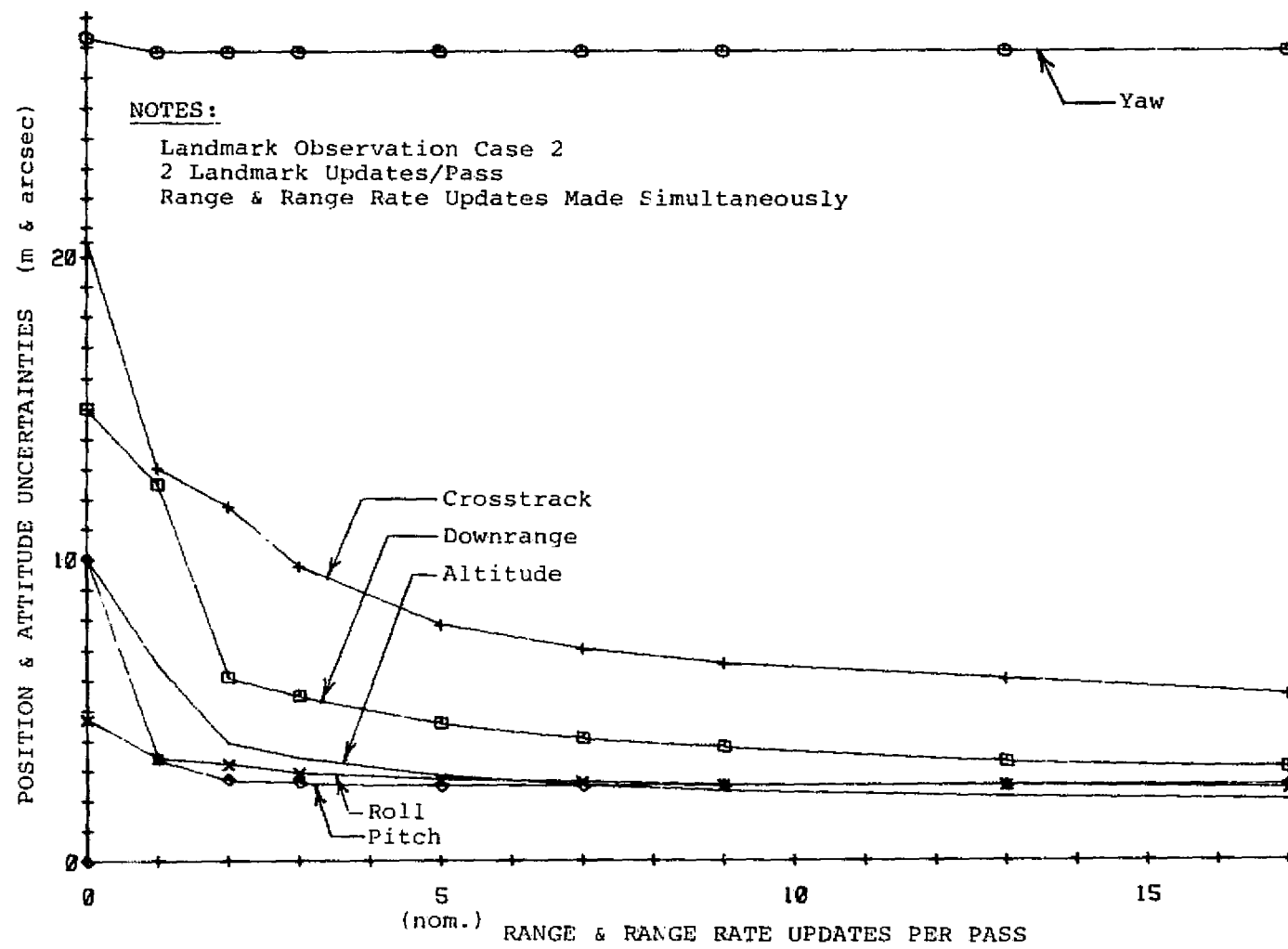


Figure 2-20 Sensitivity to Number of Range &amp; Range Updates per Pass

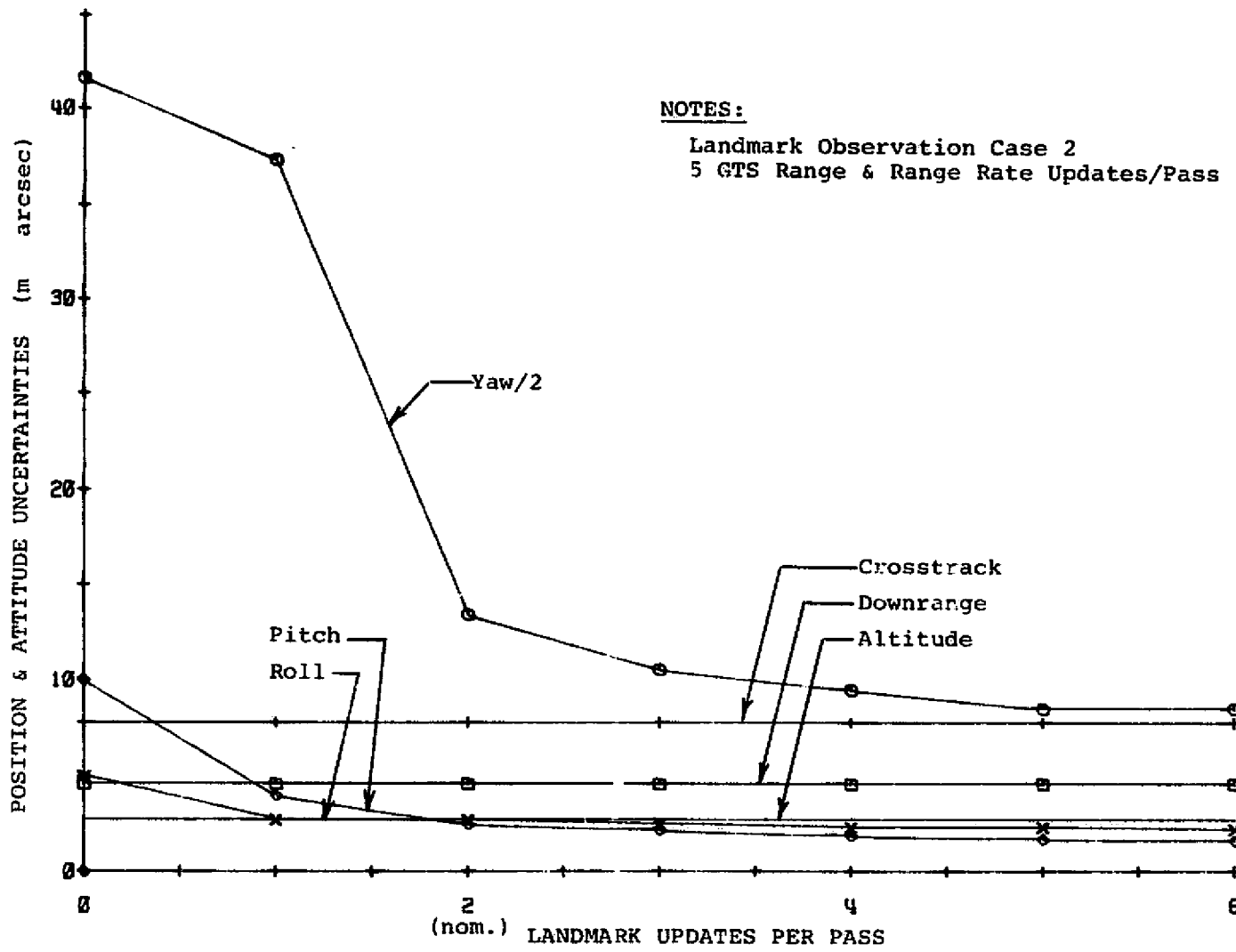


Figure 2-21 Sensitivity to Number of Landmark Updates per Pass

### Sensitivity to Gyro Random Drift and Quantization

Performance results were generated with various values of gyro random drift up to six times the nominal value of 0.01 degree per hour. For this amount of variation the results showed that random drift had no affect on the position estimation performance and only a slight influence on attitude estimation performance. For example, a six sigma random drift on each gyro resulted in pitch, roll and yaw uncertainties of 2.6, 3.1, and 27.1 arcsecs, respectively, while nominal values of random drift resulted in 2.5, 2.7, and 26.8 arcsecs.

Studies of sensitivity to gyro quantization noise also produced similar results. The attitude uncertainties for a six sigma quantization noise on each gyro were almost the same as those for a six sigma random drift on each gyro.

### Sensitivity to Gravity Harmonic Uncertainties

In Section 2.1 the gravity harmonic uncertainties were defined as being equal to a constant times the difference between the corresponding C and S coefficients of the two most recent Smithsonian gravitational models (SEII and SEIII). This constant (0.33) was chosen so that the resulting ephemeris error data would match the results obtained from GSFC for five orbits. Inspection of equivalent data from other studies indicate that the above definition is probably pessimistic. In Table 2-7 some performance results are shown for various values of the gravity harmonic uncertainties relative to the nominal values defined above. This table clearly shows that the indicated changes in the harmonic uncertainties have negligible affect on the attitude estimation uncertainties, while the affect on the position estimation uncertainties is moderate.

TABLE 2-7

## SENSITIVITY TO GRAVITATIONAL HARMONIC UNCERTAINTIES

Gravitational Harmonic Uncertainties	State Estimation Uncertainties ( $\text{lo}$ )					
	Attitude (arcsec)			Position (meters)		
	Pitch	Roll	Yaw	Alt.	Range	Track
<u>Initial State Uncertainties Are:</u>						
	60	60	60	20	50	20
0	2.5	2.6	26.8	2.3	4.5	6.6
0.5 $\sigma$	2.5	2.6	26.8	2.5	4.5	6.9
1 $\sigma$	2.5	2.7	26.8	2.8	4.6	7.8
2 $\sigma$	2.6	2.8	26.8	3.6	4.9	10.0
4 $\sigma$	2.6	3.1	26.8	4.9	5.5	13.4
6 $\sigma$	2.7	3.3	26.9	5.9	6.1	15.4

Notes: Landmark Observation Case 2

2 Landmark Updates per Pass

5 Range and Range-Rate Updates per Pass (Ground Tracking)

## 2.9 CONCLUSIONS

In contrast to the previous study<sup>(1)</sup> where star and landmark measurements were used to estimate spacecraft attitude, orbital ephemeris, and gyro bias drift, the present study is primarily concerned with how well the same state parameters can be estimated when using landmark measurements in combination range and/or range rate measurements with respect to ground tracking stations or the proposed Tracking and Data Relay Satellite System (TDRSS). For purposes of comparison, some results of the previous study are included with the results of the present effort in Section 2.8. In the previous study it was found that landmark measurements alone (See Table 2-2) were not sufficient to estimate all twelve state parameters. (At least, this was the case for landmarks visible to the multispectral scanner of Landsat or the proposed EOS). However, by using both star and landmark measurements, it was found that very good performance could be obtained in estimating all twelve state parameters (See Table 2-3). In this case, the star sightings were the primary source of data for estimating spacecraft attitude and gyro bias drift, and the landmark measurements provided the only information on orbital ephemeris. However, when landmark measurements are used only with range and/or range rate measurements (See Table 2-3), the landmark measurements play a reverse role in that they provide the only data for estimating spacecraft attitude and gyro bias drift, while the range and/or range rate measurements dictate the performance in estimating orbital ephemeris. In comparing the attitude performance for these two cases in Table 2-3, it is seen that the performance is noticeably better when using star sightings. However, the following differences, which favor the star tracker, should be noted:

- 1) More star measurements (20 per orbit) were made than landmark measurements (2 per pass).
- 2) The star measurements were uniformly distributed throughout each orbit, while the landmark measurements were restricted to that part of the orbit over the USA.

- 3) Some of the stars were further from the local vertical than any of the landmarks due to the larger field-of-view of the star tracker ( $8^\circ$  square). Consequently, the performance in estimating yaw attitude should be better for the star measurements.
- 4) The assumed accuracy of the star measurements (5 arcsecs per axis) is somewhat optimistic for the star tracker being considered for this type of mission, while the accuracy assumed for the landmark measurements may conceivably be more realistic.

However, regardless of the relative merits of star and landmark measurements in estimating spacecraft attitude, it is seen from the general results of this study that landmark measurements are very versatile in that they can be used as the primary or backup data source for attitude or orbit determination.

In this study, performance results were generated for landmark measurements in combination with range and range rate measurements from either TDRSS or ground tracking stations. (See Table 2-4). In the case of TDRSS it was found that the performance was not as good as with ground tracking stations primarily because of the larger uncertainties adopted for the ephemeris of TDRSS. If these uncertainties were reduced by two orders of magnitude, the resulting performance in estimating spacecraft attitude and orbital ephemeris would probably be comparable with that obtained with ground tracking.

From the sensitivity studies made with landmark measurements, combined with range and range rate measurements with respect to ground tracking stations, the following conclusions can be made:

- 1) Only two observation passes over the USA are required for reasonable performance in estimating both attitude and orbital ephemeris.

- 2) It is not necessary to use both range and range rate measurements with landmark measurements in order to obtain good estimation performance. For example, range rate measurements combined with landmark measurements do almost as well as when range measurements are included. (See Table 2-3).
- 3) Only two landmarks are required on each pass over the USA in order to achieve almost steady state performance in estimating spacecraft attitude. (See Figure 2-21).
- 4) Variation of the landmark position uncertainty and the number of landmark updates per pass had no affect on orbital ephemeris estimation. Only the attitude performance is affected by these parameters. (See Figures 2-17 and 2-21).
- 5) About two updates per pass are required in range or range rate in order to achieve near-steady state performance in estimating pitch and roll. (See Figures 2-18, 2-19, and 2-20).
- 6) The performance in yaw is essentially independent of range or range rate measurements.

## SECTION 3

### STAR AND LANDMARK MEASUREMENT EQUATION DEVELOPMENT

#### 3.1 INTRODUCTION

In this section the results are presented for the study task pertaining to the development of detailed measurement equations for the basic onboard navigation measurements. Since the navigation system for EOS may rely extensively on computations done at a ground processing center, it may be possible to treat the larger state vectors associated with a more detailed set of measurement models.

Two types of measurements are considered; namely a star direction measurement using a star camera device, and a landmark direction measurement using a multispectral scanner. The scanner is assumed to be one that scans from side to side at a constant rate.

The previous treatments of the measurements for these two sensors<sup>(1)</sup> assumed that the basic measurements were angles and that the associated errors were white noise. In fact the basic measurements are voltages and time intervals. These are converted to angles by means of computations which introduce errors beyond those arising in the measurement of the basic quantities.

If the basic measurements are taken to be angles, as was done previously, the errors arising from conversion of basic measurements to angles must be accurately represented. However it is simpler and more direct to enter the basic measured quantities into the navigation estimation equations. This approach may only be tractable when ground based computations are considered since use of the raw measurements along with more detailed error models implies increased computational requirements.

## 3.2 STAR TRACKER MEASUREMENT EQUATION

### 3.2.1 Introduction

Several potential navigation system configurations for EOS involve star tracking devices. A leading candidate for this application is a star "camera" device such as the Ball Brothers CT401 star tracker. This type of tracker has the attribute that it acquires and tracks stars by means of a scanning electron beam, and therefore requires no moving mechanical parts. It is a body-mounted device whose optical axis is often aligned with the spacecraft negative  $z_B$ -axis (local zenith).

The task addressed here is to derive a measurement model specifically for a tracker of this type. The goal of the derivation is a model that is very general i.e., includes all the major noise types and sources. Essential steps in the derivation include formal statements of the tracker fundamental measurement and the state-vector, measurement-vector relationship, derivation of the formal partial derivative equations, and definition of the form of the output-measurement relationship.

### 3.2.2 Basic Tracker Operation and Measurement

The tracker has a square field of view several degrees on a side, and the center of the field is pointed at some selected direction in spacecraft body coordinates. There are two modes of operation, namely the search and track modes. In the search mode the scanning electron beam is driven over a uniform scan pattern by ramp and stepped voltages in the directions of the major axes of the field of view. When a star signal, represented by a beam current increase, is detected at a selected threshold value, the associated search voltages are observed,

and their values are used to define the star direction. When a star has been "found", it is then tracked (in the track mode) by a restricted field scan operation, and changes in star position due to spacecraft motion are added to the basic location voltages that were obtained at acquisition. Thus the basic star tracker measurements are a pair of voltages along nominally orthogonal axes. The relationship between these voltages and the angles defining the star location in the field of view is not, however, a simple proportion because of various distortions of the scan geometry. Instead, a functional relationship between the basic analog voltages and the star position angles is derived by means of calibration against a test star pattern. Discussion of this functional relationship is deferred until later. Detailed description of the tracker operation can be found in Reference 13.

### 3.2.3 Formal Measurement Equation

The relationship between the measurements, state, and noise levels in the device is intrinsically nonlinear. It can be written as

$$\underline{z} = \underline{z}(\underline{x}, \underline{x}_c, \underline{v}) \quad (3-1)$$

where  $\underline{z}$  is a vector whose elements are the measured quantities,  $\underline{x}$  is the spacecraft and tracker state vector,  $\underline{x}_c$  is a vector of unestimated variables<sup>(14,15)</sup> that affect the state covariance ("consider" parameters), and  $\underline{v}$  is a vector of white noises. The state  $\underline{x}$  for this problem consists mainly of quantities defining the spacecraft attitude such as attitude angles and gyro bias drift, and estimatable biases in the star tracker.

Assuming that the estimation process to be applied for navigation will be linear, we expand Equation 3-1 in a Taylor series keeping only first order terms. The formal linearized measurement equation is thus

$$\delta \underline{z} = \frac{\partial \underline{z}}{\partial \underline{x}} \delta \underline{x} + \frac{\partial \underline{z}}{\partial \underline{x}_c} \delta \underline{x}_c + \frac{\partial \underline{z}}{\partial \underline{v}} \delta \underline{v} . \quad (3-2)$$

In the case of covariance propagation studies, as for example in Section 2 of this report, the  $\delta$ 's represent statistical deviations of variables from nominal values. In an actual estimation application the  $\delta$ 's represent deviations of the true state from the estimated state. The partial derivative convention used here is the following:

$$\frac{\partial z_i}{\partial x_j} = h_{ij} ,$$

so that differentiation of column vector  $\underline{z}$  by column vector  $\underline{x}$  yields a matrix  $H$  (with elements  $h_{ij}$ ). The matrices  $H$ ,  $H_c = \frac{\partial \underline{z}}{\partial \underline{x}_c}$ ,  $A = \frac{\partial \underline{z}}{\partial \underline{v}}$  are here termed measurement "sensitivity" matrices. Thus equation 3-2 may be written

$$\delta \underline{z} = H \delta \underline{x} + H_c \delta \underline{x}_c + A \delta \underline{v} .$$

In the case of the CT401 star tracker the measurement vector ( $\underline{z}$ ) is taken to be the scan voltages mentioned previously, namely

$$\underline{z} = \begin{pmatrix} v_x \\ v_y \end{pmatrix} . \quad (3-3)$$

As implied by  $\underline{z}$ , the nominal boresight axis of the tracker is taken to be the  $z$  axis.

There are many potential sources of contributions to the measurement error ( $\delta \underline{z}$  in Equation 3-2). First, there are possible state uncertainties consisting of spacecraft attitude and several tracker bias errors that might be estimated. Secondly there are unestimated biases or "consider" biases,<sup>(16,17)</sup> and thirdly, there are white noise sources. The major error sources in the star tracker measurement are listed below in Table 3-1 along with representative one sigma values.

TABLE 3-1  
MAJOR ERROR SOURCES, TYPES AND REPRESENTATIVE VALUES\*

Estimatable Biases

Alignment	-	5 arcsec
Geometric Calibration	-	20 arcsec
Mechanical Distortion	-	5 arcsec
Temperature Measurement Bias	-	2.5 arcsec/deg
Magnetic Field Measurement	-	50 arcsec/gauss

Consider Biases

Temperature Fluctuations	-	2.5 arcsec/deg
Magnetic Field Fluctuations	-	50 arcsec/gauss
Star Intensity Estimates	-	9 arcsec/mag

White Noise

Poisson Photon Arrival Rate	-	5 arcsec
Electronic Noise	-	15 arcsec

Two bias sources, namely temperature and magnetic field variations, can be included in either bias category, depending upon the

---

\* The representative error values are based in part upon Reference 13, and in part upon conversations with R.L. Cleavenger of Ball Brothers Research Corporation and R. Doxie of MIT's Center for Space Research. These errors are very design specific and therefore cannot be loosely used for any application. Errors in each of the listed categories can be reduced considerably by sufficient application of engineering design effort.

details of the tracker data reduction. For example, if temperature and axial magnetic field strength are not measured, then deviations of these quantities from their calibration values will fluctuate with random amplitude on a time scale that is long compared to the measurement time. These fluctuations would then be treated as consider biases.

### 3.2.4 Tracker-Inertial Coordinate Relationship

To evaluate the partial derivatives or sensitivity matrices  $H$ ,  $H_C$ ,  $A$  of Equation 3-2 we write a vector equation relating the tracker line-of-sight (LOS) to a star, to the inertial direction of the star. The error-free relationship is just

$$\underline{S}_B = T_{BO}T_{OI}\underline{S}_I \quad (3-4)$$

where  $T_{BO}$  and  $T_{OI}$  are the coordinate rotations from inertial to spacecraft body coordinates, as defined in Section 2.  $\underline{S}_I$  is a unit vector in inertial coordinates defining the LOS to the star being tracked.  $\underline{S}_B$  is the corresponding unit LOS vector to the star in body coordinates. To simplify the treatment of tracker errors we define another rotational transformation  $T_{BT}$  which transforms from tracker boresight coordinates to body coordinates. In the tracker boresight system the star is located in direction  $\underline{S}_T$ , and Equation 3-4 is just

$$T_{BO}T_{OI}\underline{S}_I = T_{BT}\underline{S}_T . \quad (3-5)$$

The rotational transform  $T_{BT}$  is arbitrary and composed of a pair of rotations  $T_A T_B$  for boresight pointing, and a rotation  $T_C$  for field of view orientation. We select the convention of having the star tracker z axis lie along the boresight direction. Thus a star lying along the boresight has the following direction in tracker coordinates:

$$\underline{S}_T = \begin{pmatrix} -\theta \\ 0 \\ i \end{pmatrix} .$$

This geometry is shown in Figure 3-1. The general form for  $\underline{S}_T$  is obtained by a pair of rotations from tracker coordinates to the star direction in tracker coordinates. A rotation about  $y_T$  through an angle  $\alpha$  followed by a rotation about  $x_T$  through an angle  $\beta$  yields a pair of angles in orthogonal planes corresponding to the two electron beam angles. These are related to scan voltages in the tracker. The unit vector  $\underline{S}_T$  is thus

$$\underline{S}_T = \begin{pmatrix} \sin \alpha \\ -\cos \alpha \sin \beta \\ \cos \alpha \cos \beta \end{pmatrix} . \quad (3-6)$$

Errors in the star position measurement are reflected in the term on the right in Equation 3-5.

### 3.2.5 Measurement Error Relationships

Errors in alignment of the tracker with the spacecraft axes can be expressed as a small angle rotation matrix  $T_\epsilon$  multiplying  $T_{BT}$ . True values of  $\alpha$  and  $\beta$  can be represented as the sum of values predicted from the voltage-angle calibration relationship, and error values. Thus

$$\alpha = \alpha_p + \alpha_e ,$$

$$\beta = \beta_p + \beta_e .$$

Equation 3-5 can therefore be expressed in terms of the errors as

$$T_{BO} T_{OI-I} \underline{S}_T = T_\epsilon T_{BT} \underline{S}_T (\alpha_e, \beta_e) \quad (3-7)$$

with

$$\underline{S}_T = \begin{pmatrix} \sin (\alpha_p + \alpha_e) \\ -\cos (\alpha_p + \alpha_e) \sin (\beta_p + \beta_e) \\ \cos (\alpha_p + \alpha_e) \cos (\beta_p + \beta_e) \end{pmatrix} \quad (3-8)$$

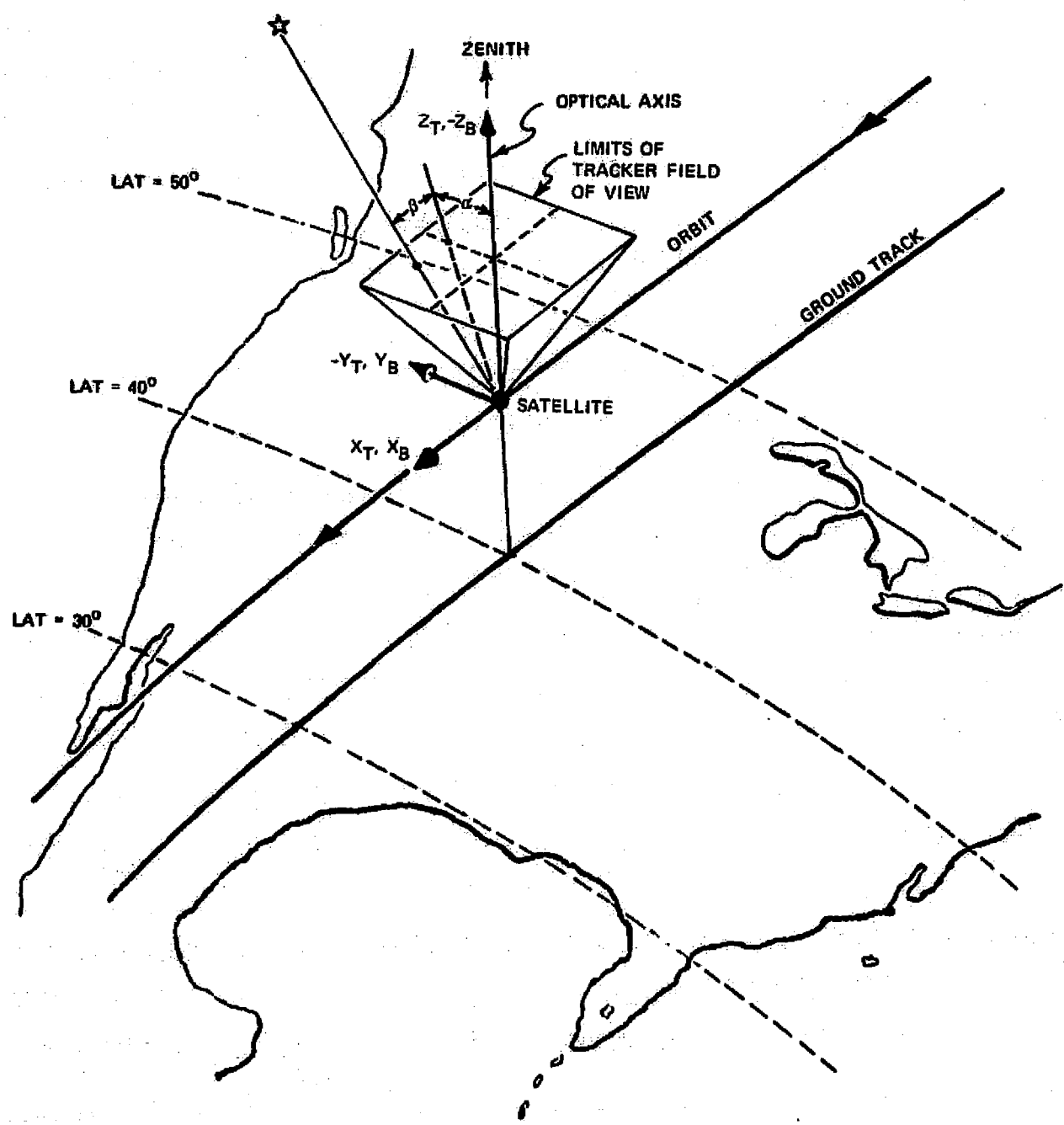


Figure 3-1 Star Tracker Measurement Geometry

If we let  $\alpha(z)$  and  $\beta(z)$  represent the electron beam angle functions of the voltage, then the form of  $\alpha_p(z)$  and  $\beta_p(z)$  depends upon how one calibrates the tracker distortions. The most straightforward calibration is done by fitting a least squares polynomial to simulated star test field measurements (Ref.13). The test field contains a  $9 \times 9$  rectangular array of simulated stars, thus the polynomial should not be of high order. In Reference 13 first and second order terms are used. Following that example we write

$$\begin{aligned}\alpha_p &= A_1(T-T_0, B, I-I_0) + A_2(T-T_0, B, I-I_0)V_x + A_3(T-T_0, B, I-I_0)V_y \\ &\quad + A_4(T-T_0, B, I-I_0)V_x^2 + A_5(T-T_0, B, I-I_0)V_y^2 + A_6(T-T_0, B, I-I_0)V_x V_y . \\ \beta_p &= B_1(T-T_0, B, I-I_0) + \dots \text{ (similar form).} \end{aligned}\quad (3-9)$$

The coefficients  $A_i$  and  $B_i$  are functions of deviations of temperature ( $T$ ), magnetic field strength ( $B$ ), and star magnitude ( $I$ ) from their values at calibration. The cross terms, i.e. those terms involving  $V_y$  in  $\alpha$  and  $V_x$  in  $\beta$ , occur because the nominally orthogonal planes in which  $\alpha$  and  $\beta$  are measured may be slightly nonorthogonal, and because certain phenomena such as a strong axial component of the Earth's magnetic field cause an effective rotation of the sensor axes.

If one considers the errors in  $\alpha$  and  $\beta$  to be small compared to their magnitudes, it is then possible to write

$$\begin{aligned}\alpha_p + \alpha_e &= (A_1 + \delta A_1) + (A_2 + \delta A_2)V_x + \dots , \\ \beta_p + \beta_e &= (B_1 + \delta B_1) + (B_2 + \delta B_2)V_x + \dots .\end{aligned}\quad (3-10)$$

or

$$\begin{aligned}\alpha_e &= \delta A_1 + \delta A_2 V_x + \delta A_3 V_y + \dots , \\ \beta_e &= \delta B_1 + \delta B_2 V_x + \delta B_3 V_y + \dots .\end{aligned}\quad (3-11)$$

Carrying the small error approximation one step further allows each of the coefficient errors to be written as an expansion, namely

$$\delta A_i \approx \frac{\partial A_i}{\partial T} \left|_{T=T_0} \right. + \frac{\partial A_i}{\partial B} \left|_{B=B_0} \right. + \frac{\partial A_i}{\partial I} \left|_{I=I_0} \right. + \dots \quad (3-12)$$

Here  $T_0$  and  $I_0$  are the tracker temperature and star intensity at calibration, and  $B_0$  is the axial magnetic field strength (nominally zero at calibration). If one adds a first order error in the voltage measurement, terms of the form  $A_i \delta V_j$  are added to the above expression for those coefficients that are nominally multiplied by voltages, i.e.  $A_i$ ,  $i > 1$ . An expansion similar to that in Equation 3-12 may also be constructed for  $\delta B_i$ . It should perhaps be emphasized that the coefficient errors in Equation 3-12 represent residual errors after calibration and fitting of the measurements with selected functions. Both the nominal coefficients ( $A_i$ ,  $B_i$ ) and the residual errors in the coefficients ( $\delta A_i$ ,  $\delta B_i$ ) are functions of the temperature, magnetic field and star intensity deviations from the nominal calibration values.

### 3.2.6 Evaluation of Sensitivity Partial Derivatives

To obtain the desired partial derivatives it is necessary to differentiate the general geometric relationship (Equation 3-7). This equation is an expression of the relationship between the measurement vector  $\underline{z}$  and the state  $\underline{x}$ . We restate the equation as

$$T_{BO} T_{OI} S_I = T_e T_{BT} S_T(\alpha, \beta) \quad . \quad (3-13)$$

The quantities on the left are each functions of the state vector  $\underline{x}$ . Thus  $T_{BO}$  is a function of the attitude, and  $T_{OI}$  and  $S_I$  are functions of the ephemeris. For manipulative purposes we may therefore express the left side of Equation 3-13 as a simple function of the state

$$f(\underline{x}) = T_{BO}(\underline{x}) T_{OI} S_I \quad . \quad (3-14)$$

The measurement vector  $\underline{z}$  is contained in  $S_T(\alpha, \beta)$  of Equation 3-13, thus

$$S_T = S_T[\alpha(z), \beta(z)] \quad .$$

If one now allows for estimatable bias errors in temperature, star intensity, tracker alignment, etc., the quantities on the right hand side of Equation 3-13 become functions of the expanded state vector, and one may write a general form for Equation 3-13 in terms of the state vector and measurement vector as

$$\underline{f}(\underline{x}) = T(\underline{x}) \underline{S}_T [\alpha(\underline{x}, \underline{z}), \beta(\underline{x}, \underline{z})] . \quad (3-15)$$

The sensitivity partial  $H = \partial z / \partial \underline{x}$  can now be obtained in general form by implicit differentiation of Equation 3-15. Thus one obtains

$$\frac{\partial \underline{f}}{\partial \underline{x}} = \frac{\partial T}{\partial \underline{x}} \underline{S}_T + T \frac{\partial \underline{S}_T}{\partial \underline{x}} , \quad (3-16)$$

which is further expanded to yield a solution for  $\partial z / \partial \underline{x}$ . Expanding the derivative in the second term on the right of Equation 3-16 gives

$$\frac{\partial \underline{S}_T}{\partial \underline{x}} = \left( \frac{\partial \underline{S}_T}{\partial \alpha} \frac{\partial \alpha}{\partial \underline{x}} + \frac{\partial \underline{S}_T}{\partial \beta} \frac{\partial \beta}{\partial \underline{x}} \right) + \left( \frac{\partial \underline{S}_T}{\partial \alpha} \frac{\partial \alpha}{\partial z} + \frac{\partial \underline{S}_T}{\partial \beta} \frac{\partial \beta}{\partial z} \right) \frac{\partial z}{\partial \underline{x}} . \quad (3-17)$$

Letting the terms in parentheses be abbreviated as  $Q_1$  and  $Q_2$  allows Equation 3-16 to be expressed as

$$\frac{\partial \underline{f}}{\partial \underline{x}} = \frac{\partial T}{\partial \underline{x}} \underline{S}_T + T Q_1 + T Q_2 \frac{\partial z}{\partial \underline{x}} . \quad (3-18)$$

Solving for  $\partial z / \partial \underline{x}$  produces the desired sensitivity matrix

$$H = \frac{\partial z}{\partial \underline{x}} = (T Q_2)^{-1} \left( \frac{\partial \underline{f}}{\partial \underline{x}} - \left( \frac{\partial T}{\partial \underline{x}} \underline{S}_T + T Q_1 \right) \right) . \quad (3-19)$$

The inverted quantity  $T Q_2$  involves only derivatives with respect to the measurement vector. Thus the same equation can be used to evaluate the sensitivity matrices for consider variables ( $H_C$ ) and white noise ( $A$ ) by substituting  $x_C$  and  $y$  for  $x$ . For the star tracker, the same elements of  $x$  do not occur in more than one of the terms  $f$ ,  $T$ , and  $S_T$ . Therefore, for any  $x$  element, two of the three right-hand terms in equation 3-19 are zero.

We next display some expansion steps in the evaluation of  $(TQ_2)^{-1}$  and  $Q_1$ . The matrix  $Q_2$  can be written

$$Q_2 = \begin{bmatrix} \frac{\partial s_1}{\partial v_x} & \frac{\partial s_1}{\partial v_y} \\ \frac{\partial s_2}{\partial v_x} & \frac{\partial s_2}{\partial v_y} \\ \frac{\partial s_3}{\partial v_x} & \frac{\partial s_3}{\partial v_y} \end{bmatrix} \quad (3-20)$$

where the elements of  $S_T$  are given by Equation 3-8. Note that the expanded derivatives for  $Q_2$ , when written out in full, are actually

$$\frac{\partial s_i}{\partial v_j} = \frac{\partial s_i}{\partial \alpha} \frac{\partial \alpha}{\partial v_j} + \frac{\partial s_i}{\partial \beta} \frac{\partial \beta}{\partial v_j} \quad (3-21)$$

If  $T$  is approximately orthogonal, the coefficient  $(TQ_2)^{-1}$  can be simplified as follows:

$$(TQ_2)^{-1} = Q_2^{-1} T^{-1} \approx Q_2^{-1} T^T \quad (3-22)$$

Since  $Q_2$  is a non-square matrix it is necessary to compute the pseudo inverse

$$Q_2^{-1} \rightarrow Q_2^* = (Q_2^T Q_2)^{-1} Q_2^T$$

$$= \left( \begin{array}{ccc} \left( \frac{\partial s_1}{\partial z_1} \right)^2 & \left( \frac{\partial s_2}{\partial z_1} \right)^2 & \left( \frac{\partial s_3}{\partial z_1} \right)^2 & \frac{\partial s_1}{\partial z_1} \frac{\partial s_1}{\partial z_2} & \frac{\partial s_2}{\partial z_1} \frac{\partial s_2}{\partial z_2} & \frac{\partial s_3}{\partial z_1} \frac{\partial s_3}{\partial z_2} \\ \frac{\partial s_1}{\partial z_1} \frac{\partial s_1}{\partial z_2} & \frac{\partial s_2}{\partial z_1} \frac{\partial s_2}{\partial z_2} & \frac{\partial s_3}{\partial z_1} \frac{\partial s_3}{\partial z_2} & \left( \frac{\partial s_1}{\partial z_2} \right)^2 & \left( \frac{\partial s_2}{\partial z_2} \right)^2 & \left( \frac{\partial s_3}{\partial z_2} \right)^2 \end{array} \right)^{-1} / Q_2^T \quad (3-23)$$

where  $Q_2^T$  is obtained by transposing Equation 3-20.

Using Equations 3-8, 3-9, and 3-20, the first matrix in Equation 3-23 may be re-expressed as

$$(\Omega_2^T \Omega_2)^{-1} = \begin{pmatrix} p^2 + q^2 \cos^2 \alpha & pu + qv \cos^2 \alpha \\ pu + qv \cos^2 \alpha & u^2 + v^2 \cos^2 \alpha \end{pmatrix}^{-1} \quad (3-24)$$

where

$$\begin{aligned} p &= A_2 + 2A_4 V_x + A_6 V_y, \\ q &= B_2 + 2B_4 V_x + B_6 V_y, \\ u &= A_3 + 2A_5 V_x + A_6 V_y, \\ v &= B_3 + 2B_5 V_x + B_6 V_y. \end{aligned} \quad (3-25)$$

Performing the inverse operation algebraically gives

$$(\Omega_2^T \Omega_2)^{-1} = \frac{1}{\cos^2 \alpha (pv - qu)^2} \begin{pmatrix} u^2 + v^2 \cos^2 \alpha & -(pu + qv \cos^2 \alpha) \\ -(pu + qv \cos^2 \alpha) & p^2 + q^2 \cos^2 \alpha \end{pmatrix}. \quad (3-26)$$

In terms of defined quantities, Equation 3-25, the terms of  $\Omega_2^T$  (from Equation 3-20) are:

$$\begin{aligned} \partial s_1 / \partial v_x &= p \cos \alpha \\ \partial s_2 / \partial v_x &= p \sin \alpha \sin \beta - q \cos \alpha \cos \beta \\ \partial s_3 / \partial v_x &= -p \sin \alpha \cos \beta - q \cos \alpha \sin \beta \\ \partial s_1 / \partial v_y &= u \cos \alpha \\ \partial s_2 / \partial v_y &= u \sin \alpha \cos \beta - v \cos \alpha \cos \beta \\ \partial s_3 / \partial v_y &= -u \sin \alpha \cos \beta - v \cos \alpha \sin \beta. \end{aligned} \quad (3-27)$$

In summary, the sensitivity partials are given in general form by Equation 3-19. Since the variables  $\underline{x}$ ,  $\underline{x}_c$ ,  $\underline{v}$  apply to only one of  $f$ ,  $T$  and  $S_T$  at a time, Equation 3-19 simplifies for any given variable of differentiation. For noise, biases, etc. related to the spacecraft altitude we have

$$H \text{ (altitude)} \rightarrow (TQ_2)^{-1} \frac{\partial f}{\partial \underline{x}} . \quad (3-28)$$

For star tracker alignment errors

$$H \text{ (alignment)} \rightarrow -(TQ_2)^{-1} \frac{\partial T}{\partial \underline{x}} S_T , \quad (3-29)$$

and for tracker internal errors

$$H \text{ (internal to tracker)} \rightarrow -Q_2^{-1} Q_1 . \quad (3-30)$$

Since  $T$  is generally a product of a nominal rotation matrix and a small angle error matrix, ie.

$$T = T_c T_{BT} ,$$

the alignment sensitivity can be written

$$H \text{ (alignment)} \rightarrow -Q_2^{-1} T_c \frac{\partial T}{\partial \underline{x}} S_T .$$

#### 5.2.7 Sensitivity Example

Suppose we wish to calculate a particular sensitivity matrix element. As an example we pick  $\partial v_x / \partial (\delta T)$  where  $\delta T$  is a temperature error ( $\delta T$  may be a bias if temperature is measured onboard the spacecraft; or a consider type error if temperature is not measured). Let  $\delta T$  be the first element of  $\underline{x}$  or  $\underline{x}_c$  or  $\underline{v}$ . Then from Equation 3-30

$$\frac{\partial v_x}{\partial (\delta T)} = -(Q_2^{-1} Q_1)_{11} .$$

Using Equations 3-26 and 3-27 one can write  $Q_2^{-1}$

$$Q_2^{-1} = \frac{1}{c\alpha^2(pv-qu)} \begin{bmatrix} u^2 + v^2 c\alpha^2 & -(pu + qv c\alpha^2) \\ -(pu + qv c\alpha^2) & p^2 + q^2 c\alpha^2 \end{bmatrix} \begin{bmatrix} p c\alpha & p s\alpha s\beta & -p s\alpha c\beta \\ -q c\alpha & q s\alpha s\beta & -q c\alpha c\beta \\ u c\alpha & u s\alpha s\beta & -u s\alpha c\beta \\ -v c\alpha & -v s\alpha s\beta & -v c\alpha c\beta \end{bmatrix}$$

(3-31)

where  $c$  and  $s$  denote cosine and sine, respectively. Using Equations 3-13 and 3-14, and the vector form of  $Q_1$  for a single element, gives

$$(Q_1)_{j1} = \begin{pmatrix} c\alpha \\ s\alpha s\beta \\ -s\alpha c\beta \end{pmatrix} \left( \frac{\partial A_1}{\partial T} + \frac{\partial A_2}{\partial T} v_x + \frac{\partial A_3}{\partial T} v_y + \frac{\partial A_4}{\partial T} v_x^2 + \frac{\partial A_5}{\partial T} v_y^2 + \frac{\partial A_6}{\partial T} v_x v_y \right)$$

$$+ \begin{pmatrix} 0 \\ -c\alpha c\beta \\ -c\alpha s\beta \end{pmatrix} \left( \frac{\partial B_1}{\partial T} + \frac{\partial B_2}{\partial T} v_x + \frac{\partial B_3}{\partial T} v_y + \frac{\partial B_4}{\partial T} v_x^2 + \frac{\partial B_5}{\partial T} v_y^2 + \frac{\partial B_6}{\partial T} v_x v_y \right).$$

(3-32)

Picking  $\alpha = \beta = 0$ , i.e. the sensitivity at the center of the field of view, and multiplying out Equation 3-31 gives

$$Q_2^{-1} = \frac{1}{(pv-qu)} \begin{pmatrix} v & u & 0 \\ -q & -p & 0 \end{pmatrix}.$$

From Equation 3-32

$$(Q_1)_{j1} \rightarrow \begin{pmatrix} 1 \cdot \Sigma A \text{ Terms} \\ -1 \cdot \Sigma B \text{ Terms} \\ 0 \end{pmatrix},$$

therefore

$$\frac{\partial z}{\partial x^T}_{11} = \frac{\partial v_x}{\partial (\delta T)} = \frac{1}{(pv-qu)} (v \cdot \Sigma A \text{ Terms} - u \cdot \Sigma B \text{ Terms}) . \quad (3-33)$$

Examination of the forms of  $p$ ,  $q$ ,  $u$ ,  $v$ , as given in Equation 3-25, show that normally

$$\begin{aligned} A_2 &>> B_2 , \\ A_3 &<< B_3 , \\ A_4 &>> B_4 , \\ A_5 &<< B_5 , \\ A_6 &\approx B_6 . \end{aligned}$$

This is because the cross-coupling terms due to rotation and non-orthogonality are nominally small. Also  $A_6$  and  $B_6$  are small with  $\Delta_6 v_y \ll A_2$ , etc. These inequalities imply that

$$p \gg q, v \gg u$$

so that Equation 3-33 becomes approximately

$$\frac{\partial v_x}{\partial (\delta T)} \approx \frac{1}{pv} \cdot v \cdot \Sigma A \text{ Terms} = \frac{1}{p} \frac{\partial}{\partial T} (A) ,$$

REPRODUCIBILITY OF THE  
ORIGINAL PAGE IS POOR

or

$$\frac{\partial V_x}{\partial (\delta T)} = \left| \frac{\left( \frac{\partial A_1}{\partial T} + \frac{\partial A_2}{\partial T} V_{xo} + \frac{\partial A_3}{\partial T} V_{yo} + \frac{\partial A_4}{\partial T} V_{xo}^2 + \frac{\partial A_5}{\partial T} V_{yo}^2 + \frac{\partial A_6}{\partial T} V_{xo} V_{yo} \right)}{(A_2 + 2A_4 V_{xo} + A_6 V_{yo})} \right|_{T = T_c} \quad (3-34)$$

where  $T = T_c$  is the calibration temperature, and the subscript "o" for the voltages indicates the values assumed at  $\alpha = \beta = 0$ . The behavior of Equation 3-34 can be seen more clearly by considering the tracker calibration to be linear without cross-coupling. Then Equation 3-34 reduces to

$$\frac{\partial V_x}{\partial (\delta T)} = \frac{\frac{\partial A_1}{\partial T} + \frac{\partial A_2}{\partial T} V_{xo}}{A_2} \quad (3-35)$$

The intuitive content of this equation is more clearly displayed by some manipulations. We first re-express the right side

$$\frac{\frac{\partial A_1}{\partial T} + \frac{\partial A_2}{\partial T} V_{xo}}{A_2} = \left( \frac{\partial \alpha}{\partial (\delta T)} \right) / \left( \frac{\partial V_x}{\partial (\delta T)} \right)$$

Substituting into Equation 3-35 and solving for  $(\partial \alpha / \partial (\delta T))$  yields

$$\frac{\partial \alpha}{\partial (\delta T)} = \frac{\partial \alpha}{\partial V_x} \frac{\partial V_x}{\partial (\delta T)} \quad (3-36)$$

### 3.3 LANDMARK MEASUREMENT EQUATION

#### 3.3.1 Introduction

One of the primary instruments being planned for an EOS type satellite is the multispectral scanner. This device is a natural for navigation measurement using landmarks within the field of view. There is an important system advantage in using the device in this manner, and that is that landmark sightings can provide both attitude and ephemeris information simultaneously. For example, it is shown in Section 2 that scanner sightings of landmarks coupled with range and range rate measurements from ground stations could obviate the need for a star tracker onboard the spacecraft.

This section derives a general measurement equation for the landmark sightings including all of the known potential error sources. The equation is made deliberately general so that various error sources that are small are not overlooked and can be systematically dropped if desired when the equation is applied in practice.

#### 3.3.2 Basic Scanner Operation and Measurement

The scanner moves a small field of view across the Earth's surface at a rate designed to give full area coverage. At regular time intervals the sensor output is sampled to yield a sequence of effective picture elements. If a known landmark has a distinguishable output, its position within a scan can be in principle determined by application of a recognition process. To this end it has been suggested that searchlights and mirrors be used as landmarks since they are nearly point sources with distinguishable spectral characteristics. The searchlight and mirror types of landmarks yield a sharply defined signal that is essentially confined to two picture elements. Thus if the approximate position of the landmark is predictable over a limited part of the scan, it may be possible to use a finer signal sample interval in order to establish the position of the landmark to within one optical resolution element.

Fundamental to the navigation problem is the association of event times within the scanner system with universal time which is used in ephemeris calculations. Since the scanner scans at a known rate, the inertial scanner pointing direction can be obtained by observing the universal time at the beginning of a scan on which the landmark is sighted, and adding to the estimated starting position an angle which is a function of the scan rate and the time between scan initiation and landmark detection. The fundamental measurement is therefore the time interval between scan initiation and landmark sighting.

If the navigation calculations are to be done at an earth facility it will be necessary to transmit from satellite to earth the scan initiation timing pulse (probably for several scans) and the time interval between detection and initiation. The latter can presumably be processed onboard the satellite.

### 3.3.3 Formal Measurement and Noise

The linearized measurement equation considering the various categories of noise is

$$\delta \underline{z} = \frac{\partial \underline{z}}{\partial \underline{x}} \delta \underline{x} + \frac{\partial \underline{z}}{\partial \underline{x}_c} \delta \underline{x}_c + \frac{\partial \underline{z}}{\partial \underline{v}} \delta \underline{v}$$

where  $\underline{x}$ ,  $\underline{x}_c$ ,  $\underline{v}$  are defined in Equation 3-1. For the multispectral scanner  $\underline{z}$  is simply a scalar  $\underline{z} + \Delta t$ .

The geometric equations (discussed below) relating scanner line-of-sight to orbit-inertial coordinates involve the basic measurement (time of landmark sighting) by means of direction cosines of the scan angle  $\alpha$ . The linear scan angle-time relationship assumed here is only one of a number of possible  $\alpha(t)$  relationships which result from various mechanical scanner designs. The linear relationship is relevant to rotating mirror scanners as in the Nimbus and ITOS satellites, the

ERTS scanning mirror, and rotating satellites such as ATS I, II, Pioneer 10, and SMS. We write the linear (error-free) relationship as

$$\alpha = \alpha(t_0) + \dot{\alpha}\Delta t. \quad (3-37)$$

where  $\alpha(t_0)$  is the angular deviation of the scanner field of view from null at scan initiation,  $\dot{\alpha}$  is the scan rate, and  $\Delta t$  is the landmark detection time interval. The true value of  $\alpha$  includes errors whose sources are identified by examining the differential form of Equation 3-37. Thus

$$\delta\alpha = \delta\alpha_0 + (\delta\dot{\alpha})(\Delta t) + (\dot{\alpha})\delta(\Delta t). \quad (3-38)$$

Here  $\delta\alpha_0$  represents an uncertainty in the scan field width,  $\delta\dot{\alpha}$  represents a scan rate uncertainty, and  $\delta(\Delta t)$  a timing error. The latter consists of two errors, namely

$$\delta(\Delta t) = \delta t_d - \delta t_0 \quad (3-39)$$

where  $t_d$  is a time-of-detection error and  $\delta t_0$  is a scan initialization error. Scanner related sources for these errors are listed below in Table 3-2. These were obtained in part from discussions with O. Weinstein of GSFC and from Reference 18. The initial scan position bias is due partly to the internal scanner mechanism and partly to the alignment of the scanner with the spacecraft body axes. The scanner-spacecraft body alignment error is treated separately as a small angle rotation matrix in the discussion which follows. Angular alignment errors are expected to be on the order of  $100 \mu$  rad.

The consider biases are slowly changing errors of random amplitude, for example, errors associated with changes in calibrated settings due to temperature fluctuations.

Since no time-of-detection algorithm has been designed and no tests have been made, the random error associated with detection cannot be closely estimated. However the searchlight experiment data

**TABLE 3-2**  
**MSS LANDMARK SIGHTING ERRORS**

**Estimatable Bias Errors ( $1\sigma$ )**

Initial Scan Position ( $\delta\alpha_0$ )	-	4 $\mu$ rad
Scan Rate Bias ( $\dot{\delta\alpha}$ )	-	0.1 %

**Consider Bias Errors ( $1\sigma$ )**

Initial Scan Position Due to Thermal Changes and Wear ( $\delta\alpha_0$ )	-	< 4 $\mu$ rad
Scan Rate Drift ( $\dot{\delta\alpha}$ )	-	.003 %
Initiation Time Error ( $\delta t_0$ )	-	$10^{-6}$ % of interval

**White Noises ( $1\sigma$ )**

Side-To-Side Scan Line Jitter ( $\delta\theta_0$ )	-	4 $\mu$ rad
Scan Line Synchronization ( $\delta t_0$ )	-	4 $\mu$ rad
Time of Detection ( $\delta t_d$ )	-	10 $\mu$ rad ?

generally show the landmark confined to a single or at most two picture elements. Thus if the midpoint of the maximum signal picture element is used as a marker the uncertainty will be roughly a half picture element. The discrimination accuracy could be improved by using a smaller sampling interval for a period defined by the expected landmark sighting time interval.

### 3.3.4 Scanner-Inertial Coordinate Relationship

The nominal vector relationship between landmark, spacecraft and scanner line of sight vectors in spacecraft body coordinates can be written as

$$\hat{T}_{BO} \hat{T}_{OI} \hat{u} = \hat{T}_{BS} \hat{l} \hat{m} . \quad (3-40)$$

Here  $T_{BO}$  and  $T_{OI}$  are the rotation matrices defined above, and  $T_{BS}$  is a rotation describing the orientation of the scanner in spacecraft body coordinates. Previously (Ref. 1)  $T_{BS}$  consisted of a single 90° rotation corresponding to an x axis boresight aimed straight down along the body z axis. In the interest of generality  $T_{BS}$  is defined here to be a three angle rotation matrix.  $\hat{u}$  is a landmark position unit vector in inertial coordinates and  $\hat{l} \hat{m}$  is a unit vector along the scanner line of sight towards the landmark. In the presence of errors the general form of Equation 3-40 changes only by the matrix  $T(\delta\gamma)$  which represents small angle errors in the scanner alignment with the spacecraft body axes.  $T(\delta\gamma)$  is introduced as a multiplier of  $T_{BS}$ . The error form of  $\hat{u}$  is given by

$$\hat{u} = \frac{\hat{l} - \underline{r} + \underline{\delta l}}{d} \quad (3-41)$$

where  $\underline{r}$  is the satellite position vector,  $\underline{l}$  is the landmark position vector, and  $\underline{\delta l}$  is a landmark position error. The scalar  $d$  is just the magnitude of the vector numerator. Figure 3-2 illustrates the landmark sighting geometry.

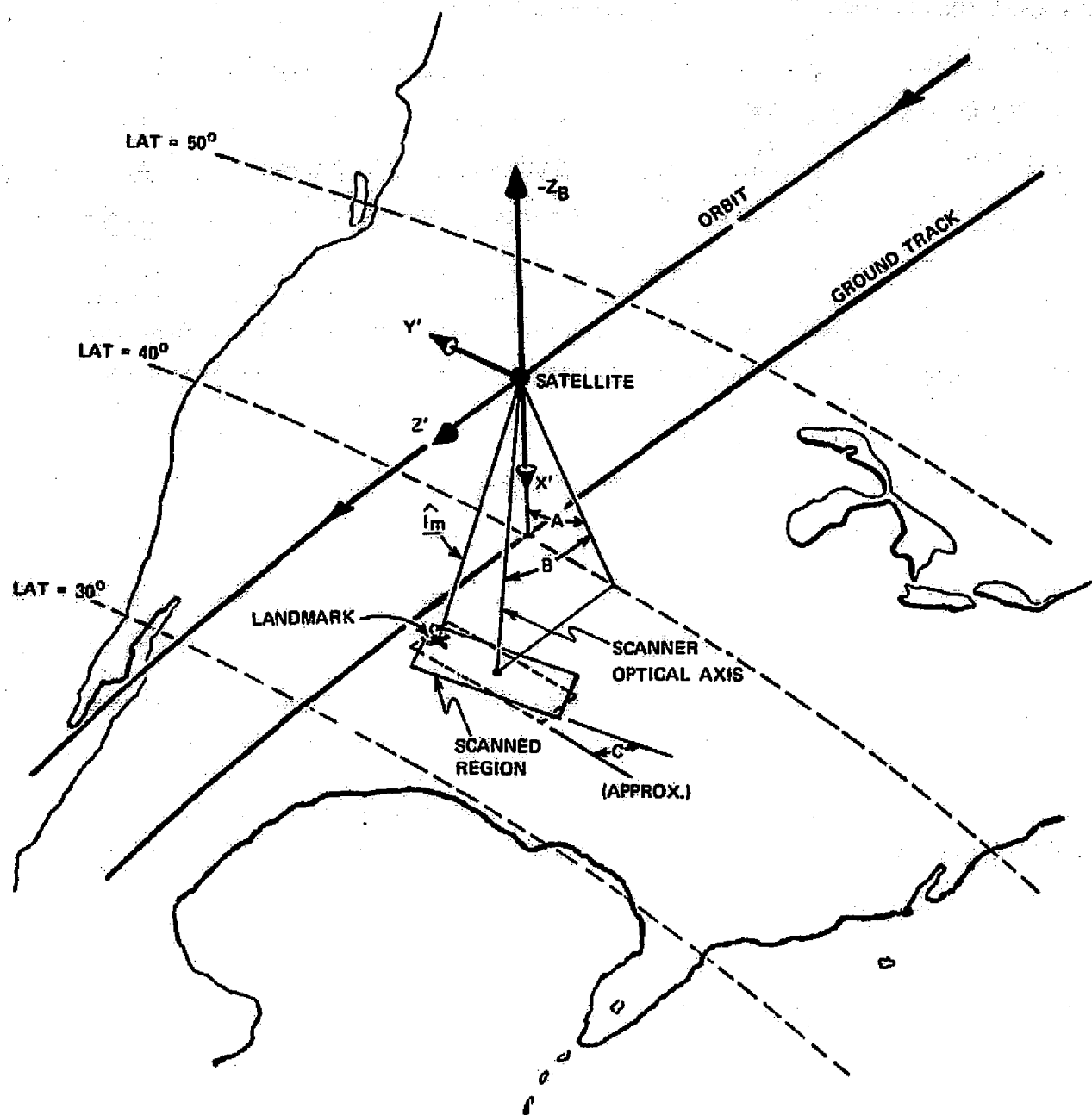


Figure 3-2 Landmark Sighting Geometry

Letting the scanner x axis point along the center of the scan allows the alignment matrix  $T_{BS}$  to be defined as

$$T_{BS} = \begin{pmatrix} 1 & 0 & 0 \\ 0 & CC & SC \\ 0 & -SC & CC \end{pmatrix} \begin{pmatrix} CB & 0 & -SB \\ 0 & 1 & 0 \\ SB & 0 & CB \end{pmatrix} \begin{pmatrix} CA & SA & 0 \\ -SA & CA & 0 \\ 0 & 0 & 1 \end{pmatrix} \begin{pmatrix} 0 & 0 & -1 \\ 0 & 1 & 0 \\ 1 & 0 & 0 \end{pmatrix}^T. \quad (3-42)$$

The individual rotations are defined as follows:  $90^\circ$  about body y axis; through angle A about  $z'$ ; through angle B about  $y'$ ; finally through angle C about  $x'$ . In the scanner coordinate system at any instant, the scan direction will be defined by the nominal scan angle  $\alpha$ . Thus the nominal form of  $\underline{\text{lm}}$  is just

$$\hat{\underline{\text{lm}}} = \begin{pmatrix} \cos (\alpha_0 + \dot{\alpha}z) \\ \sin (\alpha_0 + \dot{\alpha}z) \\ 0 \end{pmatrix}, \quad (3-43)$$

where  $z$  is the measured time of detection  $z = t_d - t_o$ . Since the line scan type of multispectral scanner which we are considering here registers six scan lines simultaneously, it is possible to have a displacement error in a landmark sighting when the landmark image falls between two detectors. Considering this displacement to be the angle  $\beta$ , and adding the error sources in  $\alpha$  (Equation 3-38), gives the actual  $\underline{\text{lm}}$  value, namely

$$\hat{\underline{\text{lm}}} = \begin{pmatrix} \cos (\alpha + \delta\alpha_0 + \delta\dot{\alpha}z + \dot{\alpha}\delta z) \cos \beta \\ \sin (\alpha + \delta\alpha_0 + \delta\dot{\alpha}z + \dot{\alpha}\delta z) \cos \beta \\ \sin \beta \end{pmatrix}. \quad (3-44)$$

The complete geometric equation in the presence of errors in the measurement is thus (combining Equations 3-40, 3-41, and 3-44)

$$T_{BO} T_{OI} \frac{1}{d} \begin{pmatrix} l_x + \delta l_x - x \\ l_y + \delta l_y - y \\ l_z + \delta l_z - z \end{pmatrix} = T_{BS} T(\delta\sigma) \begin{pmatrix} \cos(\alpha + \delta\alpha_0 + \delta\alpha_z + \dot{\alpha}\delta z) \cos \beta \\ \sin(\alpha + \delta\alpha_0 + \delta\alpha_z + \dot{\alpha}\delta z) \cos \beta \\ \sin \beta \end{pmatrix}. \quad (3-45)$$

### 3.3.5 Evaluation of the Sensitivity Partial Derivatives

Equation 3-45 can be written in the same general form as Equation 3-15, namely

$$f(\underline{x}) = T(\underline{x}) \hat{lm}[\alpha(\underline{x}, \underline{z}), \beta(\underline{x}, \underline{z})].$$

To obtain the sensitivity to the state we again solve

$$\frac{\partial f}{\partial \underline{x}} = \frac{\partial T(\underline{x})}{\partial \underline{x}} \hat{lm} + T(\underline{x}) \frac{\partial \hat{lm}}{\partial \underline{x}}$$

for  $\frac{\partial z}{\partial \underline{x}}$ . The result is (here  $z$  is a scalar)

$$\underline{H} = \frac{\partial z}{\partial \underline{x}} = (TQ_2)^{-1} \left( \frac{\partial f}{\partial \underline{x}} - \left( \frac{\partial T}{\partial \underline{x}} \hat{lm} + TQ_1 \right) \right). \quad (3-46)$$

Rewriting with  $T^{-1}$  multiplied out gives

$$\underline{H} = Q_2^{-1} \left( T^{-1} \frac{\partial f}{\partial \underline{x}} - \left( T^{-1} \frac{\partial T}{\partial \underline{x}} \hat{lm} + Q_1 \right) \right). \quad (3-47)$$

Recall that previously

$$Q_2 = \left( \frac{\partial \hat{1}_m}{\partial \alpha} \frac{\partial \alpha}{\partial z} + \frac{\partial \hat{1}_m}{\partial \beta} \frac{\partial \beta}{\partial z} \right) .$$

In the present case this becomes [since  $\beta = \beta(z)$ ]

$$Q_2 = \frac{\partial \hat{1}_m}{\partial \alpha} \frac{\partial \alpha}{\partial z} = \begin{pmatrix} -\sin \alpha \\ \cos \alpha \\ 0 \end{pmatrix} \dot{\alpha}, \quad (3-48)$$

where partial derivatives are evaluated at nominal (error-free) conditions. Taking the inverse gives

$$Q_2^{-1} = \frac{1}{\dot{\alpha}} (-\sin \alpha \cos \alpha \ 0) . \quad (3-49)$$

It remains to calculate the other terms in Equation 3-47. Let the state vector be defined as follows:

$$\underline{x}^T = (\theta, \phi, \psi; B_x, B_y, B_z; x, y, z; \dot{x}, \dot{y}, \dot{z}; \delta l_x, \delta l_y, \delta l_z, \delta \alpha, \delta \beta, \delta \gamma, \delta \dot{\alpha}) .$$

The angles  $\theta$ ,  $\phi$ ,  $\psi$  are the altitude definition angles contained in the rotation  $T_{BO}$  introduced in Equation 3-40. This matrix is defined in Section 2.4.  $B_x$ ,  $B_y$ ,  $B_z$  are gyro bias drift rates also defined in Section 2.4. The quantities  $\delta l$  are landmark position biases corresponding to an uncertainty in the geoid location of a known landmark. For example, if the landmark is a search light surveyed in by common survey techniques, the magnitude of this error is approximately 10 meters.<sup>(19)</sup> State vector elements  $x$ ,  $y$ ,  $z$  are just the satellite coordinates,  $\delta \gamma$  is the scanner-body alignment bias (may have three components), and  $\delta \alpha$ ,  $\delta \beta$  and  $\delta \dot{\alpha}$  are as defined above.

The first three state elements enter Equation 3-46 only through the first term in brackets. These we may write

$$\begin{aligned} H_{\theta, \phi, \psi} &= Q_2^{-1} T^{-1} \frac{\partial f}{\partial \underline{x}}, \\ &= Q_2^{-1} T^{-1} \frac{\partial T_{BO}}{\partial \underline{x}} T_{OI} \hat{u}. \end{aligned} \quad (3-50)$$

Now  $T = T_{BS} T_{\delta\gamma}$ , thus  $T^{-1} = T_{\delta\gamma}^{-1} T_{BS}^{-1}$ . Since  $T_{BS}$  is orthogonal  $T_{BS}^{-1} = T_{BS}^T$ , and since  $T(\delta\gamma)$  is infinitesimal  $T^{-1}(\delta\gamma) \approx T^T(\delta\gamma)$ . Substituting  $Q_2^{-1}$  (defined in Equation 3-49) and  $T^{-1}$  yields

$$H_{\theta, \phi, \psi} = \frac{1}{\alpha} (-\sin \alpha \cos \alpha \ 0) T_{BS}^T \frac{\partial T_{BO}}{\partial \underline{x}} T_{OI} \hat{u}, \quad (3-51)$$

where  $\underline{x}$  here represents only elements  $\theta, \phi, \psi$ .  $T(\delta\gamma)$  does not appear because its nominal value is the identity matrix. Evaluating the partial derivative gives (the nominal values of  $\theta$  and  $\psi$  are  $0^\circ$ )

$$\frac{\partial T_{BO}}{\partial \theta} = h_\theta = \begin{pmatrix} -C\theta & -S\theta & 0 \\ 0 & 0 & 0 \\ S\theta & -C\theta & 0 \end{pmatrix}, \quad \frac{\partial T_{BO}}{\partial \phi} = h_\phi = \begin{pmatrix} 0 & 0 & 0 \\ -C\theta & -S\theta & 0 \\ 0 & 0 & 1 \end{pmatrix},$$

$$\frac{\partial T_{BO}}{\partial \psi} = h_\psi = \begin{pmatrix} 0 & 0 & 0 \\ -S\theta & C\theta & 0 \\ 0 & 0 & 0 \end{pmatrix}.$$

Elements of the sensitivity vector  $\underline{H}$  for the first three state elements are thus

$$\begin{aligned}\frac{\partial z}{\partial \theta} &= \underline{J} \underline{h}_\theta \underline{K}, \\ \frac{\partial z}{\partial \phi} &= \underline{J} \underline{h}_\phi \underline{K} \\ \frac{\partial z}{\partial \psi} &= \underline{J} \underline{h}_\psi \underline{K},\end{aligned}\tag{3-52}$$

where  $\underline{J} = Q_2^{-1} T_{BS}^T$  and  $\underline{K} = T_{OI} \hat{\underline{u}}$ .

Elements of  $\underline{H}$  for the second set of state vector elements also involve only derivatives of  $\underline{f}$ , thus

$$\underline{H}_{\delta l} = Q_2^{-1} T_{BS}^T T_{BO} T_{OI} \frac{\partial \hat{\underline{u}}}{\partial \delta l}.\tag{3-53}$$

Evaluating the derivatives of  $\hat{\underline{u}}$  gives

$$\frac{\partial \hat{\underline{u}}}{\partial (\delta l_x)} = h_{l_x} = \frac{1}{d^3} \begin{pmatrix} -u_x^2 + d^2 \\ -u_x u_y \\ -u_z u_x \end{pmatrix}, \quad \frac{\partial \hat{\underline{u}}}{\partial (\delta l_y)} = h_{l_y} = \frac{1}{d^3} \begin{pmatrix} -u_x u_z \\ -u_y^2 + d^2 \\ -u_z u_y \end{pmatrix},$$

$$\frac{\partial \hat{\underline{u}}}{\partial (\delta l_z)} = h_{l_z} = \frac{1}{d^3} \begin{pmatrix} -u_x u_z \\ -u_y u_z \\ -u_z^2 + d^2 \end{pmatrix},\tag{3-54}$$

where  $u_x = l_x - x$  etc. according to Equation 3-41. Nominally  $\delta l = 0$ .

Let  $\underline{I} = Q_2^{-1} T_{BS}^T T_{BO} T_{OI}$ , then the H elements associated with  $\delta l$  are

$$\frac{\partial z}{\partial (\delta l_x)} = \underline{I} \underline{h}_{l_x},$$

$$\frac{\partial z}{\partial (\delta l_y)} = \underline{I} \underline{h}_{l_y},$$

$$\frac{\partial z}{\partial (\delta l_z)} = \underline{I} \underline{h}_{l_z}. \quad (3-55)$$

The sensitivity to satellite position is identical to the above except for a change of sign, thus

$$\frac{\partial z}{\partial x} = -\underline{I} \underline{h}_{l_x},$$

$$\frac{\partial z}{\partial y} = -\underline{I} \underline{h}_{l_y},$$

$$\frac{\partial z}{\partial (z)} = -\underline{I} \underline{h}_{l_z}. \quad (3-56)$$

Sensitivity to  $\delta \gamma$  involves the second term of Equation 3-47.

Thus

$$H_{\delta \gamma} = -Q_2^{-1} \frac{\partial T(\delta \gamma)}{\partial (\delta \gamma)} \hat{l_m} .$$

If we write

$$T(\delta\gamma) = \begin{pmatrix} 1 & 0 & 0 \\ 0 & 1 & \delta\gamma \\ 0 & -\delta\gamma & 1 \end{pmatrix}$$

then

$$\frac{\partial T}{\partial (\delta\gamma)} = \begin{pmatrix} 0 & 0 & 0 \\ 0 & 0 & 1 \\ 0 & -1 & 0 \end{pmatrix} = h_{\delta\gamma}$$

and

$$H_{\delta\gamma} = -Q_2^{-1} \hat{h}_{\delta\gamma} \underline{l}^m. \quad (3-57)$$

The remaining three state elements involve the last term of Equation 3-47, and can be expressed as:

$$H_{(\delta\alpha_0, \delta\beta, \delta\dot{\alpha})} = -Q_2^{-1} Q_1.$$

Recall that  $Q_1$  is defined as  $\hat{\underline{l}}^m / \partial \underline{x}^T$ , or in this case

$$Q_1 = \left( \frac{\partial \hat{\underline{l}}^m}{\partial \alpha} \frac{\partial \alpha}{\partial \underline{x}^T} + \frac{\partial \hat{\underline{l}}^m}{\partial \beta} \frac{\partial \beta}{\partial \underline{x}^T} \right).$$

One of these terms is therefore associated with each of  $\delta\alpha_0$ ,  $\delta\beta$  and  $\delta\dot{\alpha}$ . Differentiating Equation 3-44 where  $\alpha$  is taken to be the "true" value, i.e.  $\alpha = \alpha + \delta\alpha$ , with  $\delta\alpha$  representing the error terms, gives

$$Q_1(\delta\alpha_0) = \begin{pmatrix} -\sin \alpha \\ \cos \alpha \\ 0 \end{pmatrix} \cdot 1$$

thus for this state element

$$\underline{H}_{\delta \alpha_0} = - \frac{1}{\dot{\alpha}} (-\sin \alpha \cos \alpha \ 0) \begin{pmatrix} -\sin \alpha \\ \cos \alpha \\ 0 \end{pmatrix} = \frac{1}{\dot{\alpha}} . \quad (3-58)$$

For  $\delta \beta$  we have

$$\underline{H}_{\delta \beta} = - \frac{1}{\dot{\alpha}} (-\sin \alpha \cos \alpha \ 0) \begin{pmatrix} 0 \\ 0 \\ 1 \end{pmatrix} = 0 . \quad (3-59)$$

Finally for  $\underline{H}_{\delta \dot{\alpha}}$

$$\underline{H}_{\delta \dot{\alpha}} = - \frac{z}{\dot{\alpha}} . \quad (3-60)$$

### 3.4 CONCLUSIONS

It is possible to derive general and realistic measurement equations for optical navigation sensors following a three-step procedure. The steps are:

- (1) Determine the actual measured quantity in terms of the sensor operation (e.g. pulse time, voltage levels, etc.), and the types of noise associated with the measurement (e.g. bias, white, etc.).
- (2) Write the geometric state, measurement, and error relationship in general form

$$g(\underline{z}) = f(\underline{x})$$

where  $\underline{z}$  is the measurement vector and  $\underline{x}$  is the state vector.

- (3) Differentiate this relationship implicitly to obtain the linearized measurement equation used in the linear estimation of nonlinear systems.

These steps have been applied to star tracker and multispectral scanner measurements. Specific models of these devices were considered, and the resulting measurement equations are fairly comprehensive.

## SECTION 4

### HORIZON UTILIZATION STUDY

#### 4.1 INTRODUCTION

In this report some preliminary results are given for the Horizon Utilization Study, which is an investigation into the use of infra-red (IR) horizon measurements to estimate satellite attitude and gyro bias drift for a geosynchronous earth-observing satellite. It is assumed that the satellite has three orthogonal body-mounted gyros aligned with its principal body axes, and that the satellite maintains a local vertical attitude history like that used in the Modified Landmark Utilization Study of Section 2.

The primary objectives of this study are to review what is presently known about the Earth's horizon in the IR region, and determine what might best be achieved in the estimation of satellite attitude and gyro bias drift when using the most accurate instruments for horizon sensing. Unfortunately, there has been some difficulty in identifying those instruments which might be best for this application since none of the known instruments have accuracies which are comparable to the small angular uncertainty (approximately 0.004 degree) of the IR horizon when observed at geosynchronous altitudes. The typical accuracy of devices used for IR horizon sensing is about 0.1 degree. Design studies by various companies, such as Barnes Engineering (20,21), indicate that the better horizon sensors are capable of accuracies near 0.05 degree, with detector-preamplifier noise being one of the limiting factors. In addition, these instruments have usually been designed for operation at much lower altitudes than what is desired in this study, and must therefore work with the much larger angular uncertainty of the IR horizon. As yet no instrument has been identified which would have a measurement accuracy comparable to the uncertainty of the IR horizon when observed at geosynchronous altitudes. However, for the purposes of this study, it is assumed that such an instrument does exist and has an overall measurement accuracy (including horizon uncertainty) of 0.01 degree or better.

In this report the performance results are given for one type of hypothetical horizon sensor. This sensor is assumed to be a body-fixed device which simultaneously senses the Earth's horizon at a number of equally spaced points and provides an indication of local vertical. In other words, it may be looked upon as a device which essentially tracks the center of the Earth. The measurement equations for this device are presented in Section 4.3.2. To simplify matters, it is assumed in this first analysis that the Earth's horizon is circular. However, as indicated later in the comments on the performance results (Section 4.4), the next step in this study would include consideration of the actual non-circular shape of the Earth's horizon, which would provide some additional information on yaw attitude.

It should be noted that measurement equations have also been developed for a second type of horizon sensor, but are not presented in this report since they have not yet been incorporated in the computer simulation. This device consists of two small FOV sensors which spin about body-fixed axes in such a manner that one conically sweeps across the northern hemisphere while the other sweeps in a similar fashion across the southern hemisphere.

#### 4.2 INFRA-RED HORIZON UNCERTAINTY

Various studies<sup>(22,23)</sup> have shown that the  $15\mu$  bands of  $\text{CO}_2$  provide horizon markers that display the least sensitivity to variations in atmospheric phenomena such as cloudiness and surface effects. Accordingly, most of the theoretical and experimental programs aimed at IR horizon fluctuation assessment have been confined to this spectral region. Theoretical analyses by Wark<sup>(24)</sup>, and Thomas et al<sup>(25)</sup> have shown maximum altitude fluctuations of 3 to 4 kilometers for the one-half maximum radiant intensity marker after corrections for latitude and season have been made. These fluctuations are primarily due to short term temperature variations. Fluctuations of this magnitude have been confirmed experimentally by Dodgen<sup>(22)</sup>, and Girard<sup>(26)</sup>. For a satellite at 1000 km altitude, a 4 km displacement on the horizon subtends an angle of about 0.06 degree. At geosynchronous altitude the angular subtense is 0.004 degree.

### 4.3 STATE AND MEASUREMENT EQUATIONS

In this initial covariance analysis, frequent use is made of the analytical techniques and definitions previously described in Section 2 for the Modified Landmark Utilization Study. Also included in this study are most of the coordinate systems defined in Section 2.3.

#### 4.3.1 State Equations

The state of the system  $\underline{x}$  is defined as the following six dimensional vector:

$$\underline{x}^T = (\theta, \phi, \psi, B_x, B_y, B_z) \quad (4-1)$$

where

$\theta, \phi, \psi$  - Euler angles defining the body attitude with respect to the orbital frame.

$B_x, B_y, B_z$  - Bias drift of roll (X), pitch (Y), and yaw (Z) gyros.

The state equation for this system is the previously derived Equation 2-21 of Section 2. Since this equation is non-linear, use is made of the corresponding linearized expression of Equation 2-28 where the adopted state parameters represent the perturbations of the original parameters. The transition matrix for the linearized state equation is that given in Equation 2-33.

#### 4.3.2 Measurement Equations

As previously indicated in Section 4.1, the horizon sensor is assumed to be a body-fixed device which simultaneously senses the Earth's horizon at a number of equally spaced points and provides an indication of local vertical which is analytically represented as a unit LOS vector to the center of the Earth.

\*For the purposes of this study, it is assumed that the satellite position and velocity are known without any uncertainty.

The estimated direction of this unit LOS vector in body coordinates is:

$$\hat{\underline{u}}_{\text{LOS}} = T_{\text{BO}} T_{\text{OI}} \text{Unit}(-\underline{r}) \quad (4-2)$$

where  $\underline{r}$  is the estimated satellite position vector in basic inertial coordinates, and  $T_{\text{OI}}$  and  $T_{\text{BO}}$  are the coordinate transformation matrices defined in Section 2.3.

The unit vector defining the measured LOS to the center of the Earth in body coordinates is:

$$\tilde{\underline{u}}_{\text{LOS}} = \begin{bmatrix} 1 & 0 & 0 \\ 0 & \cos\alpha & -\sin\alpha \\ 0 & \sin\alpha & \cos\alpha \end{bmatrix} \begin{bmatrix} \cos\beta & 0 & \sin\beta \\ 0 & 1 & 0 \\ -\sin\beta & 0 & \cos\beta \end{bmatrix} \begin{bmatrix} 0 \\ 0 \\ 1 \end{bmatrix} \quad (4-3)$$

where  $\alpha$  and  $\beta$  are Euler angle rotations about the roll (X) and pitch (Y) axes of the spacecraft, respectively. These measured angles consist of the true angles plus a measurement noise ( $v$ ) which is assumed to be white and gaussian. In equation form,

$$\alpha = \alpha_{\text{True}} + v_\alpha \quad (4-4)$$

$$\beta = \beta_{\text{True}} + v_\beta$$

The linearized measurement equation for this case is:

$$\delta \underline{z} = H \delta \underline{x} + A \delta \underline{y} \quad (4-5)$$

where the matrix  $H$  is:

$$H = \left. \frac{\partial \hat{\underline{u}}_{\text{LOS}}}{\partial \underline{x}} \right|_{\underline{x}=\underline{x}_0} = \left. -\frac{\partial}{\partial \underline{x}} \left[ T_{\text{BO}} T_{\text{OI}} \text{Unit}(-\underline{r}) \right] \right|_{\underline{x}=\underline{x}_0}$$

$$= \left. \frac{\partial}{\partial \underline{x}} [T_{\text{BO}}] T_{\text{OI}} \text{Unit}(-\underline{r}) \right|_{\underline{x}=\underline{x}_0}$$

$$= \left[ \begin{array}{c|c|c|c|c|c|c} H_0 & H_\phi & H_\psi & 0 & 0 & 0 \\ \hline 0 & 0 & 0 & 0 & 0 & 0 \end{array} \right] \quad (4-6)$$

\*See footnote on page 2-20.

where  $\underline{x}_0$  is the nominal state (i.e.,  $\phi=\psi=0$ ) and

$$\underline{H}_\theta = \begin{bmatrix} -c\theta & -s\theta & 0 \\ 0 & 0 & 0 \end{bmatrix} \quad T_{OI} \text{ Unit } (-\underline{r}) \quad (4-7)$$

$$\underline{H}_\phi = \begin{bmatrix} 0 & 0 & 0 \\ -c\theta & -s\theta & 0 \end{bmatrix} \quad T_{OI} \text{ Unit } (-\underline{r}) \quad (4-8)$$

$$\underline{H}_\psi = \begin{bmatrix} 0 & 0 & 1 \\ -s\theta & c\theta & 0 \end{bmatrix} \quad T_{OI} \text{ Unit } (-\underline{r}) \quad (4-9)$$

The matrix A in Equation 4-5 is:

$$A = \left. \frac{\partial \tilde{u}_{LOS}}{\partial \underline{v}} \right|_{\begin{array}{l} \alpha = \alpha_0 \\ \beta = \beta_0 \end{array}} = \begin{bmatrix} 0 & c\beta_0 \\ -ca_0 & c\beta_0 \\ sa_0 & c\beta_0 \end{bmatrix} \quad (4-10)$$

which for the nominal case of  $\alpha_0 = \beta_0 = 0$  is:

$$A = \begin{bmatrix} 0 & 1 \\ -1 & 0 \end{bmatrix} \quad (4-11)$$

#### 4.3.3 Filter and Smoother Equations

The computer program written for this study allows for the selection of either a forward filter estimation scheme or a Fraser Two-Filter Smoother<sup>(10)</sup>. In either case, the data interval is assumed to begin at time  $t_0 = 0$  and ends at time  $t_n$ , with measurements occurring at equally spaced times  $t_1, t_2, t_3, \dots$ , or alternatively, at equally spaced orbit angles  $\lambda_1, \lambda_2, \lambda_3, \dots, \lambda_n$ . The time between measurements is represented by  $\Delta t_k = \Delta t = \text{constant}$ . The time of interest is assumed to be  $t_j$  where  $t_1 \leq t_j \leq t_n$ .

The forward filter is a standard Kalman filter using the following equations to recursively update the covariance matrix of the state estimation uncertainties from  $t_0$  to the time of interest,  $t_j$ :

$$P_k' = \Phi_{k, k-1} P_{k-1} \Phi_{k, k-1}^T + QG^T \quad (4-12)$$

$$K_k = P_k' H_k^T [R_k + H_k P_k' H_k^T]^{-1} \quad (4-13)$$

$$P_k = [I - K_k H_k] P_k' [I - K_k H_k]^T + K_k R_k H_k^T \quad (4-14)$$

where  $P_k'$  is the covariance of the state estimation uncertainties just before  $t_k$ ;  $P_k$  is the covariance of the state estimation uncertainties just after  $t_k$ ;  $Q$  is the covariance matrix of the gyro random drift (Equation 2-18); and  $G$  is

$$G = \begin{bmatrix} G_1 \\ 0_3 \end{bmatrix} \quad (4-15)$$

where  $G_1$  is given in Equation 2-27.

The Fraser Two-Filter Smoother makes use of two Kalman filters, one to process the data forward from the beginning of the data interval to a point of interest, and the other to process the data backwards from the end of the data interval to the same point of interest. The resulting estimates of the two filters at the point of interest are then combined in an optimal manner to obtain a smoothed estimate. The forward filter is the filter previously described. The backward filter is also a Kalman filter; however, it must first be expressed in information form since the value of  $P_k'$  at end of the data interval is unknown. To do this an information matrix  $U_k'$  is defined as follows:

$$U_k' = P_k'^{-1} \quad (4-16)$$

where the initial value of this matrix at the end of the data interval is assumed to be:

$$U_{k=n}' = U_n' = 0 \quad (4-17)$$

where  $n$  corresponds to the time of the last measurement. Starting at  $t_k = t_n$ , the information matrix is updated as follows:

$$U_k' = U_k' + H_k^T R_k^{-1} H_k \quad (4-18)$$

Afterwards, the matrix is propagated backwards as follows with updates being made at each measurement time in accordance with Equation 4-18:

$$\begin{aligned} U_{k-1}' &= \Phi_{k, k-1}^T [(\mathbf{I} - J_k G^T) U_k (\mathbf{I} - J_k G^T)^T \\ &\quad + J_k Q^{-1} J_k^T] \Phi_{k, k-1} \end{aligned} \quad (4-19)$$

where

$$J_k = U_k G (G^T U_k G + Q^{-1})^{-1} \quad (4-20)$$

The final smoothed value  $P_{j/n}$  of the covariance matrix at the time of interest ( $t_j$ ) is obtained from the two filter values  $P_j'$  and  $U_j'$  as follows:

$$P_{j/n} = (\mathbf{I} - K_j U_j') P_j' (\mathbf{I} - K_j U_j')^T + K_j U_j' K_j^T \quad (4-21)$$

where

$$K_j = P_j' [(\mathbf{I} - P_j' U_j')^{-1}]^T \quad (4-22)$$

and  $U_j'$  and  $P_j'$  are given by Equations 4-19 and 4-12 respectively.

## 4.4 PERFORMANCE RESULTS

### 4.4.1 Introduction

The results presented in this section represent the performance obtained with the Fraser Two-Filter Smoother for a satellite in both a geosynchronous and a sun synchronous orbit. The latter orbit was used primarily to provide data for comparison with the results which were obtained at geosynchronous altitudes.

In all cases the satellite was assumed to be in a local vertical attitude with rotation occurring only in pitch. The nominal values of the error sources and parameters are as follows:

#### Initial State Uncertainties ( $1\sigma$ )\*

Attitude (Pitch, Roll, Yaw)	-	60 arcsec (each)
Gyro Bias Drift	-	0.03 deg/hr (each)

#### Horizon Sensing Errors ( $1\sigma$ )

Assumed to be a white noise. Values given with performance results.\*\*

#### Gyro Error Sources ( $1\sigma$ )

Random Drift	-	0.01 deg/hr (white noise)
Quantization	-	0.1 arcsec

### 4.4.2 Performance Results for Geosynchronous Satellite

In Table 4-1 the performance results are shown for a geosynchronous satellite. Data is presented showing the effect of variation in the total data processing interval (i.e., number of orbits), the

\* To simplify matters in this preliminary study, the uncertainties in satellite position and velocity are assumed to be zero.

\*\* It should be noted that the horizon errors given with the performance results are treated as equivalent angular errors in indicating the direction of the center of the earth. The values given represent the one sigma values about the pitch and roll axes.

TABLE 4-1  
FRASER SMOOTHER PERFORMANCE FOR GEOSYNCHRONOUS SATELLITE

Case	Data Interval (orbits)	Update Interval (degrees)	Horizon Error (arcsecs)	Estimation Point (orbits)	State Estimation Uncertainties (lo)						
					Attitude (arcsec)			Gyro Bias Drift (10 <sup>-3</sup> deg/hr)			
					Pitch	Roll	Yaw	X	Y	Z	
1	2	20	36	0.25	9.9	10.5	60.6	4.4	0.12	0.44	
2	2	2	36	0.25	3.3	3.7	59.6	4.3	0.05	0.14	
3	2	0.5	36	0.25	1.9	2.3	59.5	4.3	0.04	0.08	
4	4	20	36	2	4.6	7.5	59.5	4.4	0.05	0.31	
5	4	20	2	2	0.8	1.0	59.4	4.3	0.02	0.03	
6	8	20	36	0.25	6.3	6.6	60	4.3	0.02	0.22	
7	8	89	36	0.25	11.9	11.4	61	4.4	0.03	0.45	

horizon sensing error, the interval between updates with horizon measurements (in degrees of orbit), and the point at which the smoothed estimate was made (i.e., number of orbits since the start of the total data processing interval).

The first three rows of Table 4-1 show the effect of variation in update interval. Here it is seen that a decrease in the update interval (or an increase in the frequency and number of updates) improves the performance in estimating pitch, roll, pitch (Y) gyro bias drift, and yaw (Z) gyro bias drift. However, it is noted that almost no change occurs in the performance for yaw attitude and roll (X) gyro bias drift.

Cases 4 and 5 of Table 4-1 show the performance for four orbits of data processing and two different values of horizon sensing error. It is seen that reducing the horizon sensing error from 36 to 2 arcsecs results in a significant improvement in all of the state parameters except for yaw attitude and roll gyro bias drift which remain essentially at the same values as in all other cases of Table 4-1.

Cases 6 and 7 of Table 4-1 show the performance for eight orbits of data processing and two different update intervals. In comparing Case 6 with Case 1, which are similar except for the size of the data processing interval, it is seen that an increase in the data processing interval results in a definite improvement in performance except for the same two state parameters mentioned previously.

The fact that no significant difference occurs in the performance for yaw attitude and roll gyro bias drift for all cases in Table 4-1 does raise some question as to why this is so. At first glance, it would seem logical that no improvement would occur in yaw since the horizon measurements in the present situation provide information only in pitch and roll. However, it should be noted that the spacecraft is assumed to have a nominal local vertical attitude at all times, and that information on roll attitude at one point in orbit becomes information on yaw attitude at a point 90 degrees ahead or behind in the

orbit. This fact is clearly illustrated by the following two equations showing the relationships between the errors in roll ( $\phi$ ), yaw ( $\psi$ ), roll gyro bias drift ( $B_x$ ) and yaw gyro bias drift ( $B_z$ ):\*

$$\delta\phi_2 = C \delta\phi_1 - S \delta\psi_1 + \frac{S}{\omega} \delta B_x + \frac{(1-C)}{\omega} \delta B_z \quad (4-23)$$

$$\delta\psi_2 = S \delta\phi_1 + C \delta\psi_1 + \frac{(1-C)}{\omega} \delta B_x - \frac{S}{\omega} \delta B_z \quad (4-24)$$

where the subscripts 1 and 2 denote two points in orbit separated by the orbit angle  $\lambda$ ;  $S = \sin(\lambda)$ ;  $C = \cos(\lambda)$ ; and  $\omega$  is the orbital rate. If  $\lambda = 90$  degrees, Equation 4-24 becomes:

$$\delta\psi_2 = \delta\phi_1 + \frac{1}{\omega} \delta B_x - \frac{1}{\omega} \delta B_z \quad (4-25)$$

which shows that a roll error ( $\delta\phi_1$ ) at one point in orbit becomes a yaw error ( $\delta\psi_2$ ) at a point 90 degrees ahead. It is also interesting to note that Equation 4-25 can be used to indicate the relationship between the uncertainties in yaw attitude and roll gyro bias drift of Table 4-1 by neglecting the small values of  $\delta\phi_1$  and  $\delta B_z$ , so that:

$$\delta\psi_2 = \frac{1}{\omega} \delta B_x \quad (4-26)$$

Substituting  $4.3 \times 10^{-3}$  deg/hr (or  $4.3 \times 10^{-3}$  arcsec/sec) for  $\delta B_x$  (from Table 4-1) and  $\omega = 7.27 \times 10^{-5}$  radians/sec, gives 59.1 arcsecs for  $\delta\psi_2$  which is close to the values given in Table 4-1. This close relationship between the performance in estimating yaw attitude and roll gyro bias drift has been found to be the case in most of the EOS studies conducted at CSDL.

The fact that there is no change in the roll gyro bias drift performance for the various cases of Table 4-1 may also seem strange since one would normally expect the present type of local vertical measurements to provide more information on roll gyro bias drift than yaw gyro bias drift. Actually, the performance in estimating roll gyro bias drift is better at the beginning of data processing. This is clearly seen in Figure 4-1 which shows the performance of the forward

\*These equations can be obtained from the transition matrix in Equation 2-33. It should be noted in Equation 4-23 and 4-24 that the errors in gyro bias drift are assumed to be fixed between points 1 and 2.

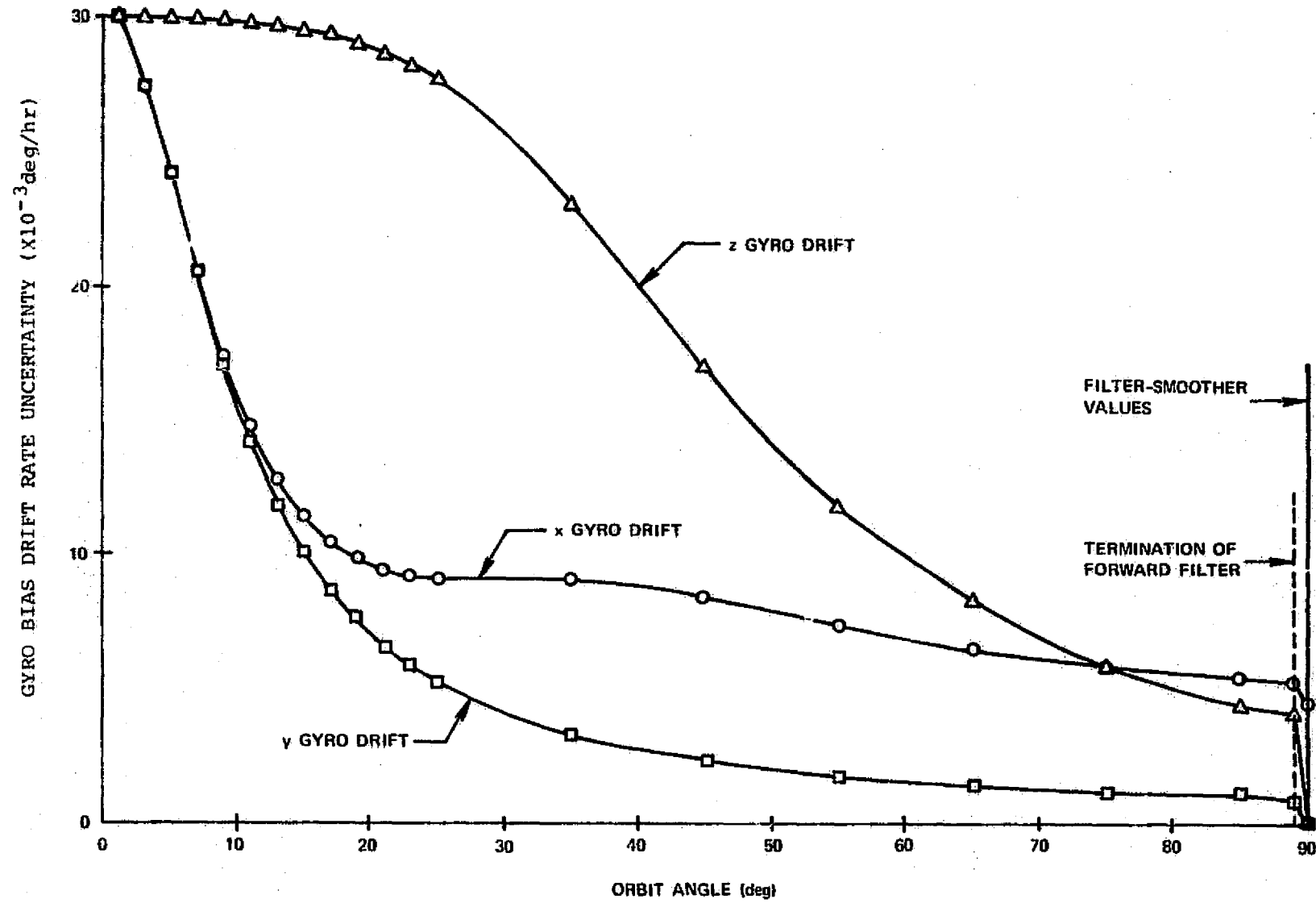


Figure 4-1 Kalman Filter Performance in Estimating  
Gyro Bias Drift for Case 2 of Table 4-1

filter for the first 90 degrees of orbit. The results in Figure 4-1 are for Case 2 of Table 4-1 where an update was made after each 2 degrees of orbital motion. Note in Figure 4-1 that the performance for yaw (Z) gyro bias drift eventually becomes better than that for roll (X) gyro bias drift. Also note that the rate of improvement in filter performance for yaw gyro bias drift is greater than that for roll gyro bias drift at the end of the data interval in Figure 4-1. Shown also are the smoothed estimates at 90 degrees which are the same values given in Table 4-1 for Case 2.

#### 4.4.3 Performance Results for Sun Synchronous Satellite

For purposes of comparison with the previous results given for a geosynchronous satellite, some performance results are shown in Table 4-2 for a satellite in a sun synchronous orbit like that used in the study of Section 2. In contrast to the previous orbit which had an altitude of 35,860 km and an orbital rate of  $7.27 \times 10^{-5}$  radians per second, the sun synchronous orbit has an altitude of 1,000 km and an orbital rate of  $10^{-3}$  radians per second. In Table 4-2 it is seen that all of the results were generated for a data processing interval of four orbits. Except for the difference in orbital period (and rate), the conditions used to generate the results for Case 1 of Table 4-2 are the same as those for Case 4 of Table 4-1. Note that the performance in estimating pitch and roll is essentially the same for these two cases, while the performance in estimating yaw is much better for the case in Table 4-2. Also note in Table 4-2 that the general performance in estimating gyro bias drift is significantly worse than that of Table 4-1. This result is primarily due to the fact that there is much less time between successive attitude updates for the cases in Table 4-2 because of the higher orbital rate.

In Table 4-2 it is seen that the performance in estimating yaw attitude and roll (X) gyro bias drift is essentially the same for all of the cases analyzed. This was also found to be true for all of the cases of Table 4-1. Also note that the relationship between the uncertainties in yaw attitude and roll gyro bias drift of Table 4-2 agrees with the relationship in Equation 4-26 when the appropriate orbital rate  $\omega = 10^{-3}$  radians/sec is used.

TABLE 4-2  
FRASER SMOOTHER PERFORMANCE FOR SUN SYNCHRONOUS SATELLITE

Case	Data Interval (orbits)	Update Interval (degrees)	Horizon Error (arcsecs)	Estimation Point (orbits)	State Estimation			Uncertainties ( $10^{-3}$ )		
					Attitude (arcsec)			Gyro Bias Drift (10 <sup>-3</sup> deg/hr)		
					Pitch	Roll	Yaw	X	Y	Z
1	4	20	36	2	4.3	7.3	27.2	26.9	0.6	4.2
2	4	20	2	2	0.5	0.6	26.8	26.8	0.1	0.3
3	4	10	2	2	0.4	0.5	26.8	26.8	0.1	0.2
4	4	5	2	2	0.4	0.4	26.8	26.8	0.1	0.2
5	4	2	2	2	0.3	0.4	26.8	26.8	0.1	0.2

#### LIST OF REFERENCES

1. White, R., R. Var, F. Grant, M.B. Adams and E. Geisler, "Interim Technical Report No. 2, Advanced Earth Observation System Instrumentation Study (AEOSIS)", Report R-821, CSDL, October 1974.
2. Ogletree, G., J. Coccoli, R. McKern, M. Smith and R. White, "Interim Technical Report No. 1, Candidate Configuration Trade Study, Stellar-Inertial Measurement System (SIMS) for an Earth Observation Satellite (EOS)", Report E-2616, MIT/CSDL, 5 November 1971.
3. Ibid. Interim Technical Report No. 2, E-2630, 31 January 1972.
4. Ibid. Interim Technical Report No. 3, E-2651, 15 June 1972.
5. White, R., "Final Report, Candidate Configuration Trade Study, Stellar-Inertial Measurement System (SIMS) for an Earth Observation Satellite (EOS)", Report R-741, MIT/CSDL, 31 January 1973.
6. White, R., and F. Grant, "Addendum to Final Report, Candidate Configuration Trade Study, Stellar-Inertial Measurement System (SIMS) for an Earth Observation Satellite (EOS)", Report R-741 (Addendum), MIT/CSDL, 31 June 1973.
7. Ogletree, G., G. Karthas and M. Smith, "Interim Technical Report No. 1, Advanced Earth Observation System Instrumentation Study (AEOSIS)", Report R-792, CSDL, February 1974.
8. Smith, M., "Problems Pertaining to the Sight Vector of a Spaceborne Imaging Radiometer", Report R-785, CSDL, January 1974.
9. Levine, G., "The Transition Matrix for a Circular Orbit", MIT/CSDL Internal Memo 11-64, February 1964.

10. Fraser, D.C., "A New Technique for the Optimal Smoothing of Data", MIT Instrumentation Laboratory Report T-474, January 1967.
11. Keach, D. and J. Knoedler, "A Study of the Feasibility of Selected Systems for Shuttle Navigation Support, Vol. II, the Tracking Data Relay Satellite System", MSC Internal Note No. 71-FM-51, Manned Spacecraft Center, 5 May 1971.
12. "Navigation Systems Characteristics, Rev 1", JSC Internal Note No. 72-FM-190, LBJ Space Center, 10 July 1973.
13. "Star Tracker and Light Shade for the Space Shuttle Orbiter", Volume 2, Proposal No. 080, Ball Brothers Research Corp., 10 May 1974.
14. Jazwinski, A., "Stochastic Processes and Filtering Theory", Academic Press, New York, 1970.
15. Wagner, W. and Velez, C., "Goddard Trajectory Determination Sub-system Mathematical Specifications", GSFC Report X-552-72-244, March 1972.
16. Kingsland, L. and Bollman, W., "An Approximate Solution to the Estimate of the Navigational Accuracy of a Deep Space Probe", JPL Technical Memo 312-884, 21 May 1969.
17. "Guidance and Navigation Requirements for Unmanned Flyby and Swingby Missions to the Outer Planets", CSDL Report R-678, May 1969.
18. Weinstein, O., "GSFC Specification for an Earth Observation Scanning Spectro-Radiometer Experiment", GSFC Report 73-15012, 30 March 1973.

19. Private communication with B. Chapman of USGS, 31 March 1975.
20. "Static Type Attitude Sensors for Synchronous Altitude Operation", Barnes Engineering Company Internal Report, 6 March 1975.
21. Savoca, R. et al, "Technical Description-Model 13-401 Earth Sensor", Barnes Engineering Company Report P-1677A, Undated.
22. Dodgen, J., and Curfman, H., "Accuracy of IR Horizon Sensors as Affected by Atmospheric Considerations", Presented at the Spacecraft Attitude Determination Symposium, El Segundo Calif., 30 September 1969.
23. Kirk, R. et al, "Infrared Horizon Definition-A State of the Art Report", NASA CR-722, Honeywell, Inc., April 1967.
24. Work, D. et al, "Calculations of the Earth's Spectral Radiance for Large Zenith Angles", U.S. Dept. of Commerce, Weather Bureau Met. Sat. Lab., Report No. 21, October 1963.
25. Thomas, J., "The analysis of  $15\mu$  Infrared Horizon Radiance Profile Variations Over a Range of Meteorological, Geographical, and Seasonal Conditions", NASA CR-725, Honeywell Inc. April 1967.
26. Girard, A., "Experimental Determination of the Earth's Infrared Horizon", Second TACITE experiment, presented at the 13th meeting of COSPAR, Prague, 19 May 1969.